Faculdade de Engenharia da Universidade do Porto

U.PORTO

FEUP **FACULDADE DE ENGENHARIA**
UNIVERSIDADE DO PORTO

Analysis on the dynamic load of an industrial robot and dimensioning of a corresponding modular structure

Alexandre Jorge Rebelo Matos

VERSÃO FINAL

Dissertação de Mestrado
Mestrado Integrado em Engenharia Mecânica
Produção, Conceção e Fabrico

Orientador: Prof. Marco Parente
Co-orientador: M.Sc. Edgar Mühlbeier

1 de Outubro 2021

Resumo

O aumento da procura por uma maior variedade de produtos requer soluções inovadoras ao nível dos sistemas de fabrico. Apesar de muitos considerarem que a quarta revolução industrial está atualmente em andamento, existem ainda falhas na produção de componentes que impedem que se atinja o potencial desejado. Existe uma necessidade de sistemas de produção capazes de oferecer altos níveis de flexibilidade e ao mesmo tempo altos níveis de automação. Este trabalho está inserido num projeto de investigação com o objetivo de colmatar essa falha através de um sistema de fabrico inovador. Este sistema combina as vantagens de máquinas especializadas para produção em grande escala com a versatilidade associada a robots industriais. Para isso as unidades de produção requerem características especiais tais como ferramentas apropriadas, sistemas de engrenagens reforçados, alto nível de comunicação e coordenação entre diferentes unidades de fabrico. Este trabalho está relacionado com o desenvolvimento de uma estrutura modular que suporta esta máquina industrial durante a operação. Inicialmente, através de programas de simulação multicorpos foi efetuado um estudo dinâmico a um robot industrial para obter o movimento que solicita o maior carregamento no seu suporte. Este estudo baseou-se numa restrição contínua dos movimentos dos diferentes eixos de rotação da máquina industrial até obter a combinação de rotações que exerce o maior carregamento que a estrutura tem de suster. Esse carregamento foi então introduzido num programa de análises por elementos finitos para dimensionar a estrutura de apoio de acordo com os objetivos do projeto.

Abstract

The increasing need for a greater variety of products, requires new solutions at the production system level. Although many consider we are now experiencing a fourth industrial revolution, there are still some aspects that prevent the manufacturing sector to achieve its full potential. There is a lack of production solutions capable of high flexibility as well as a high degree of automation. This thesis work is included in a new manufacturing approach to bridge that gap. This approach is centered around a new production system that combines advantages from specialized machines with the characteristic versatility of industrial robots. Such a versatile production system has special needs like appropriate tooling, innovative gear systems, intercommunication, and synchronization between production units. This work concerns the dimensioning of a modular structure that withstands the robot's operating loads and enables the supply of all media, energy, and information necessary. At first, multiple motion analyses of an industrial robot were performed with computer-aided programs to achieve the critical movement that generates the highest load on a base construction. This study followed a methodic approach which successively restrained the working area of the robot in order to obtain the critical movement of the overall system. After that, the load from the motion study was introduced in a finite element analysis program to experiment different dimension possibilities for the structure. This dimensioning process started with the construction of a simple virtual model which was successively improved to better represent the physical connections between different components. After that, the influence of different components' dimensions on the structural response was evaluated. In the end, a final solution that can fulfill the project requirements is proposed.

Acknowledgement

After having concluded this work, I would like to express my gratitude towards the people that were important for me since the beginning of this journey.

At first – as it couldn't be otherwise -, I would like to thank my two best friends. My parents. My mother for always making sure I took my education seriously. My father for setting the rules, and so making me the disciplined person that I am today. And again, I am thankful to both for always pushing me to give my best in everything that I do. Without them I wouldn't be the happy person that I am today.

Then, to my sister. My old rival, that with time became a great friend. A person I can always rely on to laugh about silly things and our moments passed together.

To my whole family, for always being a support to me and always providing a great environment to learn and be happy.

To all my friends, for all the good moments we have spent together and helped me endure this last semester.

To Edgar my supervisor at KIT who was always available for me and guiding me during the development of this work. His good suggestions and specially the questions he made were crucial to properly progress with the work.

To Marco my supervisor at FEUP for following this work's development and supporting me on the theory and capabilities of the computational tools used in this work.

To all of you guys, my sincere Obrigado, Dankeschön, and Thank you.

Table of Contents

Abbreviations

DOF – Degrees of Freedom

FEA – Finite Element Analysis

GUI – Graphical User Interface

MBS – Multibody Simulation

RP – Load Reference Point

TCP – Tool Center Point

WSK - Wertstromkinematik

1   Introduction

Throughout history mankind has found ways to continuously raise its standards of living. It went from hunting and scavenging groups to small farming societies, which later led to the first city, culminating in today vast urban areas. Alongside each of these transitions was the invention of new tools or establishment of new technology. Humans started by handling fire, then shaped weapons from rocks, then studied stars to forecast seasons for crop plantation, built ships to sail the seas, and so on. The current human species is the outcome from all the progress it has developed as a global community.

It is also known that this progress was never constant. There were periods with faster development, while others more stagnated. Though this is true, the rate of improvement of the overall quality of life gained a notorious growth once the first industrial revolution began in the second half of the 18th century. It brought a transition "from muscle power to mechanical power" by controlling steam pressure. It allowed societies to build stronger and more reliable means of transportation and brought the mechanization of industries. Besides this first industrial revolution, it is possible to picture other three major periods in the history of technology.

In the late 19th and early 20th centuries the second industrial revolution took place with the development of mass production. With new energy sources - electricity - and assembly lines, the processing of multiple units of the same product was made possible. This invention drove the manufacturing costs down, making those products more accessible to a wider public. Later, in the 1960s the third industrial revolution came along with the introduction of digital technology in production plants. Programmable Logic Controllers (PLCs) and other automated machines prompted a high-level of automation in manufacturing, increasing production rates even further (Schwab 2016).

Notably, each of these technological and innovative transitions were associated with periods of high economic growth and higher standards of living for all human populations. As always, there were people who benefited more than others, but there was never a time in the human history with such a low level of global poverty. It is the technology, the science, and the will to improve that drives the economic growth, which in turn brings better conditions to all our ways of living.

1.1   Industrie 4.0

In 2011 the German Federal Ministry of Education and Research - Bundesministerium für Bildung und Forschung (BMBF) - presented a project for the development of the German industry sector through its digitization. This project was called "Industrie 4.0" and is, according to the BMBF, "characterized by a strong individualization of products under conditions of a high flexible (mass)production" (Bundesministerium für Bildung und Forschung - BMBF 2021). Basically, its main objective was to equip the German manufactory sector with novel technology and improve its productivity to face the increasing competitiveness from emerging markets.

Nowadays the term "Industry 4.0" has evolved into something wider than just production technology innovation. Many argue, we are now experiencing the beginning of a fourth industrial revolution. This revolution is viewed as the first to connect different areas of

technology, due to the convergence of digital, biological, and physical innovation (Schwab 2016). The exponential increase in computing power and cheaper data storage is bringing breakthrough innovations in fields such as artificial intelligence (AI), autonomous vehicles, 3D printing, biotechnology and others. The main theme behind all these advances and their applications is connectivity through cyber-physical systems (CPS) and dynamic data processing. These allow a massive flow of information between different machines, computers, or sensors, which facilitates performing autonomous processes.

In the manufacturing industry this fourth revolution is enabling the implementation of "smart factories". According to (Deloitte Insights 2021) a "smart factory is a flexible system that can self-optimize performance across a broader network, self-adapt to and learn from new conditions in real or near-real time, and autonomously run entire production processes.". To accomplish this, these factories require a high-level of automation and cooperation between different working stations. One major characteristic is their versatility in producing different products. While traditional factories require one manufacturing line per product, a smart factory can work different products in the same line (Resman et al. 2021). With this technology a production plant can answer different orders in much shorter times, since it does not require large changeover times with the implementation of new production lines.

However, until now these smart factories rely only in the introduction of digital innovations. They merely incorporate additional sensors and actuators to conventional manufacturing machines in order to collect and process data. To fully achieve their potential – increased efficiency, increased flexibility, increased competitiveness -, these smart factories also require appropriate production systems (Mühlbeier et al. 2021). The desired high levels of versatility in production require better suited hardware with more degrees of freedom than the conventional systems. To answer this lack of innovation on the production machines' level the Wertstromkinematik (WSK) project at the WBK Institute is under development. In a close collaboration with SIEMENS® and GROB®, this investigation project aims at achieving production systems with both high flexibility and high degree of automation. Its purpose is to bridge the gap between high production levels and versatile production lines with lower efficiency (wbk Institut 2021).

1.2 Wertstromkinematik

The Werstromkinematik – "value stream kinematics" – is a flexible production system composed by an industrial articulated-arm robot capable of executing multiple production task. It combines the productivity and precision of special machines needed for turning, milling, and drilling with the flexibility of industrial robots mainly used for gripping and moving material, tools, and workpieces (LookKIT 2020/1: Industrielle Transformation 2021). This allows these kinematic units to perform the usual robot handling tasks, but also execute assembly, cutting, joining, 3D printing, as well as machining steps.

To carry out the more complex and precise processes, the WSK units are enhanced with innovative gear technologies and software support. Additionally, if the load required for a certain task is too high for the proper functioning of a production system, it can couple with another kinematic unit, and both can fulfill the task by sharing the load. This cooperation between machines allows the execution of a higher variety of tasks without loss of precision.

After performing the desired task, the systems can be again decoupled and used separately for individual processes.

This ability of a single machine to perform multiple different tasks has the great advantage of installing an entire production line composed by these kinematic systems. In addition, when it is intended to produce a different component, these machines only need to be rearranged in a new configuration in order to manufacture a completely different product. This allows a manufacturing company to invest in a number of these production units and then produce as varied components as intended without the need for additional equipment. This way, a single production plant can be flexible enough to deliver a wide variety of products in a short time period.

To promote a quick reconfiguration of the production lines, the WSK project also aims at implementing a so-called "Plug and Produce" concept. This concept has the goal to reduce changeover times as much as possible, stimulating small and medium size production volumes. Instead of switching entire manufacturing lines, some production units can remain in the same place and have their end effectors substituted to perform another process. For the machines that need to be repositioned, a load crane can move and place them in the new location where they will be attached by clamping systems and connected to the supply lines. In this way, the production line can be rapidly rearranged and immediately start with a new product. Thus, the term "Plug and Produce".

To achieve this concept a special floor factory needs to be developed in order to supply the necessary means for the functioning of the kinematic units and execution of its task. After a company has defined a fabric section for the operation of these production systems, the corresponding production area will be divided in a number of stations where these machines can be installed. To secure the desired high-level of flexibility for the kinematic units, each of these stations should be equipped with all necessary elements to perform the prescribed manufacturing processes. In other words, all stations should be supplied with all sources necessary for the execution of all production tasks. Even if for a certain product there is no need for cutting or machining steps, the cutting fluid supply should be available in case it is needed for a future product.

This widespread necessity of having all stations fully supplied, requires a grid distribution of all media, power, and data cables (Mühlbeier et al. 2021). To answer this, the wbk researchers thought of using elevated platforms - like a false fabric floor – allowing all the supply elements to run underneath and provide them to the kinematic units from the bottom. As a consequence, all floor stations will have an interface through which the cables underneath can connect the robotic systems. In addition, these modular stations will also possess zero point clamping systems that allow the rapid reconfiguration of the production lines and assure the units positioning. Seen from above, the entire production area will be divided in segments with the same area - each with an interface for the kinematic unit supply and clamping points to secure it during operation - Figure 1.1.
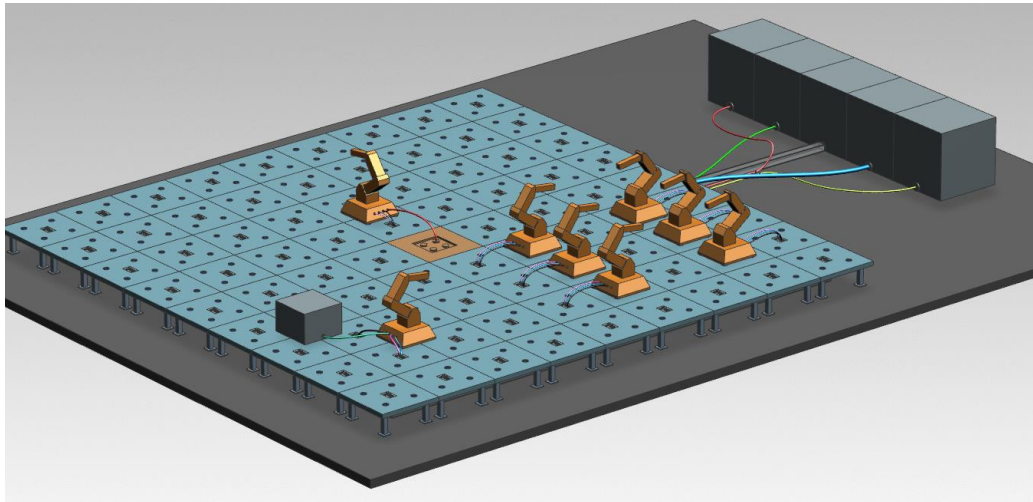
Figure 1.1 - Scheme of the production area with WSK units (Alznauer 2021)

1.3   Structure of the thesis

This Master thesis was focused on the working stations where the WSK units can be attached. The objective was to dimension these modular structures to withstand the load exerted from the robotic systems. To accomplish that, this work was divided in two separate phases.

- Motion analysis of an industrial robot.
- Dimensioning of the modular structure.

Like any structural design process, it is first necessary to define or estimate the external loads that will be applied (Udeyo 2021). At the time of this work, there was no prediction or calculation regarding the loads these production systems would exert on their base structures, because these units were not yet conceived. For this reason, the first phase of this work was oriented towards obtaining the maximum loads an existent industrial robot generates under operation. To achieve the movement that exercises the most stresses on the base structure, a methodical approach based on motion analyses was performed. These analyses compared different movements of the robotic system and were executed resorting to a multibody simulation program.

Having obtained the maximum external loads, it was then possible to start the dimensioning process. The goal here was to obtain a structure with defined dimensions that could withstand the prescribed loads. To evaluate the structural response of the base construction a finite element analysis (FEA) program was utilized. This program allowed the comparison of varied models with different dimensions in order to achieve a final solution which respected the project design requirements and sustained the robot operation. In the end, a modular structure with defined dimensions was proposed, as well as other relevant remarks and conclusions taken from the structural analyses.

2 Literature

In the following sections of this text are presented the theories and techniques behind motion and structural analyses. Understanding the methods and principles on which different computer programs rely to solve these engineering problems is fundamental for a proper product development. For this reason, in the next sections are broached the two types of analyses which played a crucial role in the elaboration of this work.

2.1 Motion Analysis

2.1.1 Introduction

A large number of mechanical systems possess moving parts. Those movements are usually defined to perform a certain functionality. It is essential for the product development process to correctly understand how a system does execute the desired movement. Depending on the mechanism and on its function, it might be important to know the highest velocities achieved, or the driving torques required, or the impact forces involved. These are examples of motion characteristics which can be obtained through a motion analysis. Instead of manufacturing a prototype and testing its kinematic or dynamic behavior, a development team can use motion analysis to simulate and evaluate the movement of parts in a mechanism. The simulation of those systems servs as a primary step in the development of a wide range of products such as: mechanisms, robots, space structures, vehicles, the human body, and others (Ling et al. 1994). Figure 2.1 shows an example of system in which motion analyses are frequently performed.
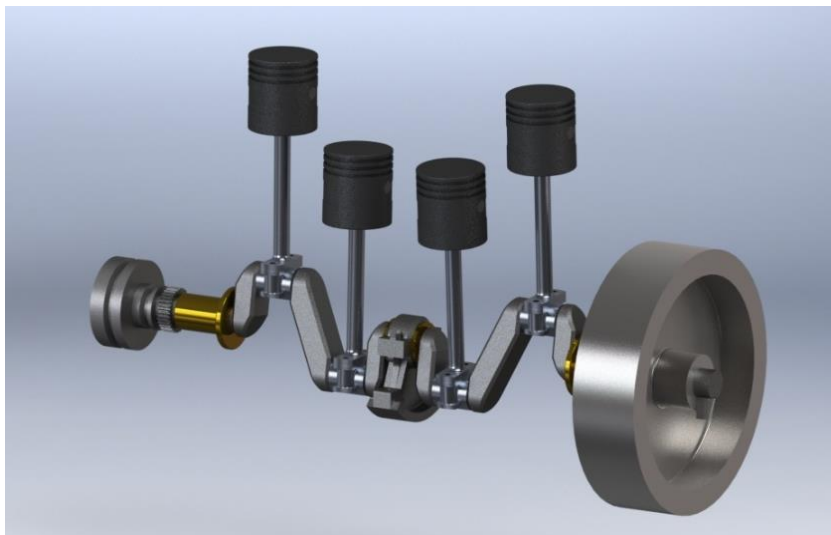

Figure 2.1 - Internal components of the combustion motor of an early 20th century ship

Usually, motion analyses are divided into two major problems: kinematics and dynamics. Kinematics is the study of motion without considering forces or reactions that cause it. Dynamics is the study of motion that results from forces exerted on components with inertia. The formulation of the equations that characterize the motion of a system are based on different physical laws and principles. Unfortunately, the obtained equations of motion are second-order differential equations. That is why, only a small number of these problems can

be solved by hand using analytical equations. The vast majority must be solved by computer-aided programs through numerical methods.

To answer this need, a large number of commercial motion software tools were developed from the late 70s until the end of the century. The currently available programs can be divided in two specification groups: the general- and the single-purpose programs. The former codes support general applications, such as 2D and 3D kinematic and dynamic simulations. Some have strong ties to CAD through designated interfaces where it is possible to model elements on the motion analysis program. Some examples of these are ADAMS®, DADS, Solid Edge® Motion or CATIA® Motion. On the other hand, the specialized codes usually offer more capabilities in specific engineering fields in addition to standard general capabilities. One known example is the ADAMS/Car which allows users to simply enter vehicle model data into the templates and the program automatically constructs subsystem models (e.g., engine, shock absorbers, tires) as well as full vehicle assemblies.

2.1.1.1 Multibody Systems

Most products involve multiple moving parts. Such products are usually referred to as multibody systems. A multibody is a system composed of several interconnected elements (or bodies). A body is "a mechanical component capable of achieving large translational and rotational displacements" (Shabana 2013). A rigid body is considered to be nondeformable and, as such, these theoretical bodies are widely used in analyses of physical systems or mechanism where there are large displacements and nonsignificant material deformation. However, in some other situations where deformations are substantial during motion, certain components have to be considered flexible. Even if there are no large deformations while in operation, a mechanism might have some parts considered flexible to increase the quality of the model and analyze other issues, for example undesired vibrations.

The connections that relate the movement between different parts are usually referred as joints. These joints are an important aspect of a multibody system. They can couple two different bodies, restricting all movement from one part to the other, or they can act as imperfect connection, allowing relative displacement between bodies. Basically, a joint connected two bodies and can introduce one or more degrees of freedom in the system, depending on the type of joint used. At the same time, it is also considered that the use of joints imposes constraints or restrictions on the bodies' movement, since it prevents displacement on other directions. In the end, a joint adds a certain relative movement, hence it provides at least one degree of freedom, while it restricts the other possible motions, thus imposing kinematic constraints (Ling et al. 1994). In practice these connections are made of bearings, rod guides, sliders, which can be classified as revolute, prismatic, or other types of joints.

In a simple manner, a multibody system is an assembly of two main kinematic groups of components: bodies and joints. Besides these, a multibody can have internal force elements, such as, springs, dampers, or cables that exert forces between two bodies of the system. These are often referred as action-reaction forces since they develop equal and opposite forces on the two links they connect. Then there are also action-only – external - force elements, which exert forces on the system without internal reaction. Examples of these forces are the gravity

acting on all bodies or electric motors, which actuate on the joints to control the desired motion of the links, typically used in robotic systems (Lynch and Park 2017).

2.1.2   Analytic Analysis

Analytical analyses are based on analytical formulations to solve motion problems. Due to the complexity of the formulated equations, they are only applicable to simple problems, such as single particle motion and single-body dynamics. For these cases, closed-form solutions are available. Usually, assumptions have to be made in advance for formulating or deriving equations of motion. For example, a moving object must be assumed to be of concentrated mass to consider it as a particle dynamic problem. On the following sections of this paper are presented the physical theories from which the equations of motion can be derived to solve particle and single-body problems.

2.1.2.1   Particle Motion

Particle motion is the simplest problem to solve. In general, moving objects are reduced to particles with concentrated mass. These particles can only move in three directions. Particle rotations are not considered. The position of this particle can be defined in relation to a global reference frame by three independent variables. As it has no dimensions, it can be considered a single point in Euclidean space and, therefore, it can be fully described by a position coordinate vector with three scalar values:

$$\boldsymbol{r_i} = \begin{Bmatrix} x_i \\ y_i \\ z_i \end{Bmatrix}$$

The two main theories used to formulate the equations of motion for particle motion are the second Newton law and the energy method. The Newton physical law is straightforward, but unfortunately, is limited to very simple problems. In those situations, a free-body diagram for the particle is at first built, applying then the second Newton's law $F = ma$ to formulate the differential equations that govern the particle movement. For the energy method case, kinetic energy and potential energy are first defined for the moving particle. After that, the energy conservation law or the Lagrange formalism can be employed to derive the equations of motion. This method is often more utilized for complex systems.

The conservation law of mechanical energy states that the total mechanical energy - the sum of kinetic energy T and potential energy U – in a system is constant in time $\frac{d}{dt}(T + U) = 0$. This relation can be applied to many particle problems, however the energy method based on the Lagrange formalism can be utilized to derive the motion equations from more general situations. It relies on the Hamilton's principle for particle dynamics, where the Lagrangian value $L = T - U$ is combined with mathematical treatment through virtual work techniques to obtain the following expression applied to a system with n degrees of freedom characterized by a vector $\boldsymbol{q} = [q_1, q_2, \dots q_3]^T$

$$\frac{d}{dt}\left(\frac{\partial L}{\partial \dot{\boldsymbol{q}}}\right) - \frac{\partial L}{\partial \boldsymbol{q}} = Q \qquad\qquad \text{Equation 2.1}$$

When the system is conservative, $Q = 0$. Otherwise, - for example, when friction forces are considered - $Q = F$, F being the force vector correspondent to the coordinate vector q.

These three physical formalisms here exposed can also be applied to systems composed by multiple particles. For such a system, the equations of motion for a particle i can be derived from the Newton's second law as

$$m_i \ddot{r}_\iota = F_i + \sum_{j=1}^{n} f_{ij}$$

<div align="right">Equation 2.2</div>

where m_i is the mass of the particle i, r_i is the position vector, F_i the external forces acting on the particle and f_{ij} the interaction forces from the other particles of the system. For the energy methods, the system kinetic and potential energy values equal the sum of the respective energy of all system particles.

2.1.2.2 Rigid body generalized coordinates

Before entering the analysis of a rigid body motion, it is necessary to define unequivocally the configuration of a body in relation to a reference coordinate system or frame. The chosen reference frame will be an inertial, global coordinate system. As was seen before, the position of a particle i in space can be totally described by three translational parameters creating vector r_i. Unlike particles, a free rigid body moving in space occupies space and has geometrical characteristics – center of mass, moments of inertia, and so on. In other words, a rigid body has six degrees of freedom – three translation and three for rotation.

A free rigid body moving in space can be described by the position of one arbitrarily chosen point and orientation parameters that define the rotation of the body around that point. Usually, the chosen point corresponds to the center of mass. There are infinite different possibilities to choose from to represent the rotation of a body. Depending on the multibody system some might be more convenient than others (Flores 2015). In the following subsections are presented some of the best-known formalisms to obtain the rotation matrix of a body.

The most straight-forward formalism is the matrix of direction cosines. This method creates a coordinate system attached to the body – usually, at the center of gravity. Each column i of the transformation matrix A contains the components of the vector u_i that constitute the corresponding body frame vector u_i' projected onto the inertial frame. As it can be seen, the generation of matrix A results from describing each of the three body frame vectors in the global frame.

$$A_i = \begin{bmatrix} a_{11} & a_{12} & a_{13} \\ a_{21} & a_{22} & a_{23} \\ a_{31} & a_{32} & a_{33} \end{bmatrix}$$

$$u_x' = \begin{Bmatrix} a_{11} \\ a_{21} \\ a_{31} \end{Bmatrix} \qquad u_y' = \begin{Bmatrix} a_{12} \\ a_{22} \\ a_{32} \end{Bmatrix} \qquad u_z' = \begin{Bmatrix} a_{13} \\ a_{23} \\ a_{33} \end{Bmatrix}$$

However, this method is neither practical nor convenient and, for this reason, is rarely used to describe three dimensional rotations in multibody system dynamics (Shabana 2013). Since there are nine direction cosines in the transformation matrix A and only exists three independent direction cosines – associated with the three rotational degrees of freedom – this formulation requires six equations to determine the matrix. Three equations to assure unit module for each column and other three to impose orthogonality between the three columns. The nine elements of the matrix are not independent and there is no subset of elements that can define unequivocally the orientation of the frame (Ling et al. 1994). This means all nine values of matrix A need to be defined, when only three should be enough to describe the three degrees of freedom of rotation. This is the major drawback of this formulation and, thus, an alternative method that does not require so many interdependent parameters is more appropriate.

There are many three-parameter formalisms that define the relative orientation between two reference frames. Those best known are the Roll-Pitch-Yaw rotations – Bryant Angles – and the Euler angels. Both methods rely on succession of three rotations which move the body frame to the desired final position. Basically, any rotation matrix can be decomposed as a product of three rotation matrixes around the principal axes (Blundell and Harty 2015). Thus, any orientation of a body coordinate system can be obtained by a minimum of three successive rotations, as evidenced on Figure 2.2. This is considered a minimal representation because there is no need to apply equations between the rotation parameters. The three angles around which the rotations are performed are defined as Euler angles.
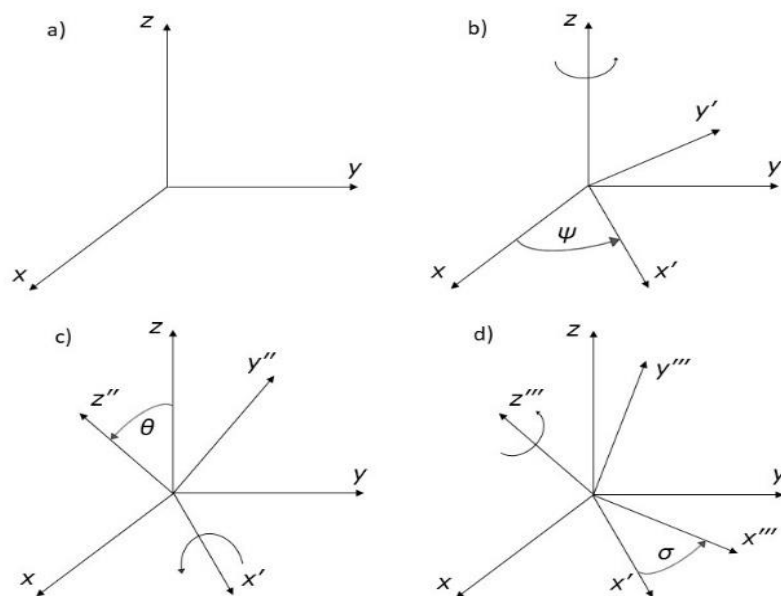

Figure 2.2 - Illustration of the Euler angles successive rotations

From all the twelve possible conventions - without redundancy - the Z-X-Z is the one most used (Flores 2015). This means a body rotates first by ψ about body frame Z-axis, then rotates θ about body X-axis and finally by σ around new body Z-axis. The (ψ,θ,σ) are the Euler angles that represent the final orientation of the body. All other conventions generate rotations in different sequences, being XYZ sequence often known as Bryant Angles. In this case we will

consider the Z-X-Z sequence. To obtain the transformation matrix of the final orientation, it is necessary to successively multiply the three transformation matrixes generated by the rotation of each angle. The calculations necessary to obtain the transformation matrix associated with the previous figure are as follows.

$$D = \begin{bmatrix} c\psi & -s\psi & 0 \\ s\psi & c\psi & 0 \\ 0 & 0 & 1 \end{bmatrix} \qquad C = \begin{bmatrix} 1 & 0 & 0 \\ 0 & c\theta & -s\theta \\ 0 & s\theta & c\theta \end{bmatrix} \qquad B = \begin{bmatrix} c\sigma & -s\sigma & 0 \\ s\sigma & c\sigma & 0 \\ 0 & 0 & 1 \end{bmatrix}$$

$$A = D \times C \times B = \begin{bmatrix} c\psi c\sigma - s\psi c\theta s\sigma & -c\psi s\sigma - s\psi c\theta c\sigma & s\psi s\theta \\ s\psi c\sigma + c\psi c\theta s\sigma & -s\psi s\sigma + c\psi c\theta c\sigma & -c\psi s\theta \\ s\theta s\sigma & s\theta c\sigma & c\theta \end{bmatrix}$$

Despite their popularity, Euler angles present singular positions where its parameters are not defined unequivocally. This happens when *sinθ* is zero, making the axes of the first and third rotations coincide. If that happens then ψ and σ cannot be distinguished and it is impossible to know whether θ equals to zero or an integer multiple of π. It can be observed that the singularity phenomenon is present in any three rotational coordinates regardless of their sequence. This problem can be avoided if another variable is introduced, becoming a four non-independent parameter formulation.

According to Euler's rotation theorem, a rotation of a rigid body in space can always be described by a rotation angle φ around some axis - Figure 2.3. "The theorem indicates that the orientation of the body-fixed axes at any instant can be obtained by an imaginary rotation of these axes from an orientation coincident with the global axes" as (Flores 2015) mentioned. The parameters needed for this formulation are the three direction cosines of the unit vector u which defines the axis of rotation and the last parameter angle φ. The four-parameter formulations do not have the singularity problems of the three-parameters. However, the number of variables is increased, which imposes more constraint equations to the multibody system.
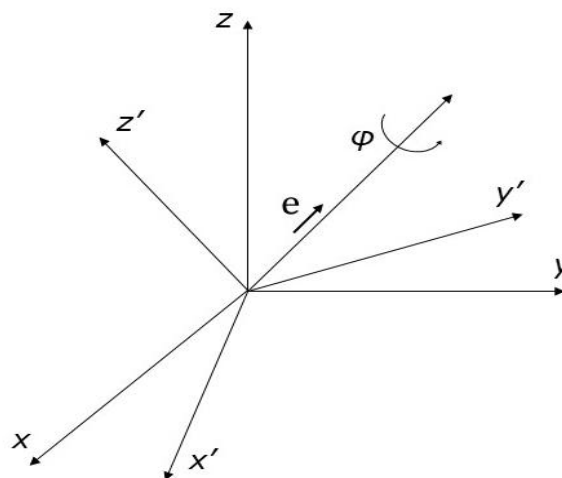

Figure 2.3 - Representation of Euler's rotation theorem

The best-known four-parameter formalism is based on the Euler parameters, which can be

$$p = \begin{Bmatrix} e_0 \\ e \end{Bmatrix} = \begin{Bmatrix} e_0 \\ e_1 \\ e_2 \\ e_3 \end{Bmatrix}$$

described by the following vector.

Value e_0 is equal to $cos(\frac{\varphi}{2})$ while the other three values compose vector e which defines the orientation of the axis of rotation. Vector e has a magnitude of $sin(\frac{\varphi}{2})$. The transformation matrix can be expressed in terms of the Euler parameters as shown.

$$A = 2 \begin{bmatrix} e_0^2 + e_1^2 - \dfrac{1}{2} & e_1 e_2 - e_0 e_3 & e_1 e_3 + e_0 e_2 \\ e_1 e_2 + e_0 e_3 & e_0^2 + e_2^2 - \dfrac{1}{2} & e_2 e_3 - e_0 e_1 \\ e_1 e_3 - e_0 e_2 & e_2 e_3 + e_0 e_1 & e_0^2 + e_3^2 - \dfrac{1}{2} \end{bmatrix}$$

Now that different methods to represent a rigid body orientation were exposed, it is possible to introduce the notion of generalized coordinates. The set of chosen parameters that characterize unequivocally, at any instant of time, the configuration of a body, that is, the position and orientation of all points that compose that element are called a set of generalized coordinates (Flores 2015). Such a set of variables are usually represented by vector $q_i = \{q_{i1}, q_{i2}, \dots, q_{in}\}^T$ composed by n variables that fully define body i configuration in relation to a global coordinate frame. Keep in mind that vector q_i is composed of vector r_i – with three translational components of the body origin – and vector p_i with the rotational parameters. If the angular parameters selected were the Euler or the Bryant angles, then the dimension of q_i would be six, if the Euler parameters were used, then q_i would be instead a seven-dimension vector as shown.

$$q_i = \begin{Bmatrix} r_i \\ p_i \end{Bmatrix} = \{x_i \quad y_i \quad z_i \quad e_0 \quad e_1 \quad e_2 \quad e_3\}^T$$

2.1.2.3 Rigid Body Motion

In physics, rigid-body dynamics is the study of a body's motion when submitted under external forces. The relation of those forces with the movement of a body is given by the so-called equations of motion. They are divided in two types: the translational and the rotational equations of motion. The first equation corresponded to the translation equation and is given by the Newton's second law.

$$F = m\ddot{r}_i$$ Equation 2.3

This means that the vector F with the sum of all external forces acting on body i along the three translational directions is equal to the mass of the body multiplied by the acceleration of the center of gravity $\ddot{r}_i$. The second equation refers to the rotation of a body and is given by,

$$M = \dot{H}$$ Equation 2.4

with M being the moment of force or torque and H the angular moment at the body's center of mass. If the body reference frame is aligned with the principal axes of inertia of the body, by decomposing and deriving H the following equation is obtained,

$$M = I\dot{\omega} + \widetilde{\omega}I\omega$$ Equation 2.5

where I is the inertia matrix of the body and ω the angular velocity vector. This equation is known as Euler's equation of motion.

Besides the above shown equations of motion, the energy methods can also be applied to rigid body problems. To do so, it is only necessary to adjust the kinetic energy equation to also include the rotational motion as follows,

$$T = \frac{1}{2}m\dot{r}^2 + \frac{1}{2}\omega H$$ Equation 2.6

where $\dot{r}$ and H are the velocity and angular moment at the center of gravity of the body, respectively. The potential energy equation remains the same. With this, it is possible to apply the conservation of energy method or use the Lagrange equation at Equation 2.1 to obtain the equations of motion for a rigid body case.

2.1.2.4 Multibody Kinematic Analysis

Multibody kinematic analyses are responsible for relating the physical positions, velocity, and acceleration of all system parts with respect to time, not accounting the exerted forces to generate such motion. These analyses involve formulating the kinematic equations of the multibody and solving them for position, velocity, and acceleration of each body. This is an important step in the design process of general mechanism, particularly for studying allowable workspaces and robotics. Mechanical system where position, velocity, and acceleration of the moving components must be known, require kinematic analyses to assess the proposed functionalities and measure performance.

Before presenting the physical principles used to generate the kinematic equations, it is first necessary to address an important characteristic of a multibody system. The degrees of freedom. A rigid body in space without any motion restriction has six degrees of freedom. Let

us consider two free bodies in space. The system composed by these two has in total 12 degrees of freedom - 6 from each. If a joint is added to connect both bodies, then some restrictions will be established, preventing the random motion.

According to the type of the joint added, different restrictions will be established. This means, one of the bodies' position is partially dependent on the other. They are not entirely free anymore. In other terms, introducing a kinematic joint to a system, will reduce the total number of degrees of freedom by the number of imposed constraints due to that joint. In a multibody system with many bodies and joints connecting them, the number of degrees of freedom of the system depends on the number and types of joints applied. The number of degrees of freedom of a mechanism can be calculated using Grübler's formula:

$$DoF = m\,(\,N-1\,) - \sum_{i=1}^{J} c_i \qquad \text{Equation 2.7}$$

Where $m = 6$ for spatial systems and $m = 3$ for planar, N equals the number bodies, c_i is the number of constraints given by joint i, and J the number joints. In other terms, a system starts with $N-1$ bodies with 6 degrees of freedom. The -1 represents the body that acts as the base, which means it is fixed to the environment. The total number of rigid body degrees of freedom would be $m(N-1)$ if the system had no restrictions. The correct number can be then obtained by subtracting the number of constraints introduced by each joint - Table 2.1. This formula only holds true if all the joint constraints are independent, otherwise the DoF of the system will be higher.

Table 2.1 - Different joint types and their degrees of freedom

JOINT TYPE	DEGREES OF FREEDOM	N. PLANAR CONSTRAINTS	N. SPATIAL CONSTRAINTS
REVOLUTE	1	2	5
PRISMATIC	1	2	5
HELICAL	1	-	5
CYLINDRICAL	2	-	4
UNIVERSAL	2	-	4
SPHERICAL	3	-	3

Redundant joint constraints can appear when several joints restrict the same degree of freedom. The redundant constraints are usually not present in kinematic problems. However, they are often introduced due to structural reasons (a door supported by three hinges, used to strengthen the construction, is a simple example of system with redundant constraints, since in practice the door kinematics would be the same with a single hinge). If redundant constraints are present in the multibody system, the constraint equations are dependent. (Wojtyra 2009)

Multibody systems with negative number of degrees of freedom are denoted over-constrained system. A typical example is the truss structure where extra links are added to distribute the load, reducing stress on other links. Systems with zero degrees of freedom are denoted fully constrained mechanisms and represent a structure that is fixed, non-movable. When a mechanism has a positive number of degrees of freedom, then it is possible to solve it for kinematic and dynamic problems.
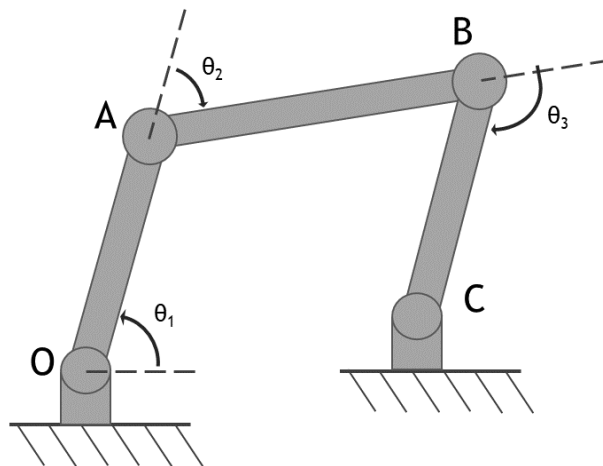

Figure 2.4 - Scheme of a 4-bar mechanism

There are different methods utilized to formulate the kinematic equations of a mechanism. Usually, these methods rely on the geometry features of the system. One typical approach is the loop closure method, which creates vectors between each joint of the system to generate the kinematic equations (Ling et al. 1994). Those equations will relate the joints positions with one another based on the geometry of the body. After that, it is possible to derive those equations in respect to time to obtain the velocity equations, and then derive again to get the acceleration equations. Once enough independent equations are obtained, it is possible to solve the problem by simply substituting the variables that represent the degrees of freedom by their desired value. Let us take for example Figure 2.4.

Applying the Grübler's formula to the presented system, the number of degrees of freedom obtained is equal to 1. $DoF = 3(4-1) - 4 \times 2 = 1$. There are 4 bodies – the ground $\overrightarrow{OC}$ also acts as a body – and 4 revolute joints. Any of the described angles can be selected as the degree of freedom. Basically, that will be the controlled angle and its variation will make the rest of the system move. The kinematic equations that characterize this system can be obtained by closing the kinematic loops of the system. In other terms, the sum of vectors representing the length and orientation of each link is equal to the vector from the first joint to the last accounted. From the loop closure method the following equation is formulated.

$$\overrightarrow{OA} + \overrightarrow{AB} + \overrightarrow{BC} = \overrightarrow{OC} \qquad\qquad \text{Equation 2.8}$$

Assuming for example $\overrightarrow{OC} = \{3,1\}^T$, it is possible through Equation 2.8 to obtain the following kinematic equations relating the three variables θ_1, θ_2 and θ_3.

$$l_1 \cos(\theta_1) + l_2 \cos(\theta_1 - \theta_2) + l_3 \cos(\theta_1 - \theta_2 - \theta_3) = 3$$

$$l_1 \sin(\theta_1) + l_2 \sin(\theta_1 - \theta_2) + l_3 \sin(\theta_1 - \theta_2 - \theta_3) = 1$$

If the motion of the chosen angle is defined, then through the previous equations it is possible to obtain the corresponding position for the other variables. As it can be observed, the obtained equations are not linear making their solution more cumbersome. If the above system was open chained, then vector $\overrightarrow{OC}$ would not be constant. Instead, both parameters of this vector – let us say $\{x_c, y_c\}^T$ - would be variable in time. Therefore, there would be in total 5 variables in the system for 2 equations, which proves the existence of 3 degrees of freedom – corresponding to the 3 angles free to rotate. By further deriving the above equations it is then possible to obtain the velocity and acceleration equations for the system.

2.1.2.5 Multibody Dynamic Analysis

Problems involving forces and the consequent motion they cause must be solved by dynamic analysis. One example when such an analysis is needed, is when there is the intention to know the minimum torque necessary to elevate a mechanical arm carrying weight. To calculate that torque value, one needs to apply the equations of motion for the multibody system.

The equations of motion are used to describe the dynamic behavior of a multibody system. The movement of the interconnected bodies can be formulated by equations that result from the same principles exposed earlier for the rigid-body case: Newton's second law or energy methods. These equations are written for the general motion of the individual bodies - as if they were independent – adding then the constraint conditions from the joints (Shabana 2013). These constraint conditions raise from the movement restrictions each joint imposes on the adjacent bodies. These joint restrictions allow the transmission of forces or torques between the bodies. These forces are also called reaction joint forces and are related to the kinematic equations above exposed. Basically, the motion of each body is described by the kinematic equations, while its dynamic behavior results from the equilibrium of the externally applied and transmitted torques and forces (Flores 2015).

Unfortunately, the analytic solution of dynamic problems for multibody systems is too complex. It is true, the obtained equations will depend profoundly on the theory utilized to formulate them, however the obtained relations are mostly nonlinear algebraic or nonlinear differential equations that are impossible to solve without numerical methods (Ling et al. 1994). Furthermore, the formulation process of the equations of motion is already complicated because it requires the rearrangement of the kinematic equations to explicit the variables that will be utilized. "There is no specific (analytic) method that is powerful and general enough to

be consistently applied to formulate and solve general multibody dynamics problems." as described by (Chang 2015).

2.1.3 Computer-Aided Methods

The computer-aided methods for solving problems with multibody system have one main objective. Create a systematic approach to formulate and solve the equations of motion. This method should be flexible enough to adapt to different mechanisms, in order to obtain the equations of motion for each body and its constraint equations from the adjacent bodies. That formulation should be uniform and consistent to be implemented on a digital computer. Then, the computer can resort to numerical integration to solve the equations of motion. With this, the extensive work of formulating analytical equations by hand can be handled by a computer.

In a general overview, motion analysis computer-aided methods rely on:

1. Formulating the kinematic constraints equations that characterize the relative movement between adjacent bodies in a mechanical system.
2. Differentiating the constraint equations in respect to time to obtain the velocity and acceleration equations.
3. Applying one of the physical theories to formulate the equations of motion for each body.
4. Solve the equations of motion using numerical methods.

2.1.3.1 Kinematic Analysis

The kinematic analysis is the study of the motion of a multibody system, regardless of the causes that generate it. Since there are no forces involved, the motion of the system is provoked by imposing movement on certain elements – input elements - that drive specific degrees of freedom of the system. It is then clear, that the number of these input or guiding elements must be equal to the number of degrees of freedom of the multibody mechanism (Ling et al. 1994). Once the motion of the guiding elements is defined, it is then possible to calculate the position, velocity and acceleration of the remaining – dependent - elements through kinematic constraint equations (Nikravesh 1988). As was previously explained, the constraint equations result from the kinematic relations between different coordinate parameters describing the system topology. In short, the kinematic analysis is performed by solving a set of equations obtained from the kinematic and guiding constraints.

Before taking a look into the formulation and solution of the kinematic problems it is first necessary to address the coordinate system selection as it plays an important role on the equations obtained.

As was already shown, it is fundamental to properly define the configuration of a rigid body. The same happens for a multibody mechanism. It is necessary to choose a set of parameters that can fully characterize all bodies of the system. As was shown, the configuration – position and orientation - of a body can be described by a set of parameters which compose vector q_i. This vector holds all the information necessary to unequivocally define body i. It is then possible to expand this representation and establish vector $q = [q_1, q_2, q_3, \dots, q_n]^T$ – with dimension n bodies of generalized coordinates q_i - which carries the values of all n elements of the multibody system. Basically, this vector q possesses the information of all bodies' position and orientation.

The selection of these parameters will have a deep influence on the formulation techniques used to obtain the kinematic equations that characterize the geometry of the system. Some coordinates are more favorable than others to apply the Newton's Laws, for example. Here will

be presented two types of coordinate systems: the relative and the reference point coordinates.

Relative coordinates define the position of each body in relation to the previous element in the mechanism. This is accomplished by using the parameters or coordinates that correspond to the relative degree of freedom allowed by the joint which connects both elements. The earlier explored case for formulating the analytic kinematic equations was based on this coordinate system – Figure 2.4. Relative coordinates are the type of dependent coordinates that lead to the minimum number of variables to define a system. In fact, in the case of open chain systems the number of relative coordinates is equal to the number of degrees of freedom.

Due to the low number of coordinates, it has a good numerical efficiency. Because each degree of freedom is associated with a coordinate, it is simple to control the motion permitted by that join. This is particularly interesting for systems with actuators, such as, motors responsible by governing a degree of freedom (Lynch and Park 2017). For this reason, relative coordinates are especially effective and suitable for open chained robots, with revolute and/or prismatic joints and actuators controlling each joint. However, as was observed, the formulated equations are complex nonlinear equations. Another downside of this coordinate system is the need for postprocessing to determine the motion of each material point of the system. If for example the motion of an element's center of mass is required, then it is necessary to generate and solve more equations to obtain that information. (Ling et al. 1994)

Reference point coordinates define the absolute position of each body of the system through the characterization of an elements' point – usually its center of gravity – and angular variables that define the body's orientation. This method utilizes sets of generalized coordinates as shown before for the rigid-body case, where an element's point position is defined by cartesian coordinates and then other parameters define the orientation of the body referring to an inertial frame - Figure 2.5.
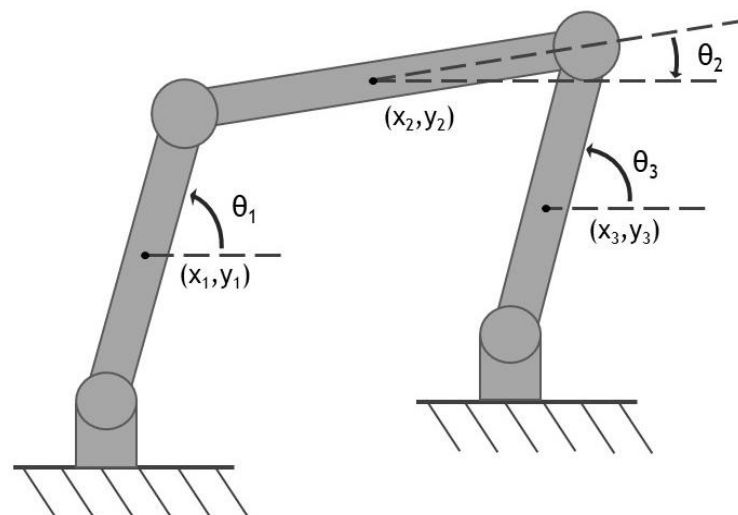

Figure 2.5 - Scheme of a 4-bar mechanism defined by reference point coordinates

As was shown, the configuration – position and orientation - of a body can be described by a set of parameters which compose vector q_i. This vector holds all the information necessary

to unequivocally define body i. It is then possible to expand this representation and establish vector $\boldsymbol{q} = [q_1, q_2, q_3, \ldots, q_n]^T$ – with dimension n bodies of generalized coordinates q_i - which carries the values of all n elements of the multibody system. Basically, this vector $\boldsymbol{q}$ possesses the information of all bodies' configuration.

Because every element of the system has a minimum of three or six coordinate points (planar or space), this method requires much more variables than the relative coordinates. This means, for certain mechanisms this method has a low numerical efficiency when compared with relative coordinates. On the other hand, it requires no post processing as the position of each element is directly determined.

The formulation of the constraint equations with reference point coordinates relies on the restrictions that joints introduce between adjacent elements. The equations are obtained relating the coordinate points of a body with the coordinate points of the next or previous element in the kinematic chain. Basically, to each body it only concerns the motion of its neighbors, because of the joint connecting the two. A joint that allows one degree of freedom, will impose two constraint equations in a planar system between the two coordinate points it connects. This means the constraint equations with reference points are established at a local level - joint by joint. This is particularly interesting for complex systems, since the equations imposed by equal joint types have the same format, they just need to adjust according to the bodies dimensions (Lynch and Park 2017). Once the type of equation originated from a certain joint is established, it is possible to keep adding more elements to the system that it does not increase the equations complexity, just their number. Taking the Figure 2.5 above, the constraint equations between point 1 and 2 are as follows,

$$X_2 - X_1 = \frac{L_1}{2}\cos(\phi_1) + \frac{L_2}{2}\cos(\phi_2)$$

<div align="right">Equation 2.9</div>

$$Y_2 - Y_1 = \frac{L_1}{2}\sin(\phi_1) + \frac{L_2}{2}\sin(\phi_2)$$

If the same is done for the remaining points, there will be in total eight equations for nine coordinate variables, being one of them the designated degree of freedom.

The principle behind the formulation of these equations in the spatial case is the same. Define which are the appropriate equations for each type of joint and then construct the constraint equations for adjacent bodies connected by the joint used. However, this processing for 3D problems is more laborious since it involves orientation parameters that require caution in their use and there are more types of joints available – some allowing more than one degree of freedom (Haug 1984).

To sum up the comparison between these two coordinate systems, relative coordinates require a lower number of equations, while reference points utilize more variables generating more equations to solve. Relative coordinates allow the distinction between open and closed chained systems and are especially suitable for robotic applications, because its parameters already define the motion generated at each joint. However, the constraint equations obtained are more complex in relation to reference points. This can be easily understood since relative

coordinates' equations can relate all coordinate parameters, while in reference coordinates each equation relates exclusively adjacent coordinates.

Besides, reference point coordinates do not require post processing and its implementation is much easier on a computer program (Ling et al. 1994). Other advantage of this coordinate system is its flexibility to be used in every multibody system, even if its efficiency is lower for certain cases in comparison with relative joints (Nikravesh 1988). Nevertheless, the matrixes of equations obtained with reference points are sparse and with special techniques it is possible to make the numerical integration more efficient (Ling et al. 1994). These reasons make the reference point coordinates the most used in general-purpose motion analysis programs, while reference coordinates can be found in single-purpose codes. Due to its wider application, the set of generalized coordinates analyzed in this chapter will be the reference point.

Regardless of the multibody system and the coordinate system chosen to characterize it, a kinematic problem is always based on solving the constraint equations (Schiehlen 2006). The constraint equations arise from the description of the system topology and establish the relation between the independent variables - input elements used to drive the system- and the dependent variables – the rest of the bodies of the system - (Flores 2015). Besides these kinematic constraint equations, the values of the input elements' motion are by itself also constraints – we constrain its value, by defining it. These are usually called driving constraints. The set of all kinematic constraint equations is denoted by symbol Φ. If the total number of coordinate parameters characterizing a system is *n* and the number of degrees of freedom is *k*, then $m = n - k$ is the number of independent kinematic constraint equations of the system. The solution of a kinematic initial position problem is then given by the following expression,

$$\Phi(\mathbf{q}) = 0 \qquad \text{Equation 2.10}$$

where the set of Φ equations depends on the parameters of generalized coordinate vector q. In addition, there are the *k* driving constraint equations. These are appended to the original kinematic constraint equations, giving a total number of *n* equations. The driving constraint are equations representing each independent coordinate as a function of time (Nikravesh 1988). These are defined as follows,

$$\Phi^{(d)} = \Phi(\boldsymbol{q}, t) = 0 \qquad \text{Equation 2.11}$$

where $\Phi^{(d)}$ depends only on the input parameters of q and of time t - only if these parameters are not constant in time. In general, kinematic constraint equations may also be functions of time, but those are special cases called non-holonomic joints. In this case are only considered algebraic equality constraints also known as holonomic kinematic constraints.

To solve systems of nonlinear equations such as Equation 2.10, it is usual to resort to the well-known Newton-Raphson method which has quadratic convergence in the neighborhood of the solution. This means, the error in each iteration is proportional to the square of the error in the previous iteration. Furthermore, it hardly brings complications if the starting point is a good initial approximation. It is possible to transpose its principle to the kinematic problem

case with the set Φ of all kinematic constraints. The substitution of Equation 2.10 by the first two terms of Fourier series results in a system of linear equations as follows,

$$\Phi(\boldsymbol{q}, t) \cong \Phi(q_0) + \Phi_q(q_0) \times (\boldsymbol{q} - q_0) = 0 \qquad \text{Equation 2.12}$$

where matrix Φ_q is the Jacobian matrix for constraint equations in q_0. That is, the matrix of partial derivatives of equations with respect to the coordinates' parameters. This matrix has *mxn* dimension, where *m* is the number of kinematic constraint equations and *n* the total number of variables of all coordinates. It will be seen that the Jacobian matrix of the kinematic constraints is extremely important in all kinematic and dynamic analysis problems. Matrix Φ_q can be defined through the following expression:

$$\Phi_q = \begin{bmatrix} \dfrac{\partial \Phi_1}{\partial q_1} & \dfrac{\partial \Phi_1}{\partial q_2} \cdots & \dfrac{\partial \Phi_1}{\partial q_n} \\ \dfrac{\partial \Phi_2}{\partial q_1} & \dfrac{\partial \Phi_2}{\partial q_2} \cdots & \dfrac{\partial \Phi_2}{\partial q_n} \\ \vdots & \vdots \ddots & \vdots \\ \dfrac{\partial \Phi_m}{\partial q_1} & \dfrac{\partial \Phi_m}{\partial q_2} \cdots & \dfrac{\partial \Phi_m}{\partial q_n} \end{bmatrix} \qquad \text{Equation 2.13}$$

Equation 2.12 represents a system of linear equations constituting an approximation to the nonlinear system. This way it is possible to implement the recursive process to approximate vector *q* to its solution – when all the values of $\Phi(q)$ are under a certain threshold. At that point, the initial position analysis would be complete.

In general, *q* is not explicitly defined in respect to time, therefore it cannot be differentiated to obtain $\dot{q}$ and $\ddot{q}$. An alternative approach the first- and second-time derivatives of the constraint equations are used to yield the kinematic velocity and acceleration equations (Nikravesh 1988). As is the case for initial position problems, for velocity and acceleration cases, the value of *k* velocities and *k* accelerations – driving elements - must be known to solve the kinematic velocity and acceleration equations for the other dependent elements. The velocity equations that result from the time derivative of Equation 2.10 and Equation 2.11 are:

$$\Phi_q \dot{\boldsymbol{q}} = 0$$

$$\Phi_q^{(d)} \dot{\boldsymbol{q}} + \Phi_t^{(d)} = 0 \qquad \text{Equation 2.14}$$

$$\begin{bmatrix} \Phi_q \\ \Phi_q^{(d)} \end{bmatrix} \dot{\boldsymbol{q}} = \begin{bmatrix} 0 \\ -\Phi_t^{(d)} \end{bmatrix}$$

Which represent *n* algebraic equations and where Jacobian matrixes Φ_q and $\Phi_q^{(d)}$ have dimension *mxn* and *kxn*, respectively. $\Phi_t^{(d)}$ is the vector of partial derivative of the driving constraint equations with respect to time and $\dot{q}$ is the vector of velocities of the coordinate

parameters. When a driving constraint has a simple form, such as, $q_i = f_i(t)$ for the i-driving element, then $\Phi_t^{(d)}(i)$ is equal to the time derivative of $f_i(t)$. Basically, for those cases, matrix $\Phi_q^{(d)}$ becomes a matrix with only zeros and ones, and vector $\Phi_t^{(d)}$ possesses the values of velocity of the driving elements in respect to time (Nikravesh 1988).

Through Equation 2.14 it is possible to obtain the values for the velocities of all elements if the position of the multibody system and the velocity of the input elements is known. As for the initial position problem, the matrix that controls the velocity problem is the Jacobian matrix of kinematic constraint equations. The major difference between the two problems is the fact that the position problem equations are mainly non-linear, while the equations governing the velocity problem are linear. This means, there is no need for iterative processes - they can be solved by any usual method adopted for the solution of systems of linear equations (Flores 2015). In addition, there is only one possible velocity solution if the problem is properly formulated (Schiehlen 2006).

To obtain the acceleration equations it is necessary to derive in relation to time the previous velocity equations. This results in the following expressions,

$$\Phi_q \ddot{q} + \dot{\Phi}_q \dot{q} = \Phi_q \ddot{q} + (\Phi_q \dot{q})_q \dot{q} = 0$$

$$\Phi_q^{(d)} \ddot{q} + (\Phi_q^{(d)} \dot{q})_q \dot{q} + 2\Phi_{qt}^{(d)} \dot{q} + \Phi_{tt}^{(d)} = 0 \qquad \text{Equation 2.15}$$

$$\begin{bmatrix} \Phi_q \\ \Phi_q^{(d)} \end{bmatrix} \ddot{q} = - \begin{bmatrix} (\Phi_q \dot{q})_q \dot{q} \\ \left(\Phi_q^{(d)} \dot{q}\right)_q \dot{q} + 2\Phi_{qt}^{(d)} \dot{q} + \Phi_{tt}^{(d)} \end{bmatrix}$$

where Φ_{qt}^d is the vector of partial derivative of Φ_t^d in respect to q – which is zero for the cases described above where driving $q_i = f(t)$ – and Φ_{tt}^d is the vector of second order partial derivatives of the driving constraints in relation to time. The term $-(\Phi_q \dot{q})_q \dot{q}$ is usually referred as the right side of the kinematic acceleration equations and is represented by a variable γ,

$$\Phi_q \ddot{q} = \gamma \qquad \text{Equation 2.16}$$

Similar to the velocity analysis, the determination of the acceleration vector $\ddot{q}$ requires the position and velocity of all bodies in the system and the acceleration values of the input elements. This system of equations is once again composed of linear equations and its leading matrixes are exactly the same as the velocity problem, Φ_q and Φ_q^d. This means, the Jacobian matrixes only need to be factorized once during each step to solve the velocity and acceleration problems (Nikravesh 1988). After the former problem is addressed, it is only necessary to generate the right-hand side of Equation 2.15 and then solve the linear system of equations to obtain the acceleration vector $\ddot{q}$.

2.1.3.2 Dynamic Analysis

As was mentioned at the beginning of this chapter, a dynamic problem consists in analyzing the motion of a multibody system when external forces or torques are involved. In a forward dynamic problem, the forces and torques are an input of the problem which are then used to calculate the motion of the degrees of freedom. In an inverse dynamic case, the external forces and torques are calculated for a specific input motion.

In a dynamic problem the number of coordinate variables is higher than the total number of kinematic and driving constraint equations. In other terms, the motion of the multibody system cannot be unequivocally determined by only knowing the geometric and driving constraint equations. To determine its motion, dynamic equilibrium conditions must be established. Such an equilibrium relates the external forces and torques applied to a body with its capacity to move – inertia – through time. Establishing those relations leads to a system of second order differential equations also known as equations of motion (Shabana 2013). The solution of a dynamic problem lies on coupling the differential equations of motion with the kinematic constraint equations by introducing Lagrange multipliers to relate the joint reaction forces.

Before addressing this problem, it is first necessary to clarify one aspect regarding the generalized coordinate vector derivatives $\dot{q}$ and $\ddot{q}$. As it was done for the position vector q_i which held all the parameters – translational and rotational - that defined a body's i configuration, it is possible to define vector v_i – for translational and angular velocity – and vector $\dot{v}_\iota$ – for translational and rotational accelerations.

$$v_i = \begin{Bmatrix} \dot{r}_\iota \\ \boldsymbol{\omega_i} \end{Bmatrix} = \begin{Bmatrix} \dot{x}_\iota \\ \dot{y}_\iota \\ \dot{z}_\iota \\ \omega_x \\ \omega_y \\ \omega_z \end{Bmatrix} \qquad\qquad \dot{v}_\iota = \begin{Bmatrix} \ddot{r}_\iota \\ \dot{\boldsymbol{\omega}}_\iota \end{Bmatrix} = \begin{Bmatrix} \ddot{x}_\iota \\ \ddot{y}_\iota \\ \ddot{z}_\iota \\ \dot{\omega}_x \\ \dot{\omega}_y \\ \dot{\omega}_z \end{Bmatrix}$$

Note that vector v_i does not correspond to the derivative of vector q_i. Although the derivative of the translational parameters of q_i are indeed equal to $\dot{r}_\iota$, the same is not true for the rotational parameters p_i as they can be represented by different rotational principles. Now it is necessary to find a relation between the rotational parameters of q_i and the angular velocity vector ω_i. As would be expected this relation depends on the type of variables used, but the equations are similar for both the Euler parameters and angles.

$$\boldsymbol{\omega} = 2G\dot{\boldsymbol{p}} \qquad\qquad\qquad \text{Equation 2.17}$$

$$\boldsymbol{\omega} = R\dot{\boldsymbol{p}} \qquad\qquad\qquad \text{Equation 2.18}$$

This Equation 2.17 relates vector $\boldsymbol{p}$ – with rotational Euler parameters – derivative with the angular velocity vector $\boldsymbol{\omega}$ through a *3x4* matrix G. This matrix results from mathematical treatment of the transformation matrix A and is defined as follows.

$$G = \begin{bmatrix} -e_1 & e_0 & -e_3 & e_2 \\ -e_2 & -e_3 & e_0 & -e_1 \\ -e_3 & -e_2 & e_1 & e_0 \end{bmatrix}$$

For the Euler angles case, Equation 2.18 relates the derivatives of those angles with the angular velocity vector through matrix R. This matrix performs the transformation from the Euler-axis frame to the global frame and is defined as follows (Paul 1984).

$$R = \begin{bmatrix} cos\sigma & sin\psi \, sin\sigma & 0 \\ sin\sigma & -sin\psi \, cos\sigma & 0 \\ 0 & cos\psi & 1 \end{bmatrix}$$

To relate the angular acceleration vector $\dot{\boldsymbol{\omega}}$ of a rigid body with the second order derivative $\ddot{\boldsymbol{p}}$ of the angular variables, Equation 2.17 and Equation 2.18 must be differentiated with respect to time. In case of Euler parameters, this results in the following equations,

$$\dot{\boldsymbol{\omega}} = 2G\ddot{\boldsymbol{p}} + 2\dot{G}\dot{\boldsymbol{p}}$$

<div align="right">Equation 2.19</div>

$$\dot{\boldsymbol{\omega}} = 2G\ddot{\boldsymbol{p}}$$

Where $2\dot{G}\dot{\boldsymbol{p}}$ is equal to zero, due to mathematical relations on the generation of matrix G. For the Euler angles, the differentiation of Equation 2.18 becomes,

$$\dot{\boldsymbol{\omega}} = R\ddot{p} + \ddot{R}\dot{p} \qquad\qquad \text{Equation 2.20}$$

With this, we can now relate all coordinate variables with the motion of a rigid body. This is an important aspect since it allows the conversion of angular velocities and accelerations to $\dot{\boldsymbol{p}}$ and $\ddot{\boldsymbol{p}}$ vectors or vice-versa.

The equations of motion relate the forces and torques exerted on a body with its motion through the following equations,

$$M\ddot{\boldsymbol{r}} = \boldsymbol{f} \qquad\qquad \text{Equation 2.21}$$

$$I\dot{\boldsymbol{\omega}} + \widetilde{\omega}I\boldsymbol{\omega} = \boldsymbol{n} \qquad\qquad \text{Equation 2.22}$$

where Equation 2.21 - Newton's Second Law Equation – is a matrix of equations consisting of three scalar equations that relate the forces and accelerations of the center of mass of a rigid body in space, where M is the mass matrix and $\boldsymbol{f}$ represents the sum of all forces exerted

on the body. These three equations are considered the translational equations of motion. Equation 2.22 – Euler's Equation – carries the equations of motion responsible for the rotational component of the body. These equations define the orientation of the body for a given set of moments n acting on the body through the usage of matrix I - the global inertia tensor.

The mass matrix M in space is an *3x3* identity matrix multiplied by m_i if the origin of the body's reference frame is attached to the center of mass of the body, where m_i is the total mass of body i. Inertia matrix I gives an idea on how the mass of a rigid body is distributed in space. Thus, this matrix is composed by the moments and products of inertia of the body referred to the global frame of reference.

Having exposed the two geometric matrixes, it is then possible to combine both Equation 2.21 and Equation 2.22 in a single matrix equation form also known as Newton-Euler formulation,

$$\begin{bmatrix} M_i & 0 \\ 0 & I_i \end{bmatrix} \begin{Bmatrix} \ddot{r}_i \\ \dot{\omega}_i \end{Bmatrix} + \begin{Bmatrix} 0 \\ \widetilde{\omega}_i I_i \omega_i \end{Bmatrix} = \begin{Bmatrix} f_i \\ n_i \end{Bmatrix}$$

Equation 2.23

It is also possible to further compress this equation into the following form,

$$M_i \dot{v}_i + b_i = g_i$$

where matrix M_i is the mass matrix of body i, vector $\dot{v}_i$ is the body acceleration vector, vector b_i contains the quadratic velocity terms and g_i is the body force and torque vector (Nikravesh 1988).

These are the equations of motion for an unconstrained body in three dimensions. It is then possible to formulate a hypothetical multibody system with b unconstrained elements - without any joint connecting them – in which these elements are actuated by external forces, such as, gravity, and by internal forces, such as, spring or damping forces between each other. Such an unconstrained multibody system would be expressed by the following Newton-Euler matrix equation,

$$\begin{bmatrix} M_1 & 0 & \ldots & 0 \\ 0 & M_2 & \ldots & 0 \\ \vdots & \vdots & \ddots & 0 \\ 0 & 0 & 0 & M_b \end{bmatrix} \begin{bmatrix} \dot{v}_1 \\ \dot{v}_2 \\ \vdots \\ \dot{v}_b \end{bmatrix} + \begin{bmatrix} b_1 \\ b_2 \\ \vdots \\ b_b \end{bmatrix} = \begin{bmatrix} g_1 \\ g_2 \\ \vdots \\ g_b \end{bmatrix}$$

Equation 2.24

$$M\dot{v} + b = g$$

Where M is the diagonal matrix of all M_i mass matrix elements and the following vectors $\dot{v}$, b and g are the acceleration, quadratic velocity, and external forces of all bodies, respectively. It is important to refer that vector g includes all the external and internal forces exerted on each body, even if the internal forces cancel themselves in the overall system. Basically, this vector g is composed by multiple vectors g_i which represent the sum of all the load acting on body i on each force and torque direction.

Now we will turn to a more realistic case, considering a multibody system with kinematic joints connecting different elements. To do so, it is necessary to account the geometric relations these connections establish. Recalling that the kinematic constraint equations are responsible for this function, their short form is here again exposed.

$$\Phi_q(\mathbf{q}) = 0$$

<div style="text-align:right">Equation 2.10</div>

Each of these kinematic joints introduces forces to restrict the relative movement between bodies. At each joint, there are as many force reactions as there are degrees of freedom that the joint prevents. Let us take a spherical joint as an example. It allows relative movement in three rotating axes, and, therefore, imposes three force reactions. A revolute joint imposes three reaction forces and two reaction torques since the next body is only free to rotate around one axis. And so forth, for the other joint types. These forces and torques - created due to the geometric constraints of a joint - are referred as constraint forces and can be denoted by vector $\boldsymbol{g}^c$,

$$\boldsymbol{g}^c = [g_1^c \quad g_2^c \quad \cdots \quad g_b^c]^T$$

where each $\boldsymbol{g}_i^c$ is the six-dimension vector with the sum of all joint reaction forces and torques acting on body i. These reaction forces are also internal to the system, which means each body will exert a force of the same magnitude and opposing directions on the other. The sum of vector $\boldsymbol{g}^c$ and external forces vector $\boldsymbol{g}$ is equal to all the forces acting on the system (Nikravesh 1988). Therefore, Eq. Equation 2.24 can be modified to.

$$M\dot{\boldsymbol{v}} + \boldsymbol{b} = \boldsymbol{g} + \boldsymbol{g}^c$$

<div style="text-align:right">Equation 2.25</div>

With this, Equation 2.10 and Equation 2.25 represent the equations of motion of a system with constrained elements, where $\boldsymbol{g}^c$ corresponds to the forces associated with the kinematic joint restrictions, that is, the forces necessary for the constraint equations to be satisfied (Ling et al. 1994).

It is now necessary to understand how $\boldsymbol{g}^c$ can be obtained. The kinematic constraint equations are formulated on the generalized coordinate system represented by vector q. However, Equation 2.25 is referred to the $\dot{v}$ vector. Therefore, it is first necessary to establish a transformation expression that allows the conversion of vector $\boldsymbol{g}^c$ into vector $\boldsymbol{g}^{*c}$ - consistent with the coordinate system $\boldsymbol{q}$ - and vice versa. When this is known, it is then necessary to conceive the relationship between vector $\boldsymbol{g}^{*c}$ and the constraint Equation 2.10. (Flores 2015)

For the transformation from $\boldsymbol{g}^c$ to $\boldsymbol{g}^{*c}$ the translational parameters of $\boldsymbol{g}^c$ - regarding the joint reaction forces – remain the same, but that is not the case for the rotational part of the vector – constraint torques $\boldsymbol{n}^c$. Obviously, the transformation equation depends on the angular parameters used in $\boldsymbol{q}$. When the rotational coordinates are represented by the Euler parameters, then the following equation is utilized.

$$n_i^c = \frac{1}{2} G_i n_i^{*c}$$ <div style="text-align: right">Equation 2.26</div>

Where n_i^{*c} is the vector of constraint torques acting on body i, represented in vector $\boldsymbol{q}$ coordinate system and G_i is the matrix obtained from the rotation matrix of Euler parameters introduced in Equation 2.17.

Now that was presented how it is possible to convert $\boldsymbol{g^*}$ to $\boldsymbol{g^c}$ for the Euler parameters case, it is then necessary to relate vector $\boldsymbol{g^*}$ with the constraint Equation 2.10. Through the virtual work formulation and further mathematical processing, the following equation is derived (Nikravesh 1988).

$$g^{*c} = \Phi_q^T \lambda$$ <div style="text-align: right">Equation 2.27</div>

Where λ is a m-vector of Lagrange multipliers and Φ_q^T is the *nxm* transposed Jacobian matrix of constraint equations. This vector λ establishes the magnitude of the constraint forces (Shabana 2013). With this system of equations, vector $\boldsymbol{g^c}$ can be calculated. Then it is only necessary to apply Equation 2.26 to obtain the joint torque reactions on the proper coordinate system $\dot{v}$. Substituting that equation in Equation 2.25 the following expression is obtained,

$$
\begin{bmatrix}
m_1 I & 0 & & 0 & & & \\
0 & J_1 & & & & \cdots & 0 \\
& & m_2 I & 0 & & \cdots & 0 \\
& 0 & 0 & J_2 & & & \\
& & & & \ddots & & \vdots \\
\vdots & \vdots & & & m_b I & 0 \\
0 & 0 & & & & 0 & J_b
\end{bmatrix}
\begin{Bmatrix}
\ddot{r}_1 \\ \omega_1 \\ \ddot{r}_2 \\ \dot{\omega}_2 \\ \vdots \\ \ddot{r}_b \\ \dot{\omega}_b
\end{Bmatrix}
+
\begin{Bmatrix}
0 \\ \tilde{\omega}_1 I_1 \omega_1 \\ 0 \\ \tilde{\omega}_2 I_2 \omega_2 \\ \vdots \\ 0 \\ \tilde{\omega}_b I_b \omega_b
\end{Bmatrix}
=
\begin{Bmatrix}
f_1 \\ n_1 \\ f_2 \\ n_2 \\ \vdots \\ f_b \\ n_b
\end{Bmatrix}
+
\begin{Bmatrix}
f_1^c \\ \frac{1}{2} G_1 n_1^{*c} \\ f_2^c \\ \frac{1}{2} G_2 n_2^{*c} \\ \vdots \\ f_b^c \\ \frac{1}{2} G_b n_b^{*c}
\end{Bmatrix}
$$

This is the final form of the Newton-Euler formulation for the equations of motion of a multibody system. This formulation results in the establishment of a mixed set of differential and algebraic equations, which can be solved to calculate the dynamic behavior of a multibody system. This approach is very straightforward in terms of assembling the equations of motion and providing all joint reaction forces (Flores 2015).

There are also other possible options besides the Newton-Euler to formulate the equations of motion of a system. The Euler-Lagrange formalism has the advantage of using any coordinate system q, instead of transferring the constraint reaction forces to $\dot{v}$ format like the Newton-Euler case. This advantage makes the generation of equations of motion much more flexible to different multibody systems since any set of coordinates can be utilized.

Consider a constrained multibody system characterized by the coordinate vector $\boldsymbol{q}$ with n dependent coordinates that satisfies m independent constraint equations $\Phi(q,t) = 0$. The Lagrange equation that describes such a system is as follows,

$$\frac{d}{dt}\left(\frac{\partial L}{\partial \dot{\boldsymbol{q}}}\right) - \frac{\partial L}{\partial \boldsymbol{q}} + \Phi_q^T \lambda = \boldsymbol{Q}_{ex}$$
<div align="right">Equation 2.28</div>

where L is the *Lagrangian* function equal to the kinetic energy $T(q, \dot{q})$ subtracted by $V(q)$ the potential energy. $\boldsymbol{Q}_{ex}$ is the vector of generalized external forces acting along vector q and $\Phi_q^T \lambda$ is the augmented term that uses the m Lagrange multipliers λ to introduce the joint constraint forces. In case the coordinate system was constituted by only independent variables, then there would be no augmented term (Shabana 2013).

Through more mathematical treatment of Equation 2.28 and recurring to the virtual power method – assumes no work is done by the joint reaction forces – it is possible to obtain the following expression (Lynch and Park 2017),

$$M\ddot{q} + \phi_q^T \lambda = \boldsymbol{Q}$$
<div align="right">Equation 2.29</div>

where the first term represents the inertial forces, the second, the forces imposed by kinematic constraints, and $\boldsymbol{Q}$ accounts for all external forces and the additional velocity-dependent inertial forces $\tilde{\omega}_i I_i \boldsymbol{\omega}_i$.

With this formulation, Equation 2.29 possesses an increased number of unknowns to be calculated. n unknowns of the vector $\boldsymbol{q}$ and m unknowns of the lagrangian multipliers λ. This means, it is necessary to add m more equations. The immediate choice is to use the m constraint equations, which along with Equation 2.29 constitute a set of differential algebraic equations - DAEs. To avoid solving DAEs and to simplify the system of equations, it is best to differentiate the kinematic equations with respect to time into their acceleration level. That step was already exposed for the kinematic acceleration solution with Equation 2.16, which is here again presented,

$$\Phi_q \ddot{\boldsymbol{q}} = \boldsymbol{\gamma} = -(\Phi_q \dot{\boldsymbol{q}})_q \dot{\boldsymbol{q}}$$
<div align="right">Equation 2.16</div>

Now it is possible to couple Equation 2.16 with Equation 2.29 to obtain the final expression of the Euler-Lagrangian equations of motion,

$$\begin{bmatrix} M & \Phi_q^T \\ \Phi_q & 0 \end{bmatrix} \begin{Bmatrix} \ddot{\boldsymbol{q}} \\ \lambda \end{Bmatrix} = \begin{Bmatrix} \boldsymbol{Q} \\ \boldsymbol{\gamma} \end{Bmatrix}$$

Besides the already mentioned flexibility that this dynamic formalism has in adapting to different multibody systems, its main advantage is the minimum effort needed to calculate the forces associated with each kinematic constraint. This procedure possesses many advantages relative to Newton-Euler formalism because it involves the solution of a smaller set of equations – depending on the chosen vector q -, and still generates accurate results in configurations close to singular positions of the multibody (Flores 2015). Another favorable aspect of using this

formulation is its simplicity to implement in a numerical integration algorithm (Lynch and Park 2017). Anyway, for both formalisms the final matrix of equations can be solved using numerous numerical algorithms.

2.1.4   Motion Analysis Programs

There are many programs available in the market to solve multibody system problems, such as MSC ADAMS®, OpenSim®, RecurDyn® and MATLAB® Simscape. Nowadays there are appropriate Multibody Simulation (MBS) programs to solve every type of multibody mechanism. From large and complex systems to machines or musculoskeletal - muscular and skeletal - aggregates. During the 1990s, the automotive industry was one of the first sectors to establish MBS software in the vehicle design and process development (Blundell and Harty 2015). Besides the car industry, these programs are also used in aerospace and aircraft business for testing virtual prototypes of landing gears or automatic satellite altitude control systems, or in the general machinery industry to analyze robotic systems, industrial machines, or even devices such as electrical relays (Welch 2019).

Inside the available motion analysis options there is a distinction between general- or single-purpose programs. General-purpose programs are known for their flexibility in addressing a very large set of problems across a wide range of engineering industries (Blundell and Harty 2015). With this MBS programs is possible to build and analyze models from door latches to spacecrafts, unlike single-purpose tools which are specifically developed for a given type of simulation. In these programs, the numerical models are fixed, and the user can only modify its parameters. For this reason, single-purpose programs are much easier to work with and present faster results, but then lack the flexibility to simulate different systems.

The *software* chosen to assist the development of this work was MSC ADAMS®. This program is one of the main driving tools for the development of many products in varied industries. It is used by many companies to analyze motion performance for kinematic validation, joint reactions, clearances and collisions, motor and actuator sizing, work-cycle times, and precise positioning (MSC Software Corporation 2002). Although its wide range of applications, the industry with the most intensive use of this program is the automotive sector (Jadav and Gautam 2014).

ADAMS is in fact the name for a wide family of *software* products offered by MSC. There are many program packages to choose from, each one more oriented toward a specific industry or set of problems. The core package includes a general-purpose modeling environment named ADAMS/View, the numerical solver ADAMS/Solver, and a post-processing environment ADAMS/PostProcessor.

2.2 Structural Analysis

In any product design it is imperative to evaluate if the mechanical components used are strong and durable enough to withstand the loads from the desired operating conditions. Can a stand used in a parade hold the weight of all spectators? Until which driving velocities can a moto rider helmet protect its user? How can a building resist an earthquake? To answer these types of questions is necessary to assess the physical integrity of the whole mechanical system or some specific component. Structural analysis techniques are employed to answer different questions regarding a specific component or entire assemblies. They can be applied to solve static, buckling, vibration, frequency responses, and others (Udeyo 2021). The engineer has to decide which type of problem or set of problems are of interest for the intended function of the product.
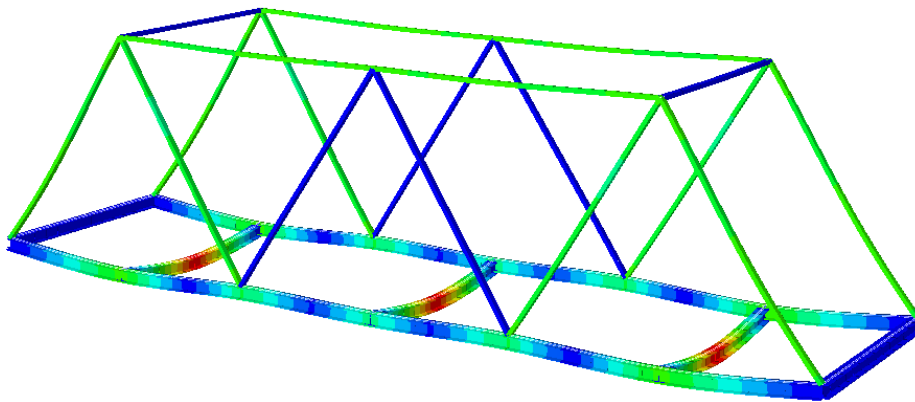
Figure 2.6 - Example of the structural analysis results for a trussed bridge under load

Structural analyses are based on series of mechanical theories and physical laws that are comprised together to predict the behavior of structures under external loads. It includes the fields of mechanics and dynamics as well as the many failure theories. To perform an accurate analysis a structural engineer must gather the necessary data of the problem, such as structural load values, geometry, boundary conditions, materials properties, and so on. The objective of structural analyses usually involves the study of the support reactions, stresses, and displacements. Those results are then compared to criteria that indicate the conditions of failure. These techniques are a great tool used to estimate the performance of a product and its structural integrity without the need of experimental tests (Chang 2015).

Structural analyses can be separated in two categories regarding the techniques used to solve its problems: the analytical methods and the numerical methods. The former methods are based on analytical formulations for simple linear elastic problems, leading to mathematical expressions solvable by hand. These formulations are constructed upon many assumptions to facilitate the equations generation. The assumptions state that the studied material is elastic, the stresses are linearly related to the strains, the deformations occurred are small and that the material behavior is independent of the load direction (Chang 2015). In other words, the material is isotropic and deforms linearly within the elastic regime. As a consequence, the analytical analyses can only be extrapolated for a small number of real case applications.

Unfortunately, most of the engineering problems are outside of this scope and, therefore, require numerical methods to solve them.

The standard numerical method employed in structural design is the finite element method (FEM) (Werkle 2021). It relies on numerical algorithms for solving differential equations formulated upon mechanical theories. The equations that govern a physical problem are partial differential or sometimes integral equations. The finite element technique gathers these equations in a matrix form suitable to be solved through implementation of computer algorithms. These are then applied to find approximate solutions for the equation matrix. One of the great advantages of FEM is the capability to be used to solve a large range of systems with arbitrary size and complexity. Nowadays, these numerical methods are a fundamental part of the design process for a wide variety of engineering fields, such as electromagnetism, fluid dynamics, static, dynamic, buckling, or modal analysis (Fu 2018).

2.2.1 Finite Element Method

According to (Werkle 2021) almost all finite element computer programs used for structural calculations are based on the matrix displacement method. This method is used to solve statically indeterminate systems, leading to algebraic linear equations that describe the problem. These equations are then comprised in a single matrix to be solved. The unknowns of the displacement method equations are displacements and rotations. To relate these variables with the external loads, the principle of virtual work is the basic relationship used for the finite element formulation (Bathe 2006).

The finite element method is based upon subdividing (discretizing) the geometry of a component into a huge number of small pieces. The so-called finite elements - an element with finite size or finite number of elements to describe a component. Hence, the complete structure is idealized as an assembly of these individual structural elements. The geometric domain discretized into finite elements is called a mesh. The assembly of these elements is generated upon their kinematic compatibility and static equilibrium conditions (Werkle 2021). At the end points of a finite element edges are what is called nodal points or nodes. These are shared by adjacent elements, establishing the connections between them. The displacements and rotations unknowns – denoted as degrees of freedom - are defined at these points. Which degrees of freedom are assigned to a node depend on the type of the element selected (Szabo and Babuška 2011).

To calculate the structural responses within an element, interpolation functions – usually polynomial - are used to relate the displacements between the element's nodes. This happens because the exact displacement functions in two- and three-dimensional analyses are not known (Bathe 2006). As a consequence, the equilibrium equations cannot be fully satisfied. Although the exact interpolated solutions do not match, the approximation error can be decreased with a higher number of elements or by applying elements with interpolation functions of higher order (Werkle 2021).

Besides the geometric discretization of components, also the forces must be discretized. A linearly distributed force is divided into equivalent point forces applied at the corresponding nodes. Also, the material properties and section properties are discretized in accordance with the finite element mesh. This way a whole complex problem is divided into small fractions with simple static properties and loads (Bathe 2006). Assuming a linear behavior of the system, the

relationship between the applied forces and the element properties allows the formulation of algebraic linear equations with the nodal point displacements and rotations as unknowns (Rieg et al. 2019). This relationship can be written as follows,

$$\boldsymbol{f} = k\boldsymbol{u}$$

where $\boldsymbol{f}$ is the load vector comprised by the forces and moments acting at the node, $\boldsymbol{u}$ is the displacement vector with the node's degrees of freedom and k the element stiffness matrix which defines how much each degree of freedom of the element will displace for a set of forces and moments.

The element stiffness matrix k and the force vector $\boldsymbol{f}$ are assembled with those of all the other elements to form the global stiffness matrix K and the force vector $\boldsymbol{F}$ of the entire system. The element stiffness matrices have to be transposed to the corresponding global reference frame of the structure, and the total stiffness matrix is built based on the compatibility equations at the nodal points. Then, it is possible to formulate the following expression,

$$\boldsymbol{F} = K\boldsymbol{U} \qquad\qquad \text{Equation 2.30}$$

Where $\boldsymbol{F}$ is the load vector with all forces and moments applied at the nodes' degrees of freedom, and K the global stiffness matrix which defines how the entire structure will displace when loads are applied to it. This matrix is square and called Sparse and Banded, because it has many zero elements and the non-zero are grouped around the diagonal. For a linear elastic problem this matrix is symmetric.

After the global stiffness matrix K and the load vector $\boldsymbol{F}$ have been determined, Equation 2.30 is solved through iterative methods employed to take advantage of the matrix sparsity (The Efficient Engineer Channel 2021). The Gaussian elimination algorithm is a common procedure for the solution of linear systems of equations. The size of a matrix equation is determined by the nodes' degrees of freedom for the type of finite element used and the number of nodes created in the component discretization. Depending on the size of the problem, these can be systems of equations with several hundred, thousands, or tens of thousands of unknowns. For this reason, the most consuming computational effort in a finite element analysis is usually the solution of the equation matrix. After solving Equation 2.30 the elements displacements are used to calculate the support reactions and the element stresses (Bathe 2006). In other terms, a finite element analysis is divided in the following steps (Werkle 2021):

- Computation of element stiffness matrices and discretization of nodal point loads
- Assembly of the global stiffness matrix using the element stiffness matrices and assembly of the load vector
- Solution of the matrix equation with displacements as unknowns
- Determination of support reactions
- Determination of the element stresses

To summarize, by going through a component discretization and finite element interpolations, the partial differential equations that describe continuum mechanic problems

are converted into systems of linear equations which can be solved by numerical methods. After the simulation, the element displacements and stresses must be interpreted as an estimate of the actual structure behavior, taking into consideration the mathematical theories related to each element type. A great advantage of FEA is the possibility to use many different structural elements such as beam, shells, and three-dimensional solid elements, each of them based on different physical theories and assumptions. These can all be used in the same computational model, providing a high-level of versatility at the structure characterization (Werkle 2021).

2.2.2   Failure Criteria

After obtaining the numerical results from a finite element analysis, it is necessary to decide which failure criteria is more appropriate for the problem. It is well known that failure of a component occurs when the stress caused by the load reach its strength limit. This strength limit depends on the components' material. For ductile materials failure occurs at the onset of plastic deformation, hence the yield strength σ_{yield} is considered as the limit value. For brittle materials failure occurs at fracture and so the ultimate tensile strength $\sigma_{ultimate}$ is utilized. In the case of uniaxial load, the relation between the material strength and the actual stress is straightforward and well documented (Chang 2015). However, for complex cases of biaxial or triaxial stress state in a component, it is hard to predict its failure. Instead, for a combined stress state, failure is predicted by selecting the most suitable of the failure theories – or criterions - (González-Velázquez 2021). Each of them is more appropriate for certain circumstances than others.

The two most common theories for ductile materials – yield failure – are the Tresca's and Von Mises's criterions (González-Velázquez 2021). The Tresca failure criterion - or maximum shear stress theory - states that yielding occurs when the maximum shear stress is equal to the shear stress at yielding in a uniaxial tensile test. In other words, the shear stress at a ductile component must be smaller than the shear yield strength to ensure a safe design.

$$\tau_{max} = \tau_{yield}$$ Equation 2.31

It is common to express this theory as a function of the principal stresses, instead of a function of the shear stresses. According to Mohr's circle, the maximum shear stress is the difference between the maximum and minimum principal stresses, thus Equation 2.31 can be reformulated as,

$$\sigma_1 - \sigma_3 = \sigma_{yield}$$

Von Mises's criterion – or maximum distortion energy theory - states that yield occurs when the maximum distortion energy is equal to the distortion energy at yielding in a uniaxial tensile test. This can be related by the following equation,

$$\sqrt{\frac{1}{2}[(\sigma_1 - \sigma_2)^2 + (\sigma_2 - \sigma_3)^2 + (\sigma_3 - \sigma_1)^2]} = \sigma_{yield} \qquad \text{Equation 2.32}$$

The left-hand side of Equation 2.32 is usually called as equivalent von Mises stress σ_{eq}. Both criterions agree with experimental tests for ductile materials, although von Mises is more precise. Despite being more conservative, Tresca's criterion was for many years widely used because it is simpler to apply (González-Velázquez 2021).

2.2.3 Safety Factors

Whether analytical or computer-aided methods are employed, none of these structural analysis accounts for variations on the physical parameters neither uncertainties in the physical conditions. In the physical world, loads, material properties, and geometric dimensions are not constant. There are uncertainties in defining the loading conditions or in making assumptions for a solvable mathematical model. These deviations from the physical problem are often addressed by using more conservative approaches. Such approaches typically include safety factors or worst-case scenarios (Chang 2015).

The safety factor approach is the simplest and most widely used in engineering design. By employing this approach, the developed solutions are usually over-dimensioned to overcome any potential problems caused by deviations from the real problem. Determining an appropriate safety factor requires many considerations, such as the degree of uncertainty in the load or in the material properties. The consequences of reaching failure are another important aspect to take into consideration, as well as the cost of selecting a too large safety factor. For some products, there are already established design rules, which enforce a required minimum factor of safety (Szabo and Babuška 2011). In other cases, the product developer has to define an appropriate value. According to (Chang 2015) the following safety factor values can be considered as general guidelines for structural engineering problems:

- N = 1 - 2 for reliable materials used under stable conditions subjected to reliable loads
- N = 2 - 3 for less experimented materials used under average conditions, subject to fairly reliable loads
- N = 3 - 4 for at most one uncertainty in materials, conditions, and loads
- N = 1 - 6 for fatigue problems
- N = 3 - 6 for impact problems

2.2.4 FEA Programs

In general, finite element programs are divided in three major software components for solving structural problems. They are pre-processing, solving, and post-processing.

The pre-processing step starts with creation of a geometric model that tries to resemble as close as possible the structure geometry. This can be directly made in the FEA programs but usually they do not possess large modeling capacity. Therefore, it is preferable to create the geometry of a component in a CAD program and then export it to the structural analysis computer tool. Once the geometric model is available, the discretization in finite elements

may be generated automatically, using mesh generation capability in the FEA program. Usually there is also the option for meshing parts manually, but it is often less desirable, especially for complex geometries. With the parts of the model properly meshed, all material properties, loading and boundary conditions, and interactions between different components must be characterized. At last, the type of simulation and desired outputs have to be specified.

The solving step then takes the discretized mathematical model, formulates the individual element stiffness matrices, assembles them in the global stiffness matrix, imposes the boundary conditions, and solves the system of equations. All these steps are performed automatically by the computer programs. The solutions can be obtained recurring to numerical algorithms such as Gaussian elimination or LU decomposition (Chang 2015).

The analysis results can be visualized in various forms in the post-processing step. Color perimeters or contour plots of the solutions, such as displacement or stress, may be displayed; a deformed shape or animation may be requested to better visualize structural deformation. In Figure 2.7 is shown the typical visualization of numerical results of a structural analysis.

Nowadays, there are several general-purpose FEA programs commercially available. Popular examples are ANSYS®, MSC/Nastran®, and ABAQUS®. Each one of these programs is renowned for its capabilities in solving certain types of structural problems. Nastran is recognized by its overall ability to produce good results in many engineering problems, while Abaqus is deemed one of the best in nonlinear analysis (Chang 2015). The dimensioning process of this thesis work was executed with Abaqus for being an available option and due to previous experience of the author with this FEA program.
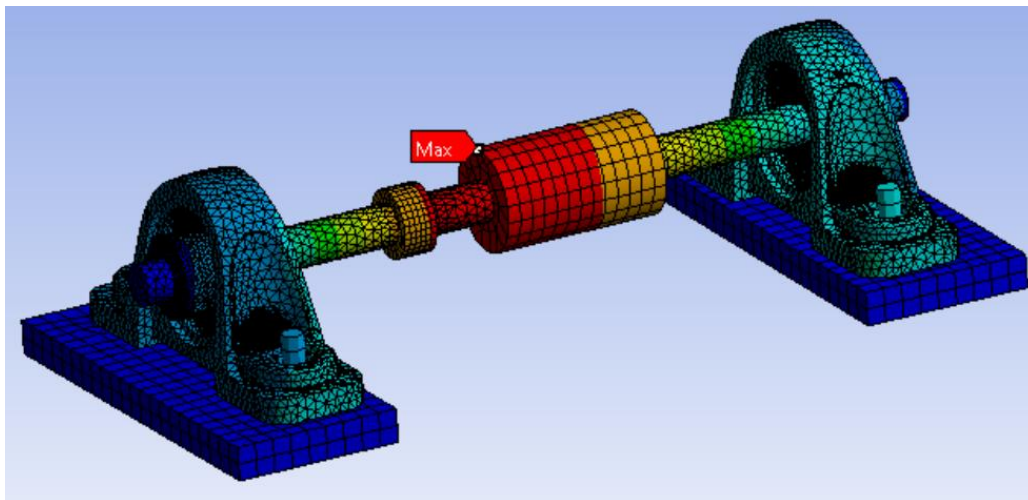
Figure 2.7 – Visualization of the structural analysis results of a shaft and bearing assembly in ANSYS

2.2.5   Finite Element Modeling

To utilize computer-aided tools for structural analyses is first necessary to build a mathematical model. This model should represent the component - or assembly – geometry and describe as closely the physical problem. The finite element program takes all the information from the mathematical model – the differential equations describing the geometry, the kinematics, the material behavior, the loadings and boundary conditions, and other aspects of

the system – to build and solve the equation matrix (Pipinato 2016). It is important to retain that a finite element analysis only solves the defined mathematical model. All the assumptions made for building the structural model impact the numerical results. "It is crucial to shape the physical problem in the most appropriate way to obtain the desired information from the analysis" (Bathe 2006). In the end, the numerical results should be verified regarding the expected physical behavior. Eventually, the mesh can be refined, and other model parameters can be altered to better portray the problem.

The first step to build a structural model is to fully understand the physical problem being considered. This means, recognizing all physical characteristics relevant for the proper characterization of the structural problem. They generally include obtaining the material properties, possessing the components' geometries, defining the boundary conditions, reflecting on the structure behavior, and above all deciding which are the objectives of the analysis (Chang 2015). How is the structure supposed to deform? Is it within the linear elastic regime or not? How is the load applied to the structure - static or time-dependent? How important are other engineering fields for the structure functionality? Are fluid, electric, or thermal aspects relevant for the model? Answering these and other questions helps to identify and properly characterize the desired model and select the most appropriate analysis type.

Then an idealization of the structural model should be conceived. This is important to next simplify the problem into a less complicated version. This is usually necessary for a vast majority of physical situations which are too complex to solve if they were fully described. Thus, a mathematical model can be generated as a simplified representation of the problem by making adequate assumptions to reduce the degree of complexity. However, these assumptions should not be taken with ease. The structural model should still closely portray the desired physical behavior. An assumption should always be supported upon theoretical knowledge or user experience to properly validate that decision. There are many available options to reduce the complexity of a physical problem in FEA programs. According to (Chang 2015) simplifications can "be made by removing nonessential geometric features, reducing 3D structures to 2D or 1D components, converting impacts to equivalent static loads if feasible, fixing the rotating end of the structure for proper boundary conditions, and so forth". Additionally, it is sometimes possible to take advantage of the structure geometry and analyze only a portion of it when there are symmetric conditions.

At last, the discretization of the model. This step depends profoundly on the desired information to take from the structural analysis. Different types of elements are based on different physical theories or possess different behavior under the load. The size of the elements has a deep influence on the simulation duration, and thus it is important to concentrate more elements on relevant regions of the model. The elements shape is another important aspect to properly discretize the geometry at specific locations. All these parameters impact the numerical results obtained. It is the user responsibility to make the best possible decisions with the options available considering the problem at hands.

After the simulation has been executed, the results of the finite element analysis - as with any other computer-aiding tool – should be taken under careful examination (Werkle 2021). FEA programs are a powerful instrument but can be misleading. Erroneous results caused by model mistakes can severely impact design decisions in product development. It is important that each engineer develops a verification procedure to check the numerical results before accepting them as reliable. Then the solutions can finally be interpreted, and the analysis could

be repeated with a refiner mesh, an improved model with more detail or with improvements regarding the optimization of the structure (Pipinato 2016).

2.2.5.1 Simplification

The main purpose of simplifying a structural model is to reduce its size and complexity, promoting a smoother and faster simulation. A smoother simulation has less discontinuities to solve, reducing its chance to find formulation errors or incompatibilities in the equations and abort. These discontinuities may be caused by several factors, such as geometry, load, or interaction between parts. A faster simulation is associated with a lower number of finite elements in the model. In the end, the numerical results obtained for a properly, simplified model must not vary significantly from the results a more complex model – closely representing the physical problem – would obtain. A simplification should not compromise the solution accuracy (Chang 2015).

There are different possibilities to simply a model. One of the best options is to use the model symmetry to largely cut down the number of equations to solve. If the system geometry, material properties, load and boundary conditions are symmetric, then it is possible to utilize this technique. This has the great advantage of drastically reducing the simulation duration, without interfering with the analysis results.

Another possibility is to use dimensional reduction. For three-dimensional problems within the linear elasticity range is possible to reduce 3D components to planar, shell, plate, beam, or truss parts (Szabo and Babuška 2011). A thin planar 3D structure can for example be modeled as a shell surface with a characteristic length. However, these types of simplifications must be guided by the theory behind each element type.

Another usual option is to ease the geometry details of the model. In general, a physical system has complex geometries with intricated shapes, small geometric features, and smooth dimension variations. These characteristics make it hard to discretize the model. In addition, most of these geometric elements have no influence in the structural analysis results. When that is the case, it is possible to suppress, remove, or ease those features to facilitate the solution. However, it is important to mention that features that influence the numerical results must not be removed. One exemplar case are holes that lead to stress concentrations around it.

2.2.5.2 Mesh generation

The geometric discretization – or mesh generation or meshing - of the structural model parts is a crucial step of a finite element analysis. It divides a component in multiple polygonal or polyhedral elements that together try to conform the exact geometry of a region - Figure 2.8. However, this partition of the structural domain cannot be arbitrarily. It has to respect a few necessary conditions.
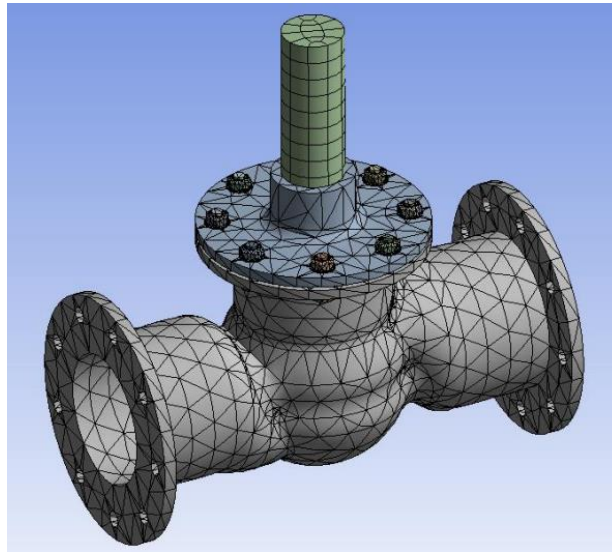
Figure 2.8 – Finite Element discretization of a globe valve model in ANSYS

For start, adjacent finite elements must share common edges and corner nodes. This prevents the elements of the same part to penetrate on one another. The following rule enforces that all elements should have a proper shape. Basically, quadrilateral elements should be close to square shapes, and triangular elements to equilateral triangles. This is achieved by setting restrictions on the elements' angles and aspect ratios to ensure mesh quality (Chang 2015). The mesh quality is an extremely important aspect for the accuracy of the numerical results. More elements approximate the solution to more accurate values but also raises the computational costs. In the end, the virtual model should be discretized in as few elements as possible that result in an approximate solution.

Nowadays, most programs possess powerful methods that enable the automatic generation of finite element meshes (Werkle 2021). These programs consider the components' topology and then select the most appropriate meshing techniques. Depending on the technique employed the user can have more or less control on the discretization process (Dassault Systèmes 2020). Most of the times, it is possible to select the elements' size for the whole part and then choose specific regions with smaller elements to improve the solution accuracy. When performing the mesh generation, the program will try to respect those conditions imposed by the user.

Besides selecting the size of the finite elements, it is also necessary to decide which element type is going to be used. FEA programs offer a wide variety of elements, each of them more appropriate for certain situations than others. In order to obtain the desired structure behavior and closer numerical solutions, a careful decision has to be made regarding the element types. These elements can be divided in their dimensionality – 1D, 2D, or 3D elements - and in the interpolation order – first, second, third, and so on. In the following paragraphs are exposed the finite element types that were important for this work development. For each element are exposed its characteristics, applications, and limitations.

2.2.5.3   Finite Elements Dimensionality

There are two major types of 1D elements - truss and beam elements. A truss element is a linear finite element with one nodal point at each end. This element can only be under tension or compression since it has only one degree of freedom – displacement along the axis – at its nodes. A linear beam element is also defined between two nodal point, but in this element case the nodes have all 6 DOF in spatial situations. Thus, these elements can be subjected to axial and lateral loads, as well as bending and torsion moments.

In FEA programs there are different types of beam elements. In general, they can be divided in two groups depending on the theorical formulation they are based upon – the Euler-Bernoulli beams or the Timoshenko beams - Figure 2.9. The "Euler-Bernoulli" – or slender - beams follow the mechanical theory with the same name which states that plane cross-sections initially normal to the beam's axis remain plane and also normal to that axis during loading. This means that the cross-sections of a beam element remain undistorted, not allowing for transverse shear deformation. This represents a less realistic case, and for this reason, these elements should only be used for slender beams subjected to small strains (The Efficient Engineer Channel 2021). The other beam element type follows the Timoshenko Beam Theory which takes the transverse shear deformation into consideration. This means, the plane cross-sections may not remain normal to the beam axis. This is a more realistic theory and can therefore be used for slender as well as thick beams with large strains and rotations.
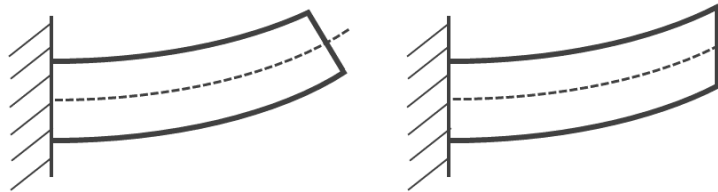
Figure 2.9 - Geometric representation of the deformed Euler-Bernoulli beams (on the left) and Timoshenko beams (on the right)

The 2D elements are planar elements that define a certain surface shape delimited by the nodal points at each end. These element types allow the formulation of structural components with 2D elements, which saves a lot of computer resources. For structural applications they can be divided in plane stress, plane strain or plate/shell elements. Plane stress elements are used to discretize thin structures which can be modeled as 2D sheets in situations where it can be assumed that there are no out-of-plane stresses. On the other hand, plane strain elements can be used to model very thick structures with a defined section, in which out-of-plane deformations can be neglectable. The plate or shell elements are the more general option for 3D structures made of thin layers of material.

In Abaqus, the shell elements are divided in conventional or continuum elements. The former is applied to parts modeled as 2D, which then have the components' thickness attributed as a property. They can be further divided in thick or thin structures if the thickness dimension is higher or lower than 1/15 of the characteristic length, respectively. Thick plates consider the effects of shear deformation, while thin elements take is as neglectable – thus being faster to solve. On the other hand, continuum shell elements are discretized from 3D bodies, but their

kinematic and constitutive behavior is similar to conventional shell elements (Dassault Systèmes 2020). These elements are a good option for slender structures dominated by bending stresses and involving contact with other components.
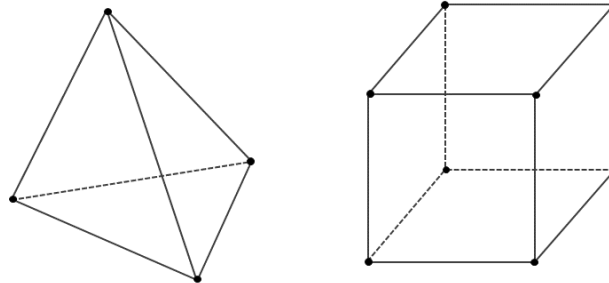
Figure 2.10 - Representation of the tetrahedral shape (on the left) and hexahedral shape (on the right)

For situations where it is impossible to reduce the dimension of a structural component, 3D elements have to be utilized. Regarding their shape, they are commonly divided in tetrahedral or hexahedral (brick) elements - Figure 2.10. The former shape is more geometrically versatile, being therefore more convenient for modeling complex geometric features like sharp edges. However, the hexahedral elements are more efficient, providing a higher solution accuracy with less computational costs.

2.2.5.4 Finite Elements Interpolation Order

In addition to the dimensionality of the finite elements, their interpolation order is another crucial factor. The interpolation degree of a finite element affects the number of nodal points on an element, and - as a consequence - the number of degrees of freedom. In general, most FEA programs utilize finite elements of low interpolation order, usually first, second or third. As was previously mentioned, higher order elements provide higher solution accuracy, but are more expensive regarding the simulation duration. Some types of finite elements have the integration order previously defined by the program. That is, for example, the case of the "Euler-Bernoulli" beams which are third-order elements in Abaqus. In other types of finite elements, the user can select the desired degree of interpolation. For instance, hexahedral elements can usually be defined as first- or second-order elements. Although FEA programs have a default selection for the elements' orders of integration, it is the engineer responsibility to evaluate which is the best option for the problem at hand.

Considering only 3D elements in Abaqus, these can be linear (first-order) or quadratic (second-order) interpolation elements. A linear element has nodal points exclusively at the corners of its shape, while a quadratic element in addition has nodal points in the middle of the edges - Figure 2.11. First-order elements have a constant volumetric strain throughout the element, which is an assumption that makes this element extremely computationally efficient. In addition, these elements are the best option to use in situations involving contact because they depict the contact phenomenon more accurately (The Efficient Engineer Channel 2021). Second-order elements provide higher solution accuracy for problems that do not involve

complex contacts nor severe distortions (Dassault Systèmes 2020). It is helpful to evaluate stress concentration regions and can represent curved surfaces with fewer elements, which is an advantage for problems strongly influenced by bending. Despite its higher accuracy, quadratic elements require more computer power, which in turn makes it sometimes worthier to use a denser mesh with linear elements.
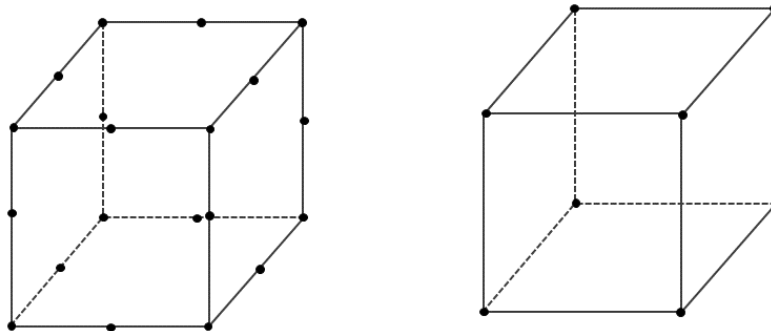
Figure 2.11 - Quadratic (on the left) and linear (on the right) hexahedral elements

2.2.5.5 Hexahedral Elements Integration

In Abaqus there is also the possibility to choose between full or reduced integration for hexahedral elements. The reduced elements were developed to shorten the simulation duration by formulating the element stiffness matrix with a lower-order of integration. They are a good option for problems with severe plastic deformation, causing high mesh distortions. The full integration elements are formulated by the minimum number of integration points to "exactly depict the strain energy for an undistorted element with linear material properties" (Dassault Systèmes 2020). For this reason, the reduced elements have become the default option since they are more efficient for large strain problems.

However, first-order reduced elements have numerical problems associated, in particular Hourglassing. This problem occurs when the elements are distorted similarly to bending situations – tension in half of the element and compression in the other. This creates a strain state that results in zero strain at the integration point, even if the nodes have changed their position. Hourglassing develops because the elements have only one integration point, leading to uncontrolled distortion of the mesh. This may cause the simulation to abort prematurely – due to convergence issues – or generate artificial stresses, resulting from the unphysical behavior associated to this problem. This effect can easily be identified in simulation results by looking at the deformed mesh and checking the existence of hourglass shapes between adjacent elements.

On the other hand, fully integrated elements may suffer from "locking" problems. There are two types of locking possibilities: shear and volumetric locking. Shear locking may develop in first-order fully integrated elements submitted to bending moments, due to parasitic shear. In such cases, the element stiffness becomes artificially higher, producing smaller displacements than it should, inducing large errors in the numerical results. It is usually associated with regions under local high bending strains, especially if the element length has the same or higher order of magnitude than the wall thickness (Dassault Systèmes 2020).

Unfortunately, this problem is not noticeable in the mesh results. To overcome this issue, it is suggested to employ at least three elements along the thickness direction or use other elements such as second-order, first-order with reduced integration, or instead use continuum shell elements (Streamliner 2021).

Volumetric locking occurs with second-order fully integrated elements when the material behavior is incompressible or almost incompressible. This numerical phenomenon develops when plastic strains are on the order of the elastic strains, causing an element to behave too stiffly (Dassault Systèmes 2020). This causes similar numerical problems as the shear locking case. This volumetric locking can be detected by the presence of checkerboard pattern of the pressure stresses at integration points.

2.2.5.6   Contact Interaction

Another important aspect in structural models involving more than one component is the proper characterization of the interaction between different parts. In the physical world, structures and mechanisms are composed of different elements with established relationships. Even if there are no joints allowing relative motion between components, parts are usually connected by some attachment solution – screws, rivets, welding, adhesives, and so on. In addition, parts also react to the geometries of adjacent bodies when they are contacting. One component simply laid on top of another exerts a downward force on the bottom component. In other cases, an element can slide along the surface of another. These different relationships have to be established in FEA programs to closely represent those physical interactions. The mathematical models need to be informed to account the forces generated from two parts contacting each other. Otherwise, components would simply overlap during the simulation, penetrating one another without any resistance.

In general, FEA computer tools have different classes of contact definitions. Abaqus has two main approaches to define this interaction: general contact and contact pairs. General contacts are the simplest to use but also the most computationally expensive. A user only needs to define the properties of a single interaction for the whole model. Then an internal algorithm will automatically detect which regions are likely to get in contact. This algorithm keeps running through the simulation, taking a lot of computer resources, due to the constant search for the potential surfaces in contact. In the contact pair definition, the user must manually define every possible interaction and its properties. This is a more time-consuming task, but also more computationally efficient, since the solver will only consider the formulated contacts, not wasting time searching for other possible contacts. This contact class is based on the master-slave approach.

This is a numerical approach used to represent how the different surfaces interact. One surface is defined has the master, while the other becomes the slave. In this approach the nodes on the slave surface "search" for the master, being prevented to penetrate the other surface. The master surface nodes are "blind", having the possibility to penetrate the slave - Figure 2.12. For this reason, the larger area surface should have the master role. This is more computationally efficient because lesser nodes have to search for the other surface nodes. In cases where both surfaces have close dimensions, then the stiffer component should be selected as master, to prevent the other from penetrating it.
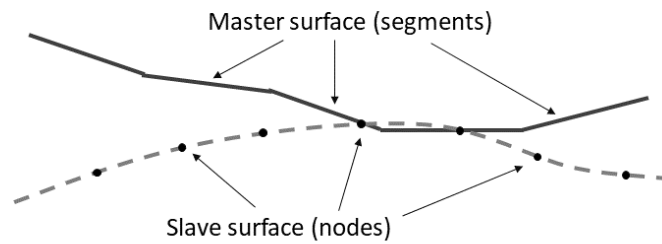
Figure 2.12 - Representation of the master surface penetrating the slave surface

One of the properties that needs to be defined in a contact pair is the tracking approach. This approach describes how the nodes of the different surfaces react to relative movement between the two parts. There are two option available in Abaqus: small- or finite-sliding. Small-sliding is the more efficient option and should be used for situations with small relative motion – little sliding. It establishes the relationship between the slave nodes and the master surface segment at the beginning of the simulation. These connections are then maintained during the solutions, never changing which slave nodes interact with the master surface (Dassault Systèmes 2020). On the other hand, the finite-sliding tracks constantly which part of the surfaces are in contact, increasing the solution duration. This option should be employed for situations with high relative motion.

Another aspect of contact pair relations is the contact discretization. This property defines the locations where the surfaces establish the contact conditions with one another. Abaqus offers to discretization options: "node-2-surface" and "surface-2-surface". The former is a more traditional approach in which each "slave node" interacts with the closest point of the master surface. This point can be one of the "master nodes" or any point along the master surface segment between two nodes. This discretization method is more robust, but less realistic. Contrarily, the surface-2-surface approach "considers the shape of both the slave and master surfaces in the region of contact constraints" (Dassault Systèmes 2020). Therefore, this option presents more realistic results, but is less robust and may fail in geometric regions with sharp edges.

In addition to the contact properties between two surfaces, it is also necessary to describe the nature of the interaction – its physical behavior. These characteristics define the mechanical contact properties regarding the tangential behavior, the normal behavior and damping due to friction. In Abaqus, the normal behavior can be described by different pressure-overclosure formulations. These are responsible for relating the contact pressure in the normal direction with the "slave nodes" penetration in the master surface. Each formulation uses a different mathematical relation to calculate the contact pressures. The most common and realistic formulation is the Hard Contact (The Efficient Engineer Channel 2021). When two surfaces come into contact this formulation generates the necessary contact pressure value to prevent the surfaces from penetrating one another. This poses a numerical challenge since this expression discontinuous. The other formulations – so-called Soft Contact relationships – use mathematical functions as exponential, linear or tabular values to describe contact pressures depending on the penetration. Although easier to solve, these formulations are not realistic. They allow – until a certain extent - penetration to occur and sometimes even generate forces

before the two surfaces come into contact. These options should be used, when the hard contact type is revealing too hard for the simulation to handle.

2.2.5.7 Constraints

In addition to selecting the contact behavior in a structural model, there are other relationships between different components that must be defined. That is the case for connections like screws, rivets, welding, adhesives, and so on. These forms of attachment generate relevant movement constraints between components and thus must also be included in the model. The coupling of one part to another is important to reduce the degrees of freedom of the system. Abaqus offers many constraint options to relate the nodes' DOF of two regions during the analysis.

A tie constraint is used to fuse two separate surfaces together, locking them to one another. The translational and rotational degrees of freedom of both surfaces are made equal. Basically, this constraint acts like a fictional stiff adhesive that binds both surfaces in all their contact area regardless of the load is being applied. This constraint is automatically employed by Abaqus when there are incompatible meshes inside the same component. Since the nodal points of the two regions have no connection, this constraint is used to enforce the same degrees of freedom to all nodes along the interface.

A rigid body constraint is used for parts defined as rigid. These non-deformable components possess no volume, they are only comprised by an assembly of surfaces that correspond to their exterior topology. This constraint is used to restrain all the part surfaces to the motion of a single reference point (RP). With this, all the regions of the rigid body have no relative movement, remaining together as a single entity attached to a reference point. This point is usually positioned at the volumetric center created by the connected surfaces.

One useful constraint utilized for many applications is the coupling constraint. It restrains the motion of a surface to the motion of a single reference point (Dassault Systèmes 2020). The degrees of freedom of the reference point are shared by the surface nodes' degrees of freedom. In other words, the displacements of this control point are divided by all the nodal points in a surface. This division is uniform by default but can be altered to impact more the surface nodes close to the RP. This constraint is commonly utilized to applied loads or boundary conditions to the model. The load can be applied at the reference point and then distributed across the desired surfaces.

Another relevant type of constraint is the MPC – multi-point constraints. This is a constraint similar to the coupling one, but instead of connecting surfaces to one specific point, it connects any desired nodal points in the model to a single point. This allows constraints to be imposed between any degrees of freedom of the model. There are different classes of MPC constraints, like for example the Beam class which restrains all DOF of the selected "slave nodes".

2.2.5.8 Singularity Points

After a finite element analysis has been performed, it is important to verify the results obtained. The stress pattern, the deformed model and the boundary conditions should be observed to evaluate the reliability of the results with the expected physical behavior.

Sometimes a convergence study may be necessary to ensure that discretization errors are not affecting the solution. However, during these convergence studies might occur a special phenomenon known as singularity point.

A singularity point is a nodal point in which the internal forces grow permanently with higher mesh densities. The results in this point do not converge, continuously increasing its value. These occur at locations with inadequate structural modeling or concentrated loads. They are typically associated with geometrically prominent points like sharp corners or re-entrant corners in plates (Werkle 2021). The results in these regions are physically meaningless as the stresses are artificially high and can therefore be neglected if there is no interest in that specific region of the model (Bathe 2006). Singularities can be avoided by rounding out sharp features in the model or distributing the concentrated loads over an area.

3   Industrial Robot Dynamic Load

3.1   Mechanical Validation of Adams

Although computer-aided approaches are now established as practical solution to many engineering problems, it is important to understand the analytical methods that lead to the solution of a problem. It is critical to verify the numerical results obtained from CAE programs, whether through experimental or analytic analysis. The demonstration of the reliability of a mathematical model is an essential part of any numerical analysis (Chang 2015). Unfortunately, for complex problems these options are not available neither practical. When that is the case, it is a good practice to formulate a simple system to obtain its analytic solutions and later compare those with the numerical results.

In the next sections, the static and dynamic analyses for a simple one degree of freedom mechanism are exposed. The solutions of these problems were then compared with results obtained for a virtual system modeled with the same characteristics in ADAMS. This verification process was performed to perceive the closeness of the two distinct methods and also to get a first contact with the capabilities of the program.

3.1.1   Statical Verification

To perform the validation of the results obtained from the two sources a simple mechanism with 1 degree of freedom was chosen. A scheme of the chosen planar mechanism is represented next in Figure 3.1.
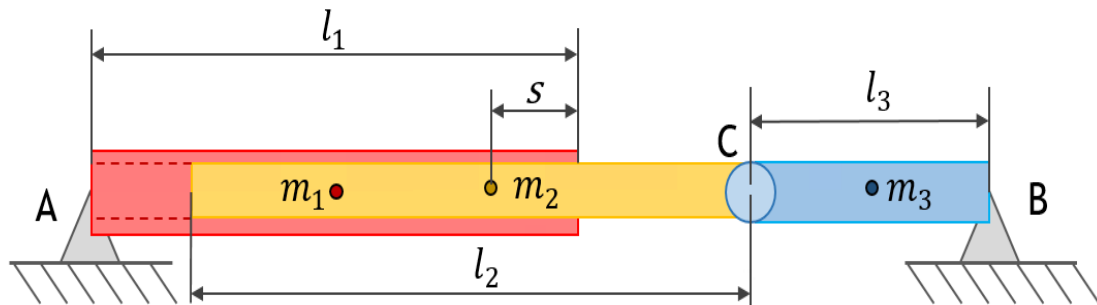
Figure 3.1 – Scheme of the studied mechanism

This is a three body mechanism with three revolutes joints at A, B and C, which results in a system with one degree of freedom. The third body (driver) rotates around joint B driving the second body (slider), which in turn is free to slide inside the first body (cylinder). Joints A and B are fixed at the same height with a distance $L = 600mm$ from one another. Bodies 2 and 3 were considered links (bars), while the first body a hollow cylinder with a through hole along its axis. This was an important aspect to ensure that the center of mass of each body was positioned in the middle of its length. To each body was attributed a length and mass as follows.

$$\begin{cases} l_1 = 375mm \\ l_2 = 400mm \\ l_3 = 125mm \end{cases} \qquad \begin{cases} m_1 = 3kg \\ m_2 = 1kg \\ m_3 = 0{,}5kg \end{cases}$$

After that, the variable that represents the degree of freedom of the system had to defined. In addition, other auxiliar variables also had to be chosen to help on the formulation of the mathematical equations. The obvious choice for the degree of freedom was the angle that the driver creates relative to the horizontal global plane – angle θ. Besides this angle, it helped in further calculations to define angle α which equals the angular displacement between the cylinder and the horizontal plane. It was also noted to be advantageous to set a auxiliar variable s, which represents the distance between the second body center of mass and the tip of the first. This parameter was chosen to be negative, if body's 2 center of mass was inside the cylinder hole. Thus, in Figure 3.1 s has a negative value.

For this problem, it was assumed that the only external forces applied to the system were the reactions at joints A and B, the gravity force and a torque exerted at B, and that the relative movement between bodies was frictionless - Figure 3.2. The static equilibrium equations for this mechanism were developed and compared with ADAMS results. The purpose here was to verify that the static numerical solutions for different mechanism configurations around all revolute joint B were close to the analytical solutions.
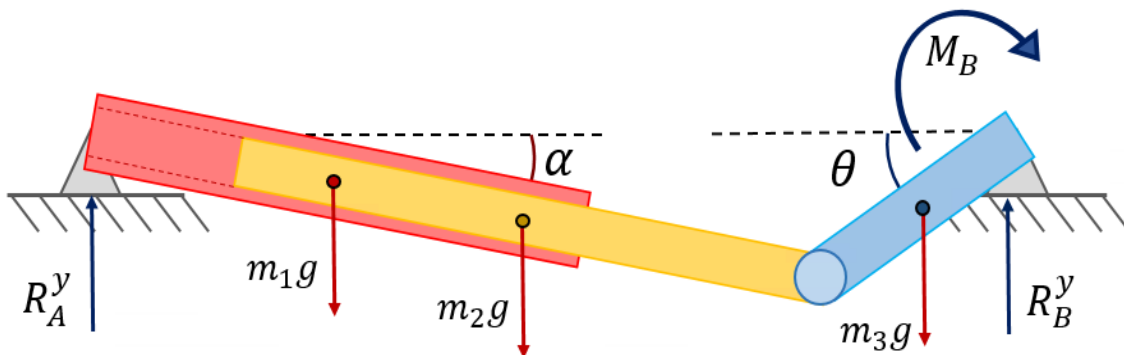
Figure 3.2 – Schematics of the studied system with the degrees of freedom and external forces

3.1.1.1 Static Analytic Analysis
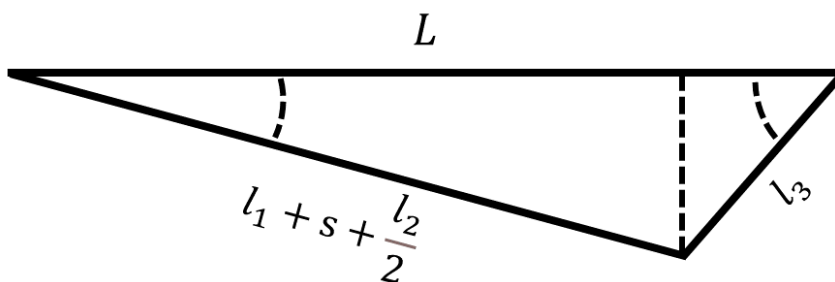
Figure 3.3 - Simple mechanism triangle scheme with dimensions

In this section, the development of the static equilibrium equations for the above-described system are presented. First, the equations that relate α to θ and s to θ were established. These equations were solely taken from the trigonometric relations of the triangles shown in Figure 3.3.

Through mathematical treatment of the trigonometric equalities on both cartesian directions, the following equations were obtained.

$$\alpha = \tan^{-1}(\frac{l_3 sin\theta}{L - l_3 cos\theta})$$

Equation 3.1

$$s = \frac{L - l_3 cos\theta}{cos\alpha} - l_1 - \frac{l_2}{2}$$

Equation 3.2

After having the geometric relations of the system variables established, it was possible to start developing the static equilibrium equations. Since this problem was considered as planar, there were only two force directions - x, y – and one torque direction – z – to formulate the equilibrium equations. At this point, it was important to define which were the variables of interest for this verification. Since the objective of the exercise was to validate the simulation results on ADAMS, comparing a higher number of variables would raise the verification quality. This way, it would be assured that the program did not only work as expected for certain parameters. In order to get the maximum number of relevant system variables, it was decided to separate the mechanism and analyze separately the free body diagram of each element.

Body 1 - Cylinder

To obtain the static equilibrium equations of the cylinder body, it was separated from the rest of the mechanism and its free body diagram was built – Figure 3.4. The sum of forces acting on the body were the joint reactions at A - R_A^x and R_A^y -, the gravity force at the center of gravity - $m_1 g$ -, and the forces transmitted from the second body - F_{21i} and F_{21o}. These transmission forces were divided in I inside and O outside forces, to reflect a situation where the only points of contact between the two bodies are at those two locations. This resulted in four unknown variables for the three formulated equations.
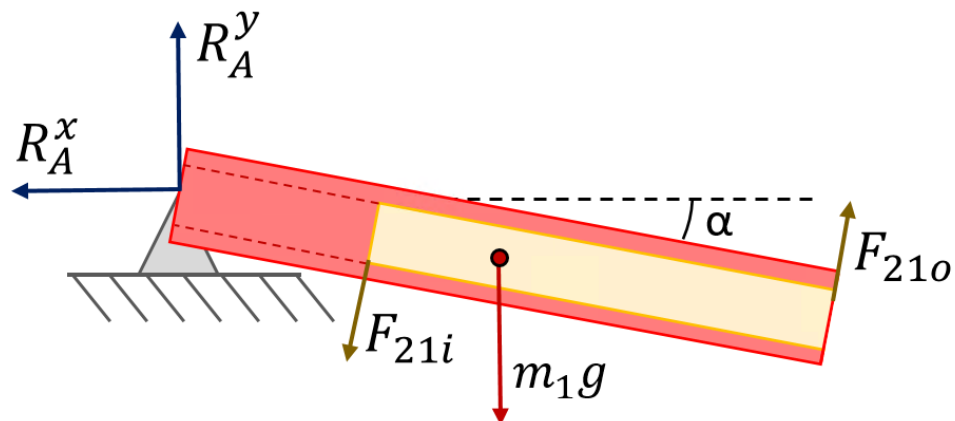
Figure 3.4 - Cylinder free body diagram

For this body, the following static equilibrium forces and torque equations are obtained.

$$\begin{cases} -R_A^x + F_{21o}sin\alpha - F_{21i}sin\alpha = 0 \\ R_A^y + F_{21o}cos\alpha - F_{21i}cos\alpha - m_1g = 0 \\ -\left(l_1 + s - \dfrac{l_2}{2}\right)F_{21i} + l_1F_{21o} - \dfrac{l_1}{2}m_1gcos\alpha = 0 \end{cases}$$

Body 2 - Slider

After the cylinder, the same formulation process was executed for the second body – Figure 3.5. The applied forces on the slider were the gravity - m_2g -, the reaction forces on C – or transmitted forces from the third body R_C^x and R_C^y -, and the reaction forces from the cylinder to the slider - F_{12i} and F_{12o}. Following the third Newton law these two latter forces have the same magnitude but opposing orientations of F_{21i} and F_{21o}, respectively.
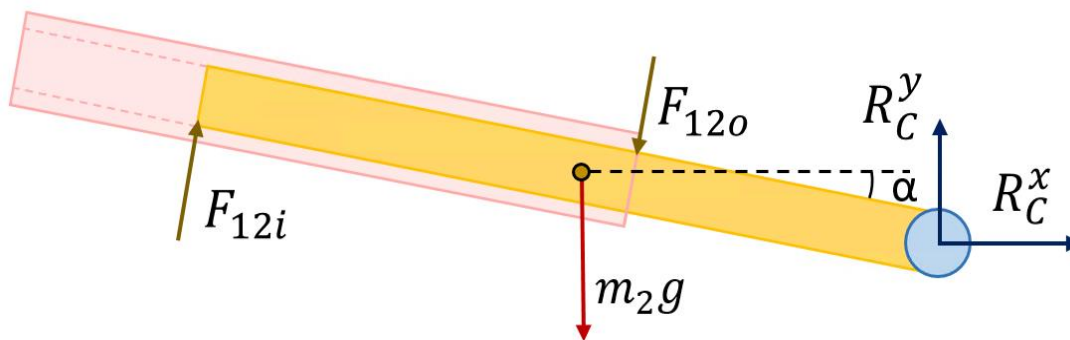
Figure 3.5 - Slider free body diagram

For this body were obtained the following static equilibrium forces and torque equations.

$$\begin{cases} R_C^x + F_{12i}sin\alpha - F_{12o}sin\alpha = 0 \\ R_C^y - m_2g + F_{12i}cos\alpha - F_{12o}cos\alpha = 0 \\ -l_2F_{12i} + \left(\dfrac{l_2}{2} + s\right)F_{12o} + m_2g\dfrac{l_2}{2}cos\alpha = 0 \end{cases}$$

The slider free body diagram introduces two more unknown variables – the reactions at C -, but also adds another three equations. With this, the number of unknown variables and equations was balanced, and it was possible to solve a system of equations to calculate the values of the forces involving the two bodies. Nevertheless, it was still intended to obtain the torque and reaction forces values at joint B.

Body 3 - Driver

Figure 3.6 shows a representation of the driver free body diagram. The applied forces are the gravity - m_3g -, the joint reactions at A - R_A^x and R_A^y -, and the transmitted forces from the second body - R_C^x and R_C^y.
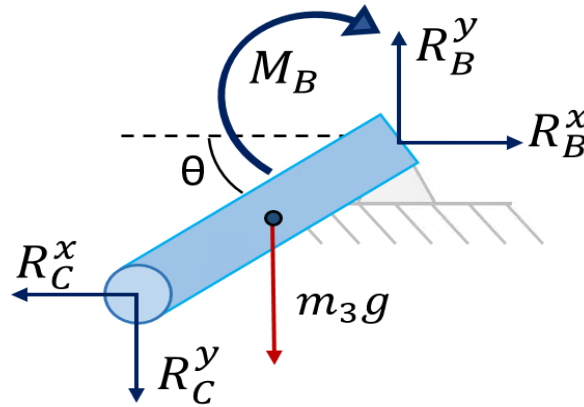
Figure 3.6 - Driver free body diagram

For this body the following static equilibrium forces and torque equations were formulated.

$$
\begin{cases}
-R_C^x + R_B^x = 0 \\
-R_C^y - m_3g + R_B^y = 0 \\
-M_B + \dfrac{l_3}{2}m_3g\cos\theta + l_3R_C^y\cos\theta - l_3R_C^x\sin\theta = 0
\end{cases}
$$

At this point, all nine equations to calculate the forces and torques involved in the static equilibrium of the multibody system were obtained. All equations are related to α, s and θ, and since the first two are themselves dependent on θ, this is the only input parameter to solve the matrix equation represented next.

$$
\begin{bmatrix}
-1 & 0 & -\sin\alpha & \sin\alpha & 0 & 0 & 0 & 0 & 0 \\
0 & 1 & -\cos\alpha & \cos\alpha & 0 & 0 & 0 & 0 & 0 \\
0 & 0 & -l_1 - s + \dfrac{l_2}{2} & l_1 & 0 & 0 & 0 & 0 & 0 \\
0 & 0 & \sin\alpha & -\sin\alpha & 1 & 0 & 0 & 0 & 0 \\
0 & 0 & \cos\alpha & -\cos\alpha & 0 & 1 & 0 & 0 & 0 \\
0 & 0 & -l_2 & \dfrac{l_2}{2} + s & 0 & 0 & 0 & 0 & 0 \\
0 & 0 & 0 & 0 & -1 & 0 & 1 & 0 & 0 \\
0 & 0 & 0 & 0 & 0 & -1 & 0 & 1 & 0 \\
0 & 0 & 0 & 0 & -l_3\sin\theta & l_3\cos\theta & 0 & 0 & -1
\end{bmatrix}
\begin{Bmatrix}
R_A^x \\
R_A^y \\
F_{21i} \\
F_{21o} \\
R_C^x \\
R_C^y \\
R_B^x \\
R_B^y \\
M_B
\end{Bmatrix}
=
\begin{Bmatrix}
0 \\
m_1g \\
\dfrac{l_1}{2}m_1g\cos\alpha \\
0 \\
m_2g \\
-m_2g\dfrac{l_2}{2}\cos\alpha \\
0 \\
m_3g \\
-\dfrac{l_3}{2}m_3g\cos\theta
\end{Bmatrix}
$$

This equation system was transposed to MS-Excel and with the use of the Excel Solver add-in tool, the values of forces and torques of the system were calculated for θ angles multiple of 15°. In Figure 3.7 are presented the values of the unknown variables for different displacement values of θ.
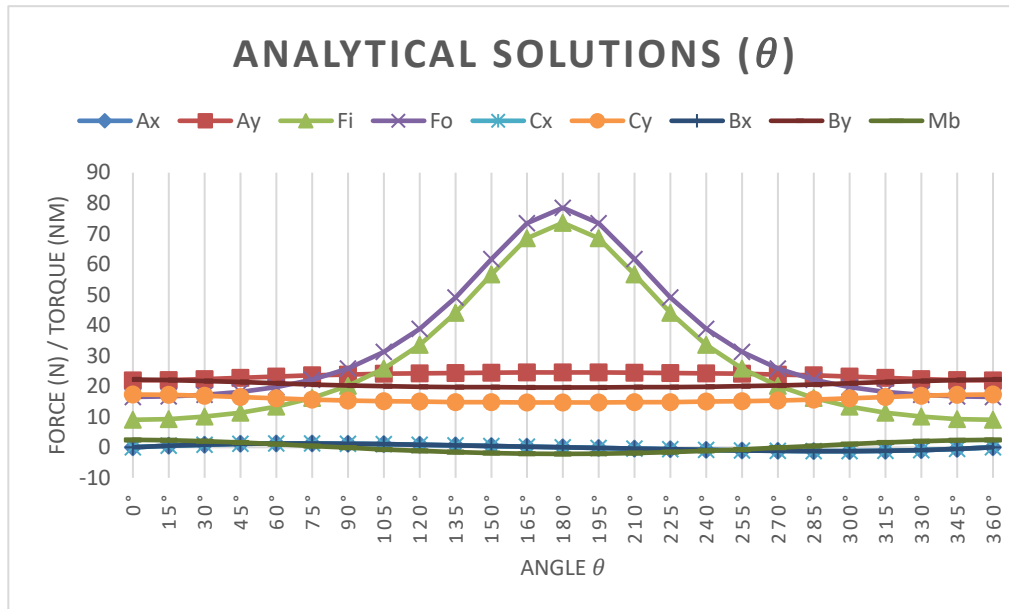
Figure 3.7 - Static analytic solutions

The values of R_A^x, R_B^x and R_C^x all have the same magnitude since they are the only force components along the x direction and they cancel each other - R_A^x cancels R_B^x and R_C^x is cancelled by the opposing reaction force in the third body. As expected, the values of F_{21i} and F_{21o} are the highest for the $\theta = 180°$ configuration, which is the configuration where the mechanism is fully extended. It makes sense that in this position the translational joint is under higher stresses to keep both bodies in line.

3.1.1.2 Adams Quasi-static Analysis

To model this system in ADAMS it was first necessary to create the three bodies and place them at their correct locations. The first body was created with a cylinder tool and the other two bodies were modeled as links. Then, the corresponding mass properties were attributed to each body. The through hole on the cylinder was made by subtracting its mass, but the simulation would run exactly the same whether there was this hole or not. For the numerical calculations only the location of the mass centers and the coordinates of the joints are taken into consideration. As long as no contact interaction had been defined between the two bodies, the cylinder hole would have no influence on the simulation results, since the cylinder center of mass suffers no displacement. Nevertheless, this hole was created to better portray the formulated mechanism.

Having the three parts modeled and properly positioned, it was then time to add the four joints connecting the bodies. Three revolute joints in A, B and C, and then a translational joint positioned in D – the center of mass of the second body. The purpose with this exercise was to

perform a so-called quasi-static analysis along the entire revolution range of the driver component. This quasi-static analysis evaluates the static equilibrium of the system at defined time steps throughout the movement (MSC Software Corporation 2021). To do so, a motion was created on revolute joint B to rotate the driver with a 30°/s angular velocity. At last, it was only necessary to apply the gravity force to all parts of the system. With all these steps executed, the virtual model represented the simple mechanism characteristics faithfully – Figure 3.8.
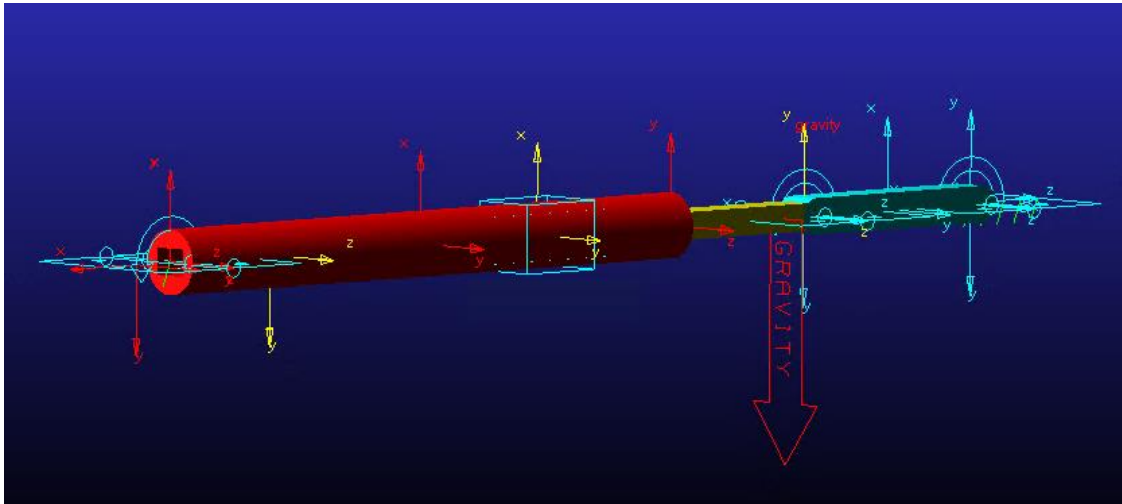
Figure 3.8 – Simple mechanism model generated in ADAMS

In the model's verification page the number of parts, constraints and the system degrees of freedom are reported. For this mechanism, the geometric number of degrees of freedom is one, but the Grübler formula in ADAMS showed a -3 value for the model. This resulted from the existence of three redundant constraints and the fact that the program considers the imposed motion as a constraint itself. By defining an intended motion for the system, it is not free to describe other movements. For this reason, the program also considers motions as constraints. Regarding the 3 redundant constraints, these were related to moment equations on the y and x directions, which do not concern this planar system. For this reason, these additional equations were left on the system. In case any problem during the simulation occurred, then it would be necessary to alter some of the joint types, for example the revolute joint at C for a spherical joint, to eleminate the redundant constraints. If that was done for all redudant constraints and the motion was also deactivated, then the Grübler formula would results in 1 degree of freedom.

Being the virtual mechanism fully modeled, it was necessary to create the appropriate measures which were going to be compared with the analytical solutions. The variables of interest are M_B - the necessary torque or moment at B to support the mechanism on that static configuration - and the reaction forces at A, B and C as another validation step. Therefore, a measure for each one of the seven mentioned elements: R_A^y, R_A^x, R_B^y, R_B^x, R_C^y, R_C^x and M_B was created. In terms of the translational joint, their measures would not be coincident with the values of F_{21i} and F_{21o}, because the kinematic constraint forces in the ADAMS model were not applied at the same location as the analytic equations. For this reason, it was decided to

analyze the normal force the translational joint has to sustain, and the reaction torque generated between the two bodies.

In order to better follows the values of the controlled degree of freedom, angle θ was also measured, as well as angle α and distance s, which were important to validade the geometric configuration of the system. Unfortunatelly, the measure of parameter s in ADAMS was obtained as the distance magnitude between the center of mass of the second body and the tip of the cylinder. That meant, the values presented were always positive, not corresponding to the definition that was previously made.

At this point, the multibody system was fully modeled and the output variables were chosen. The mathematical model was complete and ready to be simulated. The objective was to calculate the static equilibrium involved in the system to maintain its configuration in a series of defined θ angles around all the 360° of joint B. It was decided to take a static equilibrium evaluation every 15°, therefore the output time step was 0.5s, since the applied motion would rotate 30° per second. This also means that the duration of the simulation should be higher than 12s to cover the analysis around all angular displacement values from 0° to 360°.

A few first simulation tries were first performed to make sure the default simulation settings were appropriate. After it was decided that the error tolerances were small enough not to cause any disturbance in the values obtained, the final quasi-static analysis was performed. In Figure 3.9 it is possible to see the numerical results for some of the measured variables. All plots are referred to the angle θ since it is more straight-forward to understand which configuration the system is at, instead of using the simulation indepent variable – time.
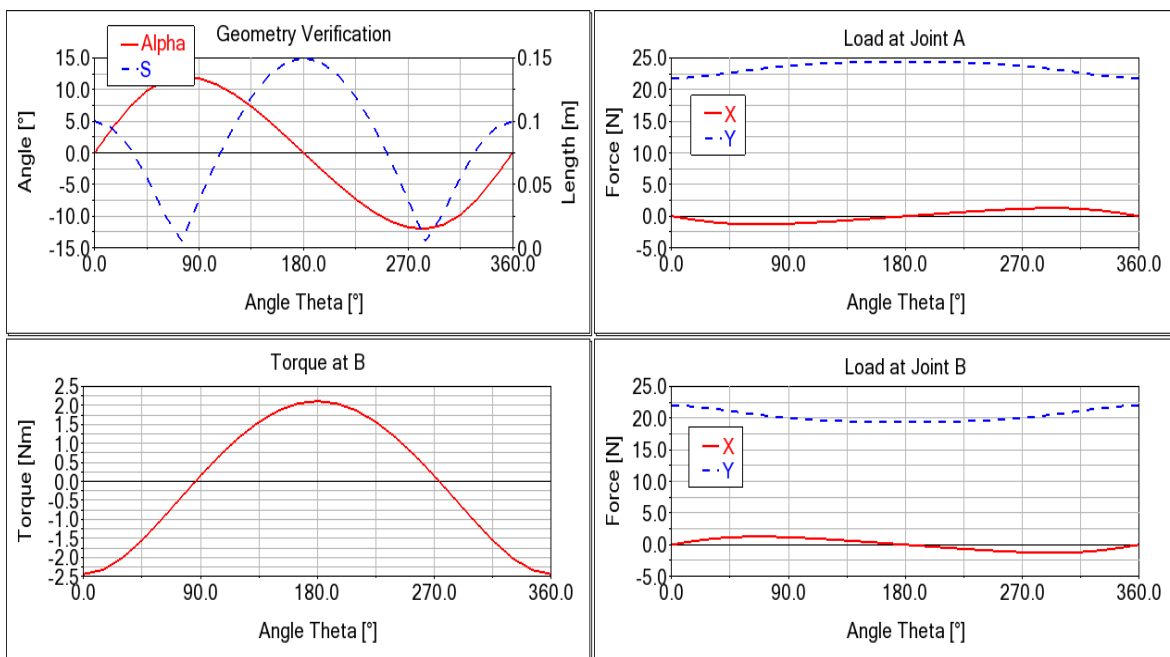
Figure 3.9 - Numerical results from ADAMS quasi-static simulation

3.1.1.3 Results Comparison

In this section are exposed the results obtained from the two motion analysis sources. From ADAMS were exported the data files with the output values depending on the θ angle. The

information in these files was then imported to an Excel file and the results obtained for each variable were compared.

First, it was important to confirm the geometric construction of the system was equal on both approaches. Otherwise, it would mean the multibody was not properly modeled or the geometric equations were incorrectly formulated. To verify the model construction, the s and α parameters were compared. The s imported values were modified to represent their correct orientation definition. To do this, the values between $\theta = 300°$ and $\theta = 60°$ were converted to their symmetric. In the following figures it is possible to observe the plot for each variable according to the method utilized.
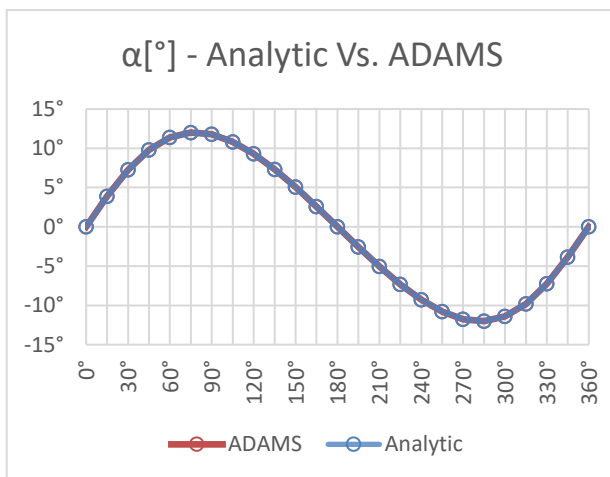
Figure 3.10 - Comparison of α between ADAMS and the analytical solutions
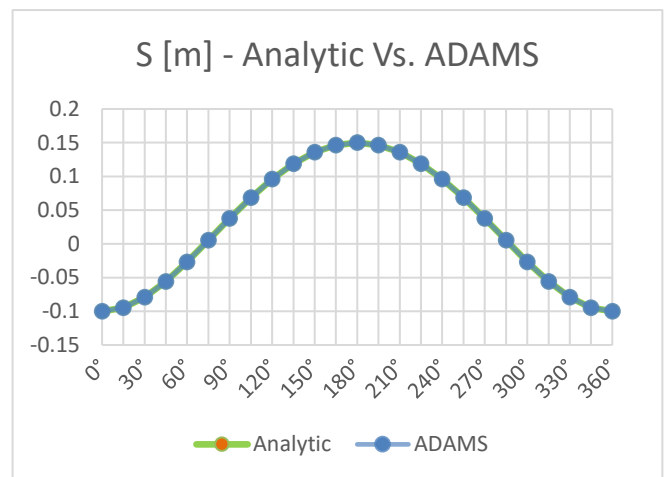
Figure 3.11 - Comparison of s between ADAMS and the analytical solutions

As those figures show, the values obtained from the two approaches for both variables are precisely the same. Even when comparing absolute errors, the results match entirely. The first significant digit of the error only appeared at the seventh decimal unit, caused by the truncation of the imported numerical results. This confirmed that the geometry of the chosen system has the correct dimensions on both methods.

In Figure 3.12 are exposed the values of the reaction forces at the revolute joints A. Once again, the differences between the obtained results are practically neglectable. As was mentioned before, the values for the x reaction forces at joint A are symmetric, but the error between the magnitude values of both calculations is again very close to zero – seventh decimal unit of the Newton.
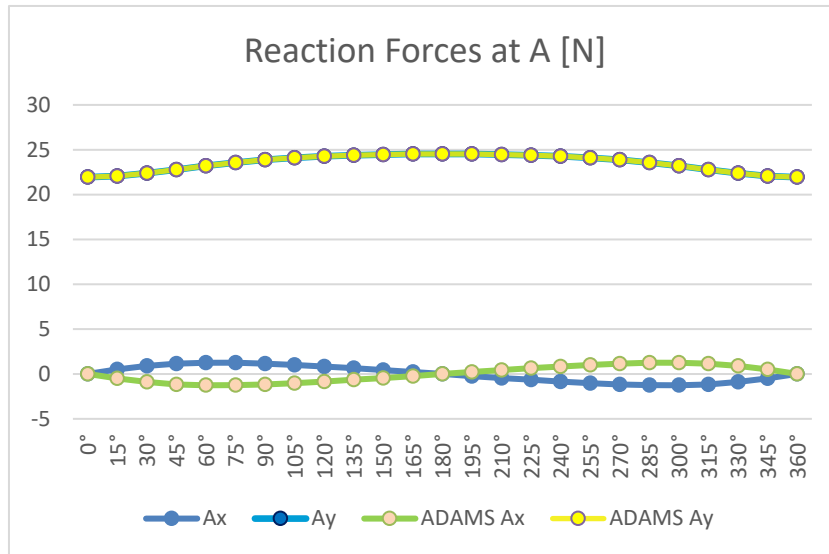
Figure 3.12 - Comparison of the reaction forces at A between ADAMS and the analytic solution

Some of the forces or torque variables present a symmetric value in comparison with the values obtained for the same unknowns through the analytic equations, because they have opposed directions in the different models. That is for example the above case of R_A^x which is defined in the x positive direction in the virtual model and was oriented on the x negative in the analytical free body diagram - Figure 3.12.

The torque values required at revolute joint B to sustain the mechanism at the desired position are exposed in the next figure for both methods. As it can be seen, the plot curves for both results are coincident.
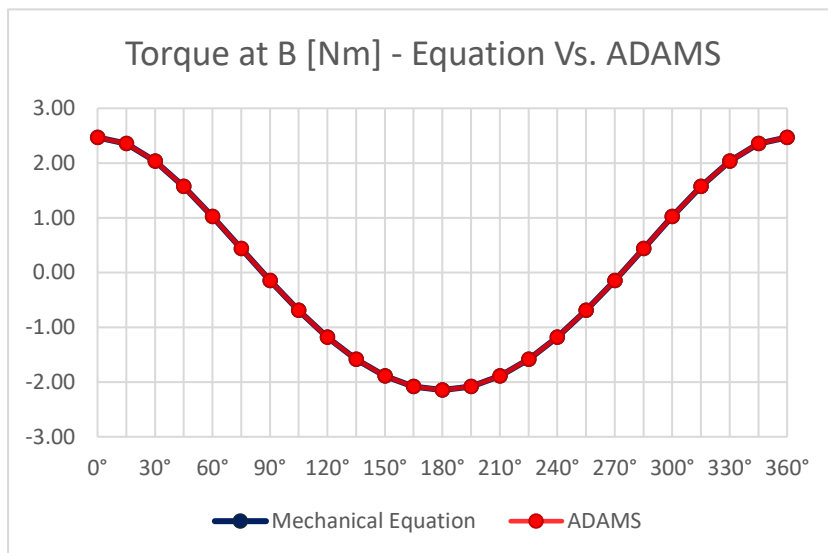
Figure 3.13 - Comparison between numerical and analytical solution on Torque at B

For the rest of the force and torque variables the results are practically the same between ADAMS analysis and the analytical formulation. The only exception is obviously for the translational joint reaction forces. In this case, the F_{21i} and F_{21o} pair was converted to an

equivalent force and torque reactions at the center of mass of the second body. Later the values of those equivalent reactions were compared with the measures at joint D in ADAMS, and it was observed that the results were also matching.

3.1.2 Dynamic Verification

Even after validating the numerical results for the static problem, it was still convenient to prove the reliability of ADAMS when inertia and accelerations are taken into consideration. The equations of motion are much more complex than the static case since they involve the inertia component of the bodies – which in turn comprises the rate change of angular moments and accelerations. To validate the numerical results obtained in ADAMS for a dynamic problem, the same simple mechanism was utilized. First, one analytically method was employed to derive the equations of motion of the system, and then the mathematical model was simulated in the computer program.

The selected method to analytically obtain the equations of motion for this mechanism was the D'Alembert principle of dynamic equilibrium. Since this method also relies on the free body diagrams of each element, and that task had already been done for the static case, there was no need to formulate new coordinates or variables. Additionally, the equations of motion were also partially obtained. It was only necessary to formulate the expressions for the absolute acceleration and the rate change of angular momentum for each body.

Regardless of having already part of the work done, it was still necessary to relate the velocity and acceleration expressions for α and s in relation to θ. That could be obtained by deriving Equation 3.1 and Equation 3.2 – from the trigonometric relations of the system's triangle – in respect to time. Doing so for both equations led to the following expressions,

$$\dot{\alpha} = \frac{l_3\dot{\theta}(cos\theta(L - l_3cos\theta) + l_3sin^2\theta)}{(l_3sin\theta)^2 + (L - l_3cos\theta)^2}$$

$$\dot{s} = \frac{l_3\dot{\theta}sin\theta cos\alpha + \dot{\alpha}sin\alpha(L - l_3cos\theta)}{cos^2\alpha}$$

Deriving once again these equations led to the acceleration of α and s. However, those expressions will not be here exposed due to their unfitting size. In reality, after the functions had been derived, Symbolab Math Solver was utilized to confirm the derivatives had been correctly obtained, due to their extensive size. Once the velocity and acceleration of those parameters were described in relation to $\theta, \dot{\theta}$ and $\ddot{\theta}$ it was then possible to start analyzing the dynamic equilibrium of each component.

Body 1 - Cylinder

Let us start with the dynamic equilibrium of the cylinder body. Its absolute acceleration at the center of mass $\ddot{x}_1$ can be taken by deriving the position vector $\overrightarrow{AG_1}$ - expressed on the global reference frame – twice in respect to time. That results in the following expression,

$$\ddot{x}_1 = \frac{l_1}{2} \begin{Bmatrix} -\ddot{\alpha}sin\alpha - \dot{\alpha}^2 cos\alpha \\ -\ddot{\alpha}cos\alpha + \dot{\alpha}^2 sin\alpha \\ 0 \end{Bmatrix}$$

For the dynamic equilibrium of moments, the rate change of angular momentum $\dot{H}$ must be obtained. This value has to be referred to the point where the moment equilibrium was previously calculated. Through the König's theorem the rate change of angular momentum can be expressed in relation to point A by the following expression,

$$\dot{H}_A^1 = (I_{zz}^1 - m_1 \frac{l_1^2}{4})\ddot{\alpha}$$

With this, the dynamic equilibrium equations can be formulated for the first body.

$$\begin{cases} -R_A^x + F_{21o}sin\alpha - F_{21i}sin\alpha = m_1 \frac{l_1}{2}(-\ddot{\alpha}sin\alpha - \dot{\alpha}^2 cos\alpha) \\ R_A^y + F_{21o}cos\alpha - F_{21i}cos\alpha - m_1 g = m_1 \frac{l_1}{2}(-\ddot{\alpha}cos\alpha + \dot{\alpha}^2 sin\alpha) \\ -\left(l_1 + s - \frac{l_2}{2}\right)F_{21i} + l_1 F_{21o} - \frac{l_1}{2}m_1 g cos\alpha = (I_{zz}^1 - m_1 \frac{l_1^2}{4})\ddot{\alpha} \end{cases}$$

Body 2 – Slider

Going on now to the second body, its absolute acceleration $\ddot{x}_2$ was calculated from position vector $\overrightarrow{BG_2}$ instead of utilizing $\overrightarrow{AG_2}$ in order to eliminate the s velocity and acceleration from the problem. This was done to simplify the expressions for $\ddot{x}_2$, having to work with only the θ and α variables. By deriving the above-mentioned vector, the following acceleration vector is generated,

$$\ddot{x}_2 = \begin{Bmatrix} \ddot{\theta}l_3 sin\theta + \dot{\theta}^2 l_3 cos\theta + \ddot{\alpha}\frac{l_2}{2}sin\alpha + \dot{\alpha}^2 \frac{l_2}{2}cos\alpha \\ -\ddot{\theta}l_3 cos\theta + \dot{\theta}^2 l_3 sin\theta + \ddot{\alpha}\frac{l_2}{2}cos\alpha - \dot{\alpha}^2 \frac{l_2}{2}sin\alpha \\ 0 \end{Bmatrix}$$

As was done for the first body case, the rate change of angular momentum $\dot{H}$ must be obtained with respect to the point utilized for the static equilibrium of moments. For the slider body case, the chosen point was C and therefore, the following expression can be derived,

$$\dot{H}_C^2 = \left(I_{zz}^2 - m_2 \frac{l_2^2}{4}\right)\ddot{\alpha} + m_2 \frac{l_2}{2}l_3\left[\ddot{\theta}(cos\theta cos\alpha - sin\theta sin\alpha) - \dot{\theta}^2(sin\theta cos\alpha - cos\theta sin\alpha)\right]$$

Now, it is just a matter of introducing these 3 expressions on the equations above obtained for the static situation of the slider body.

Body 3 - Driver

Lastly, the global acceleration and rate of change of angular momentum of the third body are shown. They are very similar to the first body expression, as both elements rotate through a revolute joint around a specific point. Applying the same principles for this case, results in the following expressions,

$$\ddot{x}_3 = \frac{l_3}{2} \begin{Bmatrix} \ddot{\theta}sin\theta + \dot{\theta}^2cos\theta \\ -\ddot{\theta}cos\theta + \dot{\theta}^2sin\theta \\ 0 \end{Bmatrix}$$

$$\dot{H}_B^2 = \left(I_{zz}^3 - m_3 \frac{l_3{}^2}{4} \right)\ddot{\theta}$$

Now that all inertia forces' components have been obtained, the system of 9 equations of motion can be written and solved for any type of movement of this simple mechanism. This system of equations will not be here exposed, due to its unreasonable size. The only variables that need to be previously defined are the components of the system state vector: θ, $\dot{\theta}$, and $\ddot{\theta}$. After characterizing the mechanism state at a certain time instant, this equation matrix can be generated depending exclusively on those three parameters. Hence, it is possible to obtain the forces involved in the system for all states of a same system.

3.1.2.1 Results Comparison

As was done for the static verification, the mechanism was analyzed in ADAMS and the measures values throughout the motion were later exported. The type of simulation chosen was the kinematic type because this is the most appropriate option for systems with zero degrees of freedom. As for the quasi-static case, the mechanism was driven by a defined motion at the revolution joint C, thus constraining its only degree of freedom. Even if the simulation is called kinematic, ADAMS also calculates the forces and reactions developing in the system. Basically, an inverse dynamic analysis can be performed by selecting the kinematic simulation in this program. In cases where there are degrees of freedom and at least one body is free to react under external action, then a dynamic simulation must be utilized.

To compare the numerical results with the analytic method used for a dynamic problem, three different motions were utilized. Two with positive acceleration 90°/s² and 30°/s² and another accelerating in the opposing direction -60°/s². Also, the initial conditions – angular velocity and starting angle – were made different for the three motions. The objective was to compare the two analysis methods for a wider variety of movement states. Instead of analyzing the entire motions and comparing the results at each time step, only six motion states in total were taken from the numerical results. Unlike the static case, this decision was made to reduce the workload in updating and solving the system of equations at every time step. Therefore, the time steps chosen were taken specifically at mechanism states as diverse as possible.

$$q_1 = \begin{Bmatrix} 11,25° \\ 45°/s \\ 90°/s^2 \end{Bmatrix} \qquad q_2 = \begin{Bmatrix} -150,4° \\ -51°/s \\ 30°/s^2 \end{Bmatrix} \qquad q_3 = \begin{Bmatrix} 180° \\ 180°/s \\ 90°/s^2 \end{Bmatrix}$$

$$q_4 = \begin{Bmatrix} -52,5° \\ 30°/s \\ -60°/s^2 \end{Bmatrix} \qquad q_5 = \begin{Bmatrix} -45° \\ 0°/s \\ -60°/s^2 \end{Bmatrix} \qquad q_4 = \begin{Bmatrix} -59,7° \\ -42°/s \\ -60°/s^2 \end{Bmatrix}$$

The above-shown vector states portray the different movement characteristics for the six solutions. There are states where the angular velocities and accelerations have opposed orientations and the mechanism positions are spread through the angles range. After extracting the output values for the corresponding time steps of these 6 samples and solving the analytical equation matrix for the same mechanism states, the relative error between the two methods was calculated for each variable. From Figure 3.14 it can be seen that the relative error values are all contained within 0,5%. In fact, except for the first and fifth vector state the deviations between the two methods could almost be neglected. Although were compared only six in all infinite possible movement states, the differences in the solutions from the two methods may not vary profoundly. This confirms that the results obtained from ADAMS are close to the analytic model. Therefore, the reliability of this numerical program in respect to a practical case, only depends on how close the characteristics of the motion model are to the real system.
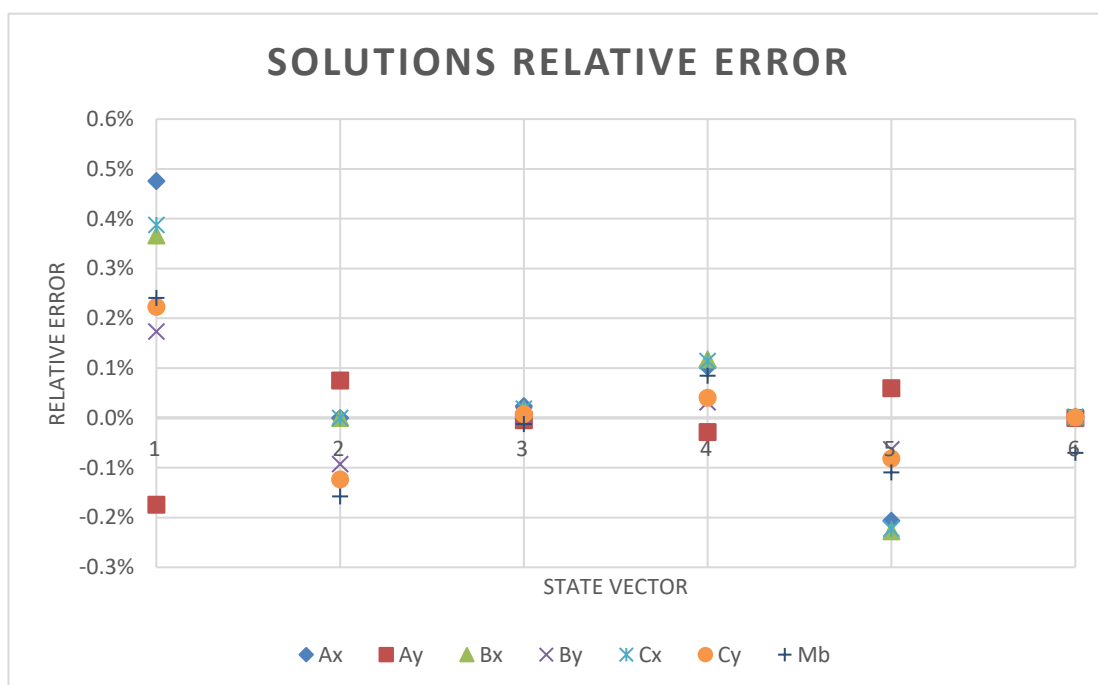
Figure 3.14 - Relative error of the dynamic solutions between the analytic and numerical methods

After performing both verification processes, it was considered safe to rely on the motion analysis program to perform static and inverse dynamic simulations of multibody systems. The analytic formulation of the equations for both problems with this simple mechanism required already a decent amount of time, while in ADAMS the modeling of the system was much faster. With a more complex mechanism, the task of obtaining the system of equations that represent it would become too overwhelming. In the software program the most time-consuming step is the modeling process. The analyses were very quick – around a few seconds – which allows the user to change and experiment parameters of the mechanism or simulation settings. This freedom of testing virtual properties, interacting with the system, and playing around different values is extremely advantageous. It gives a much better understanding of the overall mechanism behavior. In addition, it is also possible to run the animations and visualize the movement of the bodies. In summary, MSC ADAMS is an interactive multibody simulation software with quick analyses and reliable results.

For these reasons, it was decided to use this computer tool to execute the motion analyses with an industrial robot model to obtain the motion that generates the highest load on a construction supporting the machine.

3.2 COMAU NJ290 3.0

The purpose of this academic work is to develop a modular structure that can couple and supply the media, electrical and information needs for the operation of the WSK kinematic unit. Before starting the design project of the structure, it was first necessary to know the load that such a construction must endure. The characterization of this load is an important step. The structure must not by any means fail under operation. The issue here was that there was no prediction on future usages for the WSK production systems. Since the main objective of this investigation project is to offer a versatile manufacturing solution – adaptable to different production task – and since the kinematic unit itself was not yet conceived, there was no background knowledge on the mechanical load that such a base structure might have to endure.

To solve that, it was decided to take on the worst-case scenario approach and obtain the system movement that exerted the highest load on the supporting base. By obtaining the single movement that put the greatest amount of stress on the structure and dimensioning the construction to withstand those loads, it would be assured that the support would never fail under operation. To achieve this critical movement, a thoroughly motion analysis was performed with a virtual industrial robot model. This model was based on the industrial robot COMAU NJ290-3.0 and was utilized to study the load exerted from this machine to its ground connection when performing different movements. The physical characteristics of this articulated-arm robot were utilized for the multibody model, because the wbk researchers were at the time planning on using this machine to test the physical functionalities of the WSK project.
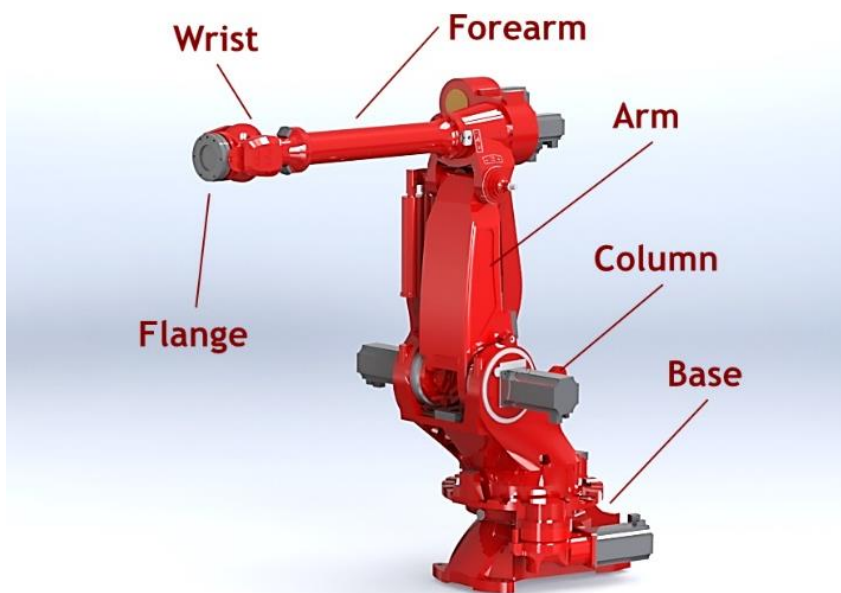
Figure 3.15 - COMAU NJ290-3.0 industrial robot

COMAU NJ290-3.0 is a six axes robot arm designed to be used in industrial environments – Figure 3.15. It possesses a high load carrying capacity and is intended for applications that require defined movements paths. The industrial robot movement is controlled by six AC

brushless servomotors. Each servomotor is responsible for the motion of one of the axes. Alongside the robot arm – between the second and third axes – there is a spring system used to balance the static load on the second axis. Some of its industrial usages are spot welding, component handling or process machining. It can hold a maximum 290kg of payload at the wrist plus 50kg of additional load on the forearm. The total weight of the machine is 2150kg and it is designed to be mounted on the floor.

Through the following sections of this text, the motion analysis executed with the COMAU multibody model in ADAMS is presented. The elaboration of the mathematical model is first broached, due to its importance in crucial assumptions that were made and other relevant details of the robot characterization. Later, the simulation methodology to obtain the highest load movement is exposed in detail. The purpose of the following sections – besides documenting the work done - is to offer the reader a plausible approach to use in similar situations when it is intended to discover such critical scenarios. Lastly, the numerical results are presented and analyzed along with other relevant remarks.

3.3 Industrial Robot Virtual Modeling

3.3.1 CAD Assembly File

To start building the robotic mechanism in ADAMS, a CAD assembly file of the COMAU NJ290 – downloaded from the company's website - was imported into the multibody simulation program. This file is composed of 21 components: 15 different parts representing structural components of the machine plus the 6 electric servomotors.

At this point, it is important to mention some aspects regarding the CAD assembly file. The first is that it only represents the exterior dimensions of the components' geometry. With it an interested future buyer can obtain a general idea on the machine's topology – how much space it occupies, which motion do the axes need to perform to reach a certain configuration, and other geometric relations between different parts. Although the assembly files are a good representation of the machine's geometry, they do not carry information regarding what runs "inside" the robot. Most of the robot CAD parts are completely blank. When a sectional view is cut through a part's geometry, it shows no internal elements. Most of the parts are modeled as bulk solids - totally filled with mass. This cannot possibly be true for some physical components because there must be other internal elements located inside some of the large components' geometry. That is the case for bearings, cylinders, gear systems, electric cables and so on. The electric motors on the CAD file are a good example. If one of them is cut by a sectional view, it is completely blank, instead of showing many different elements inside its outer frame. In the next figure a sectional view of the forearm and the electric motors depicts this situation.
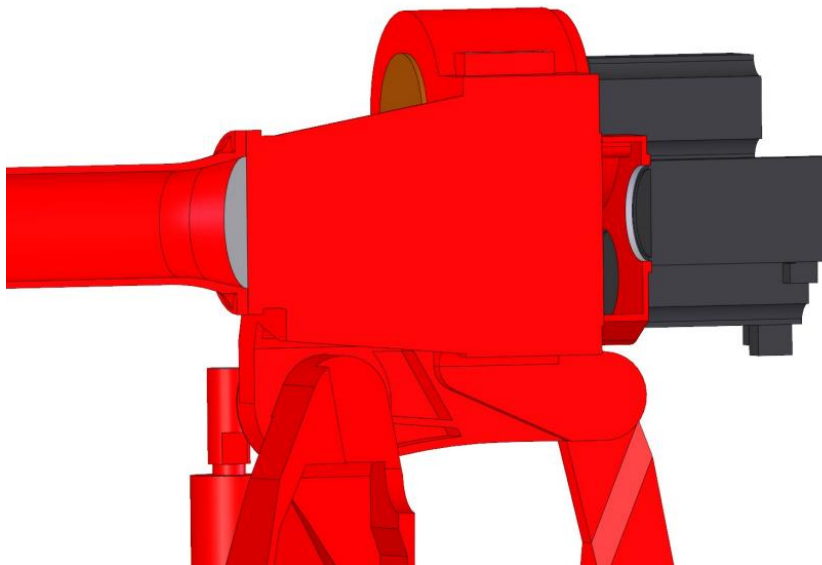
Figure 3.16 - Sectional view of forearm and electric motors of the CAD file

Another concerning aspect of the CAD files is the conflict of values on the components' mass properties. Although the assembly file has already defined the density for each component, those values do not match the robot description. For start, there are only two different density values for all the parts of the system: $7850 kg/m^3$ or $1000 kg/m^3$. Most of the structural parts have the former density value, while the electric motors and a few other structural components have the latter. It can be speculated that the $1000 kg/m^3$ density value

is used to balance the weight of some components. As their virtual design is totally filled with material, the lower density could be used to approximate their mass to the real value, because in reality these components might be hollow. However, the total resulting mass of the CAD assembly is 3137,25kg – almost 46% more than the announced value of 2150kg. This means, that the structural components of the virtual system are much heavier than their physical counterparts. Their density value is too high for the bulk geometry that they possess.

Two of the most important aspects when preparing a virtual model for a multibody system simulation are the correct positioning of each part's center of mass and its mass properties. The geometry of a component will influence its center of gravity location and its moments of inertia, while its attributed density or defined mass will influence the body's mass value. When a body is modeled as totally filled, while in reality it is not, deviations between the virtual and the physical mechanisms are introduced. This is even worsened when some of the parts not modeled have internal movement inside the structural components.

Obviously, the objective with a computer engineering simulation is to have a mathematical model with the closest characteristic to the real situation. Each deviation will introduce more errors on the results obtained, reducing the reliability of the simulation. For this reason, it was decided to alter the density values of components. Unfortunately, no information was found regarding possible valid assumptions or worthy comparisons with other robots' characteristics. That meant, there was no supporting data to base the mass properties' decisions. With no reliable information, the following decision path was chosen.

3.3.1.1 Alterations to the Robot Mass Characteristics

The first objective was to assure that the total robot weight equaled 2150kg. Since there was no base knowledge on the weight of the structural elements of the system, it was decided to first obtain the electric motors' masses. With that information, the total weight of the structural components would be known. Then, some components were selected to have their density altered. This selection was based on the geometric detail and reliability of each part on the CAD file. For instance, a body that had an electric motor coupled to it without internal features – like holes for that motor shaft - would be selected to have its density changed. All the components that were not selected remained with the 7850kg/m^3, while the others had a new density attributed so that the total weight of the robot was equal to 2150kg.

Table 3.1 – LAFERT electric motors characteristics and weight range

MOTOR CODE	STALL TORQUE	NOMINAL TORQUE	STALL CURRENT	WEIGHT RANGE	WEIGHT AVG
B10.33I	33Nm	23Nm	22,3A	46,8 – 59 kg	53,4kg
B71.13Q	13Nm	9Nm	12,1A	11,1 – 20 kg	16,0kg

There are only two different models of electric motors used in the NJ290-3.0 robot – one model for the first 3 axes and another for the other 3. Through the name of these two motors on the COMAU assembly file, it was possible to find their characteristics on the electric motor supplier website. Unfortunately, the mass of the electric machines was not included in the properties displayed. Therefore, catalogues from other companies selling similar electrical machines were explored to obtain an idea of the usual weights. Table 3.1 shows some of the characteristics of the two motors and the weight interval and weight average obtained from the market survey.

The selected values for the robot motors' weight were the average weights. This resulted in 208,2kg for the six electric motors in the robot system. Then, the structural components that would have their densities modified were selected. These are the components in light blue shown in the following figure. To obtain a final weight equal to the technical specifications' value the density of these elements was set at $3605,4kg/m^3$.
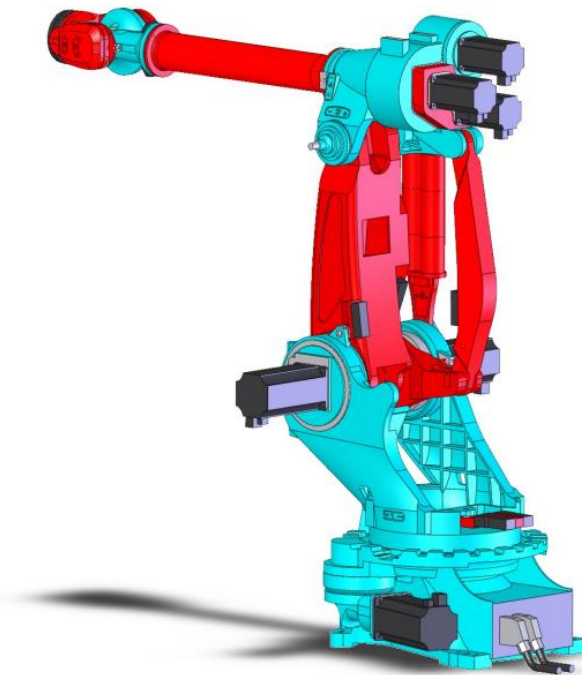
Figure 3.17 - Blue structural components of the COMAU robot had their densities altered

In that way, it was assured that the total weight of the virtual robot met the technical specifications presented by COMAU. Although certainly closer to the physical machine than the initial mass properties, there was no way possible to evaluate the accuracy of these decisions. The only information available at the time was the CAD assembly file. Unfortunately, due to the lack of better options the construction of the virtual model was done with these mass characteristics.

3.3.2   ADAMS/VIEW

Having defined mass properties for the different components, the CAD assembly file was then imported to ADAMS/View – Figure 3.18. The selected unit system of work was the meter/kilogram/second. First it was checked if the components were correctly imported and if the mass of each body was the same. No elements were missing, and their positioning was exactly the same as in the assembly CAD file. In addition, also the reference coordinate system was imported, becoming the global frame in the multibody program. This coordinate system had the y-axis along the height of the machine, while the xz-plane contained the bottom surface of the robot.

Now with the elements' geometries properly imported, it was time to create the connections between bodies. The fixed joints – 0 DOF - were the first to be created. This joint type locks two elements together, preventing any relative movement between them. It works as a unite tool that converts two parts into one, but with the advantage that this joint can later be eliminated, and the two parts' properties are maintained separate. If the unite tool was used, it would be later impossible to reverse that operation. However, the Unite tool reduces the number of equations to solve, while Fixed joints do not.
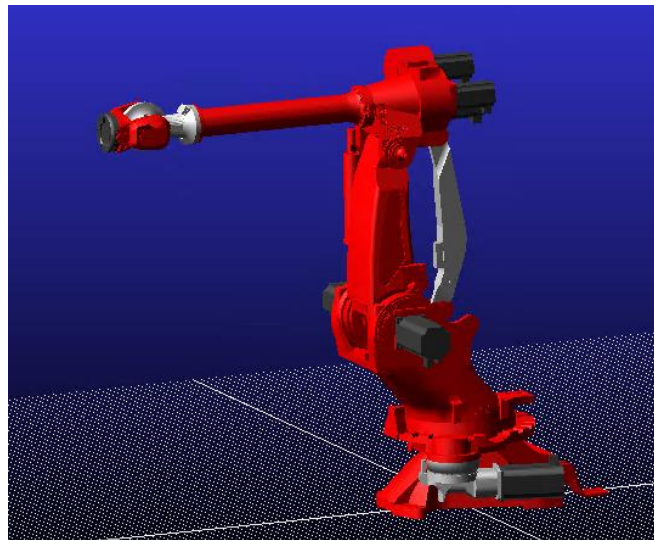
Figure 3.18 - COMAU CAD files imported into ADAMS/View

This joint was applied to all parts that are at rest with its adjacent body. A clear example is the case of the electric motors that are coupled to another component and therefore have a constant position relative to that part. Although its relatively simple function, this whole dynamic study to obtain the critical movement of this model was done focused on one specific fixed joint. The joint that locks the Base of the robot to the Ground - Figure 3.19. This is the joint that maintains the system fixed to the ground or environment. It represents the coupling of the robot to its supporting structure. The purpose of this study was to obtain the reaction forces this joint has to sustain to hold all the structure in place while it is under movement.

The chosen location for this joint was the origin of the global frame, which is in fact outside the robot geometry as it can be seen in Figure 3.19. This is not a problem since the program solver calculated the joint kinematic reaction forces at that location, and then those forces were later utilized on another CAE program for the dimensioning of the structure. As the robot

Base has four feet that are laid on top of the structure, the load will have to be later distributed across these four sections.
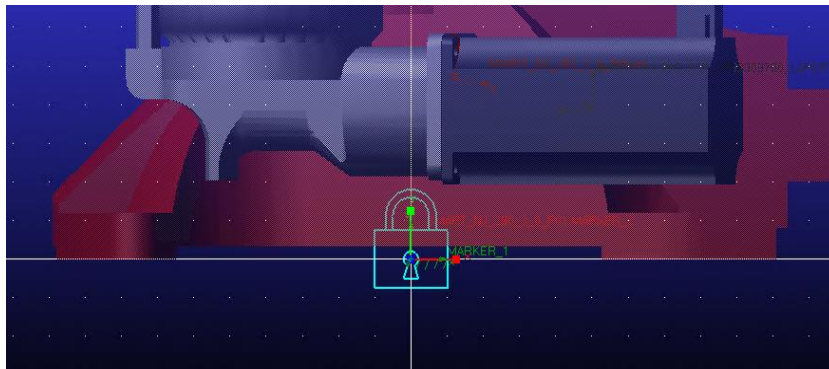
Figure 3.19 - Position of the fixed joint

With all fixed joints created, the revolute joints – 1 DOF - of the system were established. These joints allow the relative rotation of two bodies along a defined axis and therefore were applied at the six axes of the robot and at other bodies that require such a movement between them. For all revolute joints, their point of application was chosen at the mid-section of the respective rotation axis. This helps to later divide the reaction forces if it is intended to analyze the load at the bearings. It also means that some revolute joints will be placed outside any of the bodies they are referring to, which is the case for the second axis of the robot.

Since there is relative movement between bodies, it was thought to also include friction characteristics to approximate the model as much as possible to the physical behavior. The friction resistance is mainly dependent on the reaction forces at the joints and is actuated on the motion direction. This means, friction will mostly impact the torque necessary at each axis to describe the desired rotation. Since the objective of this study was focused on the forces transmitted to the base structure, the influence of friction between bodies was not significant. To prove this, a simulation with friction at the joints was later performed with different coefficient values and it was observed that the reaction forces at the base joint were practically unaltered. Thus, the joints in this model were considered frictionless.

Going forward with the model construction, it was then necessary to define the only translational joint – 1 DOF – of the system. This joint was defined to be located between the two bodies of the balancing spring that stabilize the second axis load. With this, the two parts that compose the spring system of the robot could slide on one another. This spring raised another concern, namely the spring stiffness value. There was no data available on this subject, making it impossible to attribute a spring force between the two bodies. Nevertheless, because this was an internal force of the system, it would have no impact on the base joint load. To confirm this, the system was simulated with different stiffness values for a spring modeled between the two components. The results of those simulations revealed that the fixed joint reaction forces did not change with the spring's stiffness. In fact, only the reactions at the second and third axis did vary. Due to its irrelevance for this dynamic study, this internal force was not modeled. Yet it is important to mention, if another system parameter is to be studied with this robot model, it might be necessary to create and characterize this spring force, as well as the friction coefficients between parts.

Lastly, two Point Masses were generated. These would represent the 290kg and 50kg maximum payloads at the wrist and forearm, respectively. These elements are points that have mass, but no inertia properties (MSC Software Corporation 2021). The locations of these two masses were chosen at the farthest point possible from their application body. The 290kg Point Mass was fixed to the Flange body and the 50kg to the Forearm. Figure 3.20 shows the mentioned points for both payloads.
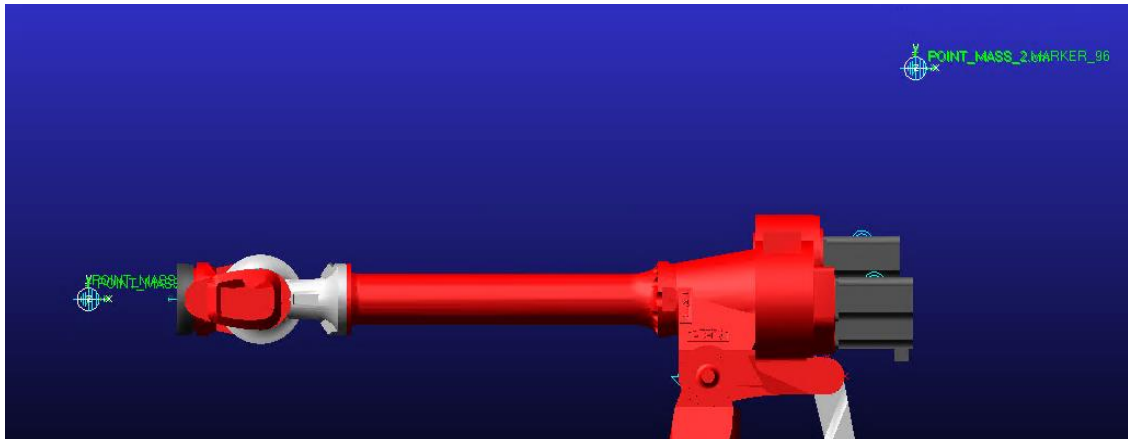
Figure 3.20 - Position of the two Point Masses representing the maximum payloads

At this point the multibody system had all necessary bodies and their interconnections. In the model's verification page, the calculated number of Degrees of Freedom was 6, but the Grübler formula had resulted in 0. This meant, there were six additonal redundant constraints. All these constraints were related with the closed-chain trapezoid of the robot and the spring system between the second and third axes. Through some manipulation of the joint types – for example, modifying some revolute joints to spherical and others to cylindrical– it was possible to reach a mechanism with 6 DOF and 0 redundant constraints. All elements of the multibody system were then succesuflly connected.

The virtual mechanism was fully generated. Its characteristics were – with the information available - the closest possible to the physical robot. The only external force acting on the system was the gravity. Therefore, the multibody model was ready to be analyzed.

3.4 Base Joint Load Analysis

In this section, the reasons behind the sequence of simulations that were performed with the COMAU NJ290 virtual model are exposed. The sole purpose of this whole robot motion study was to achieve the single critical movement that at one instant generates the highest load on the Fixed Joint supporting the mechanism at the Base. Since it is impractical to simulate every possible random robot motion to obtain for certain the critical movement, a structured methodology was implemented. This approach relies in a series of simulations which can be divided in the following groups of analyses:

- Quasi-static analyses around the robot working space limit.
- Inverse dynamic analyses for each individual axis.
- Parameterization analyses combining the axes' motions.

The first group of simulations had the objective to obtain the robot static configuration – or pose - that generates the highest load on the base. It was decided to find this configuration first, considering that it would be a good approximation for the region of the critical dynamic motion. The quasi-static simulation was only performed around the robot working space envelop, because it was assumed the highest static load would be exerted when the robot arm was totally extended. This was considered as a reasonable assumption, since the gravity was the only external force acting on the system. An extended robot arm would push the center of mass of the whole system further away from the base. With this group of analyses the static configuration that generated the highest load at the robot support was found.

The second simulation group was performed to gather a better understanding on the influence each different axis' motion had on the load sustained by the base joint. The purpose here was to control the motion of each axis and - through inverse dynamic simulations - compare the differences it caused on the robot bottom stresses. In order to have a more methodic approach, the following three different movement types were analyzed for every axis:

- Maximum angular velocity around all range of motion – Case 1
- Acceleration from rest to maximum angular velocity – Case 2
- Deceleration (braking) from maximum angular velocity to rest – Case 3

Each one of these movement types was analyzed for both angular orientations – clock- and counterclockwise. By performing these types of movements on every axis and on both rotation orientations, all possible critical motions for that revolute joint were covered. This would allow a comparison between the different motions to select the one that had a higher impact on the load. While each axis' motion was being evaluated, all other axes were locked at their critical static position. At the end of this series of simulations, it was known which was the critical movement type for each axis and its influence on the forces and moments transmitted to the ground.

Lastly, a series of parametric analyses was performed utilizing the knowledge previously gathered. At this point, it was known which was the critical movement type for each axis. In order to obtain the critical motion for the entire system, it was assumed that motion would be a combination of the critical ones of each axis. The purpose of these parametric analyses was then to test different movement combinations, in order to find the mechanism critical movement. To do so, variables that influence the way different axes' motions can be combined

were studied. These studied variables can be divided in two groups: space and time. The space variables would alter the starting angles for each movement, while the time variables would change the starting instant for the motions. The study of these movement combinations was performed according to the following steps depicted in Figure 3.21.
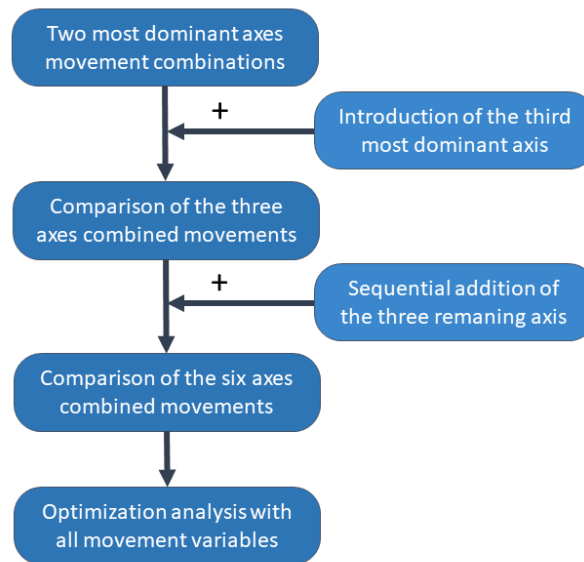
Figure 3.21 - Parameterization analyses approach

The successive introduction of the axes' motions was first performed to approximate the movement combinations to the critical system motion. At each motion added to the combined movement, the space and time variables of that axis were optimized to generate higher loads. With this, were obtained increasingly approximate movements to the critical one. At the end, a last optimization was performed with almost all studied variables to finally reach the highest base load motion.

After all this process, the critical robot movement was obtained. However, it is to be noted that this approach was far from being flawless. This methodology was based on initial assumptions and successively reducing the working space of the robot in order to approximate the system motion to the specific instant at which the load on the base is the highest possible. Unfortunately, this does not mean there are no movement configurations on other particular regions that cause higher force values. It can only be assumed that in case such a worse movement scenario exists its load is not far from the one here obtained.

During the following section, the execution of the simulation approach above mentioned will be described and the results obtained at each relevant step will be exposed and interpreted. The objective with the description of the work done is to make sure the reader following this text understands how those steps were realized, which considerations were taken and why.

3.4.1 Quasi-static Analysis

The static study of the system was divided in three steps. Firstly, the motions of the second and third axis were defined by displacement functions to prescribe the working envelop described at COMAU datasheets - Figure 3.22. While the shown path was being followed, the other axes were locked at their calibration configuration – 0°.
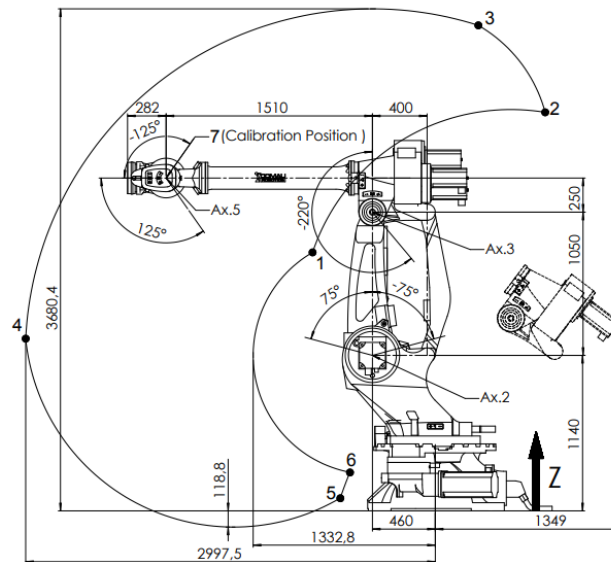
Figure 3.22 - COMAU NJ290-3.0 working area (Comau 2021)

A Quasi-static type of simulation was performed with a small output step. This simulation evaluates the static equilibrium of the system at each time step along the prescribed motion path. After the simulation, the values of torque and force magnitudes at the Base joint were plotted. It was observed that the force magnitude was constant $F = 24418,4N$ through all the working envelop. This made sense, as the only external force exerted was the gravity. From the equilibrium torque plot, was identified the region with the highest magnitude value. Since the static force at the base joint was not constant for any system configuration, only the magnitude moment was studied from this point on. Knowing the general location where the static load was higher, an optimization analysis focused on increasing this value was performed around that smaller working space. This way, it was possible to obtain the exact angles that generated the highest torque along the working envelop path. From this optimization process, the following angles of the second and third axes were obtained - Table 3.2.

Table 3.2 - Critical static configuration around the robot work envelop

AXIS	ANGLE	TORQUE [Nm]
2	75°	
3	-55,6°	23428,9

With the critical point along the envelop path discovered, the angles of the second and third axes corresponding to that configuration were made constant and the influence of the first axis angle was studied. The robot model was defined to rotate through all the first axis range (or stroke). The objective here was to find the exact angle that generated the highest reaction moments at a supporting structure. Like the above case, the torque variation around the entire axis' range was analyzed and then a subsequent optimization around the most stressful region was performed. This resulted in a first axis angle equal to 133,1° with a corresponding the static magnitude moment of 24537,6Nm.
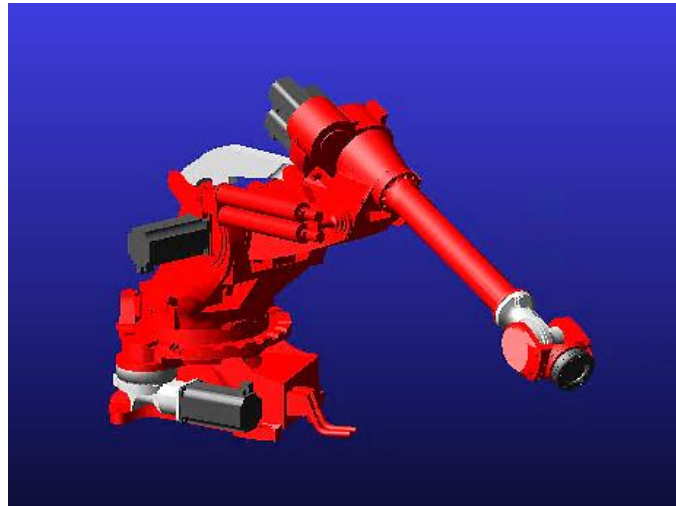
Figure 3.23 - Critical static position of the robot model

The same procedure was executed for the fifth axis to reach the critical static configuration of the robot. The fourth and sixth axes were not evaluated, because they would not cause any displacement of the center of masses of the bodies. From the fifth axis quasi-static and optimization analyses, it was found that the -19,4° angle exerted the highest value of 24636,3Nm at the base joint. Figure 3.23 depicts that robot configuration.

At last, a final optimization about the neighborhood of that robot configuration was performed by varying the angular values of the four axes. This resulted in a new pose with higher load exerted on the structure. Therefore, this new configuration was considered as the model critical configuration - Table 3.3.

Table 3.3 – Model critical static configuration of the robot model

AXIS	ANGLE [°]	MAX TORQUE [Nm]
1	136,5	
2	75	
3	-53	
4	0	24654,0
5	-19,3	
6	0	

3.4.2 Separate Axes Motion Analyses

As was mentioned above, this group of simulations had the objective to identify the type of movement for each axis that increased the most the reactions on the base joint. To do so the velocity functions of each motion were defined to perform the following three movement types: constant rotation at maximum speed, acceleration from rest to maximum speed, and deceleration (braking) from maximum speed to rest. Once the desired motions were defined, the system was kinematically simulated to obtain the highest torque and force values registered throughout the simulation. For each type of motion, the following procedure was implemented.

- Define the velocity function according to the type of movement.
- Define the practical axis working range for that motion.
- Simulate the desired motion at different starting angles through a parametric analysis.

For each movement it was first necessary to write the function that would describe the desired velocity profile of that axis. For the first movement type, that was an easy task – simply write the value that corresponded to the angular displacement per unit of time. However, for the acceleration and deceleration cases it was necessary to take other aspects into consideration. These aspects are later discussed in the text.

With the velocity functions defined, it was necessary to select the "practical" working range for each axis. Some movements, although possible to simulate on ADAMS, were not realistic. These include for example braking at the end of the axis stroke. Such a motion would make some model parts penetrate the geometry of others. Therefore, for each axis' movement type was calculated a range within that motion could be physically performed.

At last, a design variable was created for the initial displacement condition of the motion – the starting angle. Through a parametric analysis of this variable, it was possible to run multiple simulations with the same velocity function starting the movement at different positions of the axis. This allowed to better cover the possible locations where the studied movement type could be executed. At the same time, this was the variable used to ensure the motion was performed within practical working range. To do so, it was decided to evaluate all starting angles until a limit value equal to the angle stroke subtracted by the minimum acceleration or braking distance angles on that rotation orientation.

It is important to remember that the purpose of this study with the axes' motions was not to find the exact axis movement that would generate the highest stresses at the bottom, but instead to have a general idea on how much one type of movement could increase the static values in comparison to another. The critical starting angles – that correspond to the exact positions where each axes critical motions are initiated – were not the concern of this step. Here it was only intended to have a broad understanding of the axis motions influence on the maximum load values. Thus, the parametric study of the initial condition variables only analyzed 25 different starting angles equally spaced along the practical stroke, instead of searching for the critical one.

In the following sections the work done for each type of motion is described and the results obtained for the maximum magnitude forces and moments at the Base joint are shown.

3.4.2.1 Maximum angular velocity motion

The maximum angular velocity cases were the simplest to evaluate. Their velocity function was a constant equal or symmetric to the given velocity value on the technical specifications of the physical robot (Comau 2021). Since the motions were constant, there was no need to define nor study the starting angles influence. Instead, the movements were simply performed inside the practical working range for each axis. For the fourth and sixth axes - as the angle stroke for both is +/- 2700° - the movement was only analyzed inside 0° and 360°. In Figure 3.24 the force and torque magnitude values for the fifth axis counterclockwise (CC) – or positive – motion are shown.
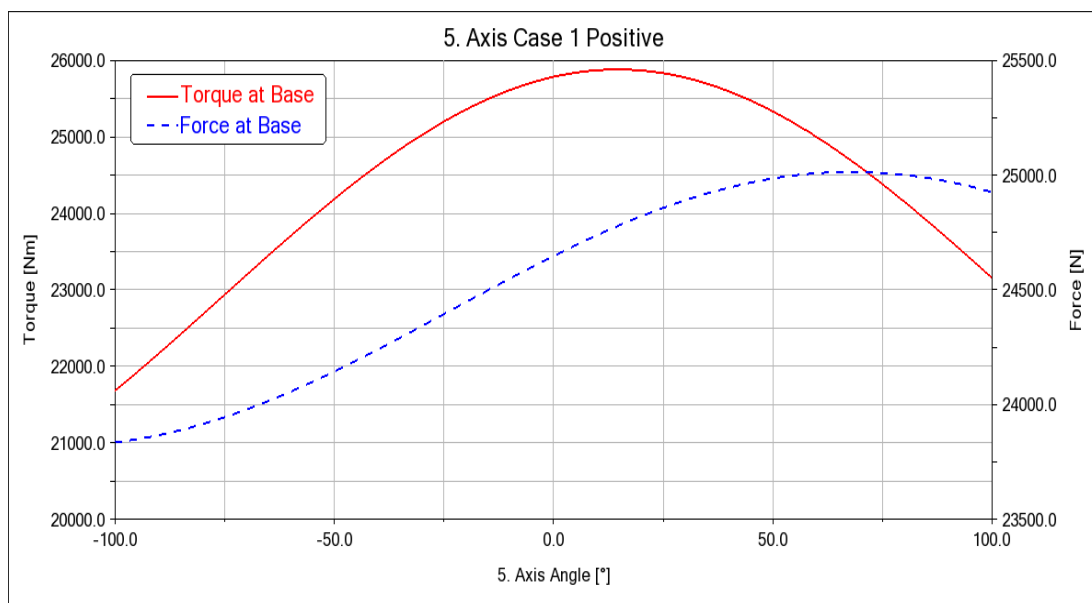
Figure 3.24 - Force and Torque magnitude exerted on the base joint during full speed motion of the fifth axis

As it can be seen, the load values were analyzed for a motion describing its path between the ends of the practical stroke -100° to +100° - instead of the real achievable stroke - ±125°. The maximum torque registered throughout the motion at 105°/s equals 25881,9Nm and the maximum force 25014,1N. These correspond to an increase of 4,98% and 2,44% of moment and force magnitude values, respectively. Table 3.4 shows the results obtained from the remaining axes maximum speed motions.

The values shown do not distinguish for the negative or positive rotation orientation because the maximum load results were equal. Actually, the torque and force plots with inverse orientations were symmetric. In the second axis case, the maximum load results occurred at the end of the allowable angle variation - at 61°. This means, the maximum results were developed at the exact instant at which the axis needs to start braking not to impact its angle range limit. This angular restriction on the motion explains why the magnitude force for the second axis is lower than the static value. Another interesting aspect revealed by the analysis was the constant force for the first axis throughout all its motion. It was later thought that this might happen because the first axis is the only one which rotates parallel to the base. In other

terms, the center of mass of the overall system is rotating around the first axis at a constant distance from it.

Table 3.4 - Maximum Torque and Force Magnitude values from the full speed motion at each separate axis

AXIS	MAX TORQUE (INCREASE%)	MAX FORCE (INCREASE %)
1	**32272,7Nm (30,90%)**	25153,5N (3,01%)
2	27163,4Nm (10,63%)*	23021,9N (-5,54%)*
3	27548,7Nm (11,74%)	**26188,3N (7,25%)**
4	24790,2Nm (0,55%)	24601,5N (0,75%)
5	25881,9Nm (4,98%)	25014,1N (2,44%)
6	24655,9 Nm (0,008%)	24419,0N (0,002%)

3.4.2.2 Rest to maximum angular velocity motion

For the acceleration case, it was necessary to define a velocity or acceleration function and attribute a design variable to the initial displacement condition. It was preferred to characterize the velocity instead of the acceleration, due to its easier definition, not to let the angular velocity exceed the values specified by the robot manufacturer. The type of function utilized was a so-called STEP function.
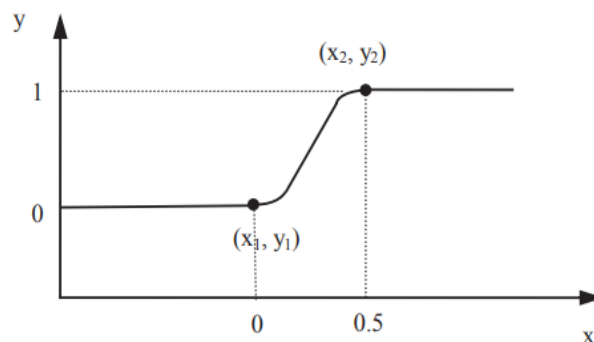
Figure 3.25 - STEP function in ADAMS

This type of function was selected because it allows a smooth transition between two specific values. This function is incorporated in ADAMS library and can be utilized as a smooth ramp function, instead of an instantaneous step as its name would suggest. The STEP function uses a cubic polynomial to smooth the variation from one state to another, as shown in Figure 3.25. The user defines both state values and the duration of the transition – starting and ending time instants. Hence, for the acceleration motions it was only necessary to set the initial velocity to 0°/s, the final velocity to the axis correspondent maximum speed, and select a duration for the transition.

However, the motion characteristics of the NJ290-3.0 robot axes are dependent on the utilized Control Unit. In addition, there was no information on the achievable angular accelerations at each axis. These values are important to define the velocity functions with duration transitions that correspond to acceleration profiles similar to the physical ones. Fortunately, SIEMENS – a partner company of this project – had already worked with these industrial machines and made a report on some of its mechanical and dynamic characteristics. In it were presented the braking times and distances for the first three axes when under different load and velocity conditions. With no other source to guide the characterization of the STEP functions, it was assumed that the braking times were equal to the acceleration times. But, despite having chosen the same transition duration as the braking times, that did not ensure that the model accelerations were close to the practical case.

The STEP function is a cubic polynomial, which means its derivative – corresponding in this case to the acceleration – is a quadratic polynomial. Although there was no information regarding the physical acceleration profiles, at least the braking distances were known. Since the braking times were assumed equals as the acceleration times, then also the braking distances must be equal to the acceleration ones. The SIEMENS braking distances could be used to validate the chosen velocity functions. Higher numerical braking lengths would imply lower accelerations than the physical mechanism and vice-versa. With this the three axes motions were simulated and the acceleration distances were taken.

The numerical results showed slightly higher lengths than the practical ones. To be on the safe side of the construction design, the duration times of the velocity functions on ADAMS were reduced by the same relative error difference. After simulating these motions was noted that the distances were practically the same as the ones prescribed by SIEMENS. Therefore, it was decided to keep those modified transition durations – 0,724s, 0,309s, and 0,342s for the three axes, respectively by order.
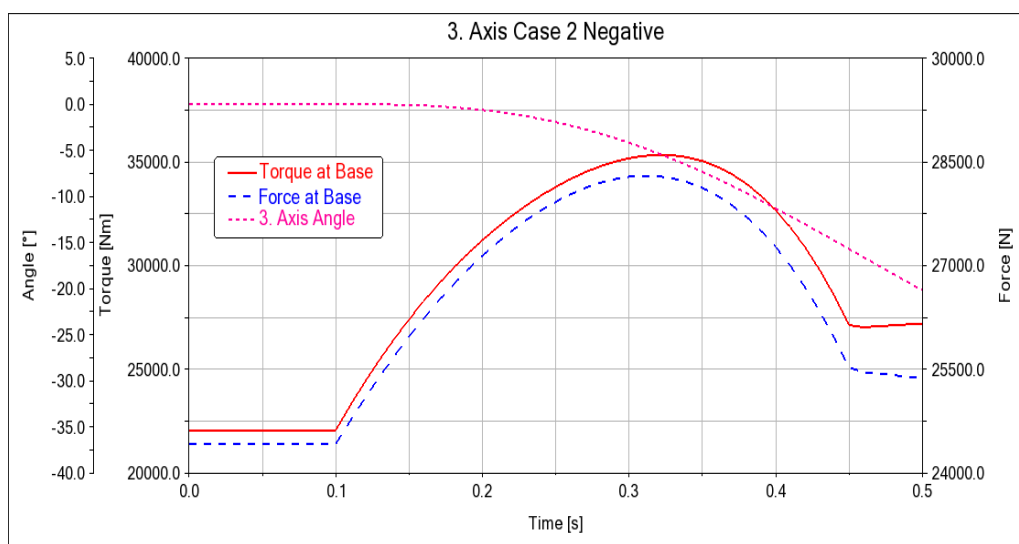
Figure 3.26 - Force and Torque magnitude exerted on the base joint during acceleration of the third axis

In Figure 3.26 can be observed the plots of the base joint magnitude forces due to the clockwise – C - acceleration motion of the third axis starting at 0°. The defined motion started with the robot at rest, then at 0,1s it initiated its rotation until it reached the 90°/s. The

movement was not started immediately to avoid any initial solver integration problems, and for the same reason it kept running until 0,5s. This late actuation beginning and prolonged solution time were done for all following motion analysis.

After defining the velocity functions of the first three axes, it was time to turn the attention to the remaining three, which still had no transition duration for their STEP functions. The selection of those times was made by a comparison with the ones of the first three axes. The last three axes have less masses to move, but their electric motors have lower power too and their maximum velocities are higher. Therefore, an acceleration time of 0,5s was chosen for all axes. This was for sure a rough assumption based only in pure intuition, but no better option was found.

The design variables created to simulate the acceleration at different starting angles could vary between both ends of the axis' practical range for this movement type. Take for example the fifth axis practical stroke depicted in Figure 3.27. With a working range of ±125° and 26° of braking distance, a counterclockwise – positive - acceleration could start between -125° and 73°. In this way the latest beginning of the motion would take the axis to reach maximum velocity at the exact moment where it was required to brake. As was above mentioned, a parametric analysis with 25 simulations inside the practical workspace was performed for each axis' motion. These analyses were performed by design studies focused on the maximum torque and force magnitude values registered during each simulation for the different starting positions.
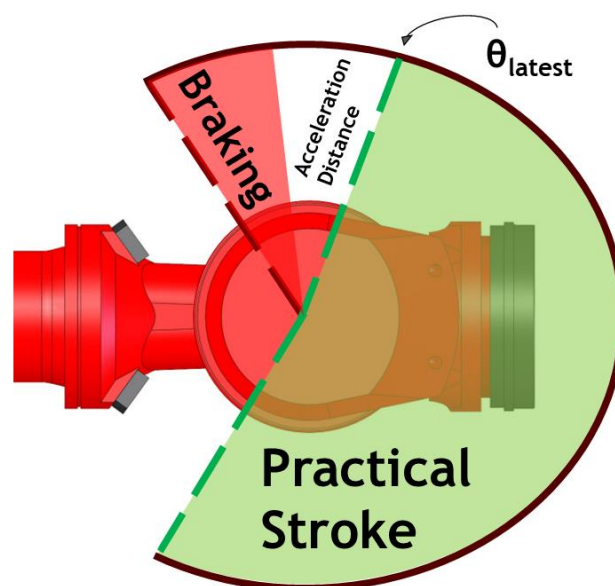
Figure 3.27 - Representation of the practical stroke for the positive acceleration of the fifth axis

In Table 3.5 are shown the simulation results for all acceleration motions. The presented values were the maximum registered through all 25 motion analyses with different starting angles. The rotation orientation is referred as C for Clockwise – negative – and CC for counterclockwise – positive. The percentages shown are the relative increase in relation to the critical static load.

Table 3.5 - Magnitude torque and force variation exerted at base joint. Results marqued by * have the same values as the full speed case

AXIS	MAX SPEED	TRANSIT TIME	ORIENTATION	TORQUE (INCREASE %)	FORCE (INCREASE %)
1	90°/s	0,724s	CC	347673,4Nm (41,0%)	25695,1N (5,2%)
			C	33653,3Nm (36,5%)	25695,1N (5,2%)
2	90°/s	0,309s	CC	44150,8Nm (79,1%)	36614,0N (49,9%)
			C	**67556,7Nm (174%)**	**37460,0N (53,4%)**
3	90°/s	0,342s	CC	27548,7Nm (11,7%)*	26188,3N (7,2%)*
			C	41990,0Nm (70,3%)	29179,3N (19,5%)
4	105°/s	0,5s	CC	25360,2Nm (2,9%)	24721,3N (1,2%)
			C	25397,1Nm (3,0%)	24721,3N (1,2%)
5	105°/s	0,5s	CC	25881,9Nm (5,0%)*	25014,1N (2,4%)*
			C	28198,0Nm (14,8%)	25404,9N (4,0%)
6	160°/s	0,5s	CC	24656,1Nm (0,008%)*	24419,0N (0,002%)*
			C	24656,1Nm (0,008%)*	24419,0N (0,002%)*

As it can be taken from the table, the second axis is the one – by a large difference - that causes the highest torque and force values on a robot support. Once again, the sixth axis has insignificant influence on the load values. An important fact in these acceleration motions was the orientation of rotation. While executing these simulations it was noted that the movement orientations against the gravity were the ones that exerted higher loads. For example, the critical motion of the second axis occurred when this axis was required to accelerate from rest starting at 75° position, having to raise most of the robot structure against its own weight – as shown in Figure 3.28. These results suggest that the worst situation for the robot base joint load might be a combined acceleration from different axes against gravity.
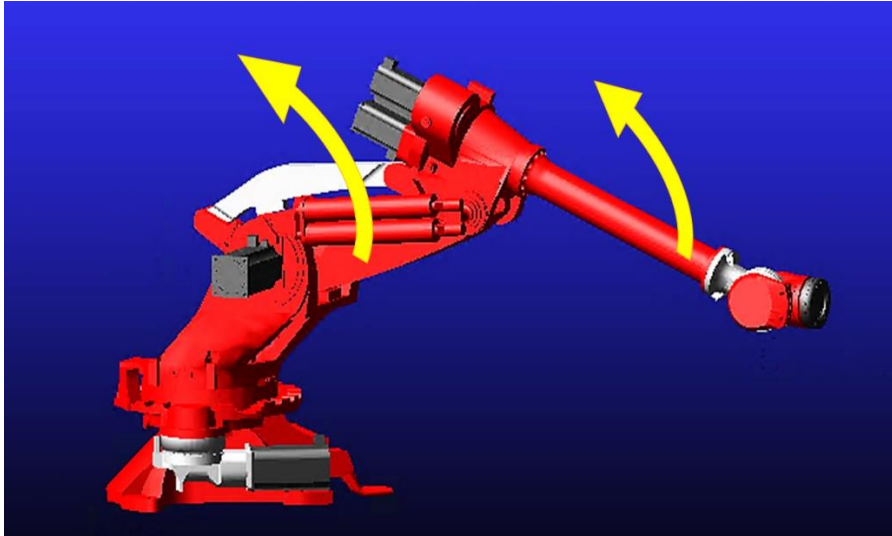
Figure 3.28 – Second axis acceleration movement

3.4.2.3 Emergency braking motion

The last type of movement studied was the braking situation from maximum angular velocity to rest. As was done for the previous acceleration case, the axes' velocity profiles were characterized by STEP functions and the varying initial positions by design variables. The durations of the function transitions were also the same as the acceleration case, but in this case, the initial state was rotating at maximum speed, while the final velocity was equal to zero. This required some careful treatment of the initial angle design variables.

As for the previous case, the braking motions were only defined to start at 0,1s of simulation. That meant, for the first 0,1s the axis would be rotating at maximum angular velocity. In other words, the starting angle of the motion was not the same angle at where the actually braking started – here called as braking angle. Because of this, the practical axes' ranges had to be adjusted – here called as adjusted working range or adjusted stroke -, so that it considered the initial motion at maximum velocity. This adjusted working range was equal to the practical braking range but subtracted by the angle described during the initial maximum speed motion. Unfortunately, the results obtained were related to the starting and not the actual braking angle. Hence, it was then necessary to convert those to calculate the angles at which the braking motions in fact started.

In Figure 3.29 is shown the torque and force variation during the deceleration motion of the second axis rotating on the negative orientation. This motion started at 0°– which corresponded to -9° braking angle. The simulation selected was the kinematic type and it was executed for 0,5s.
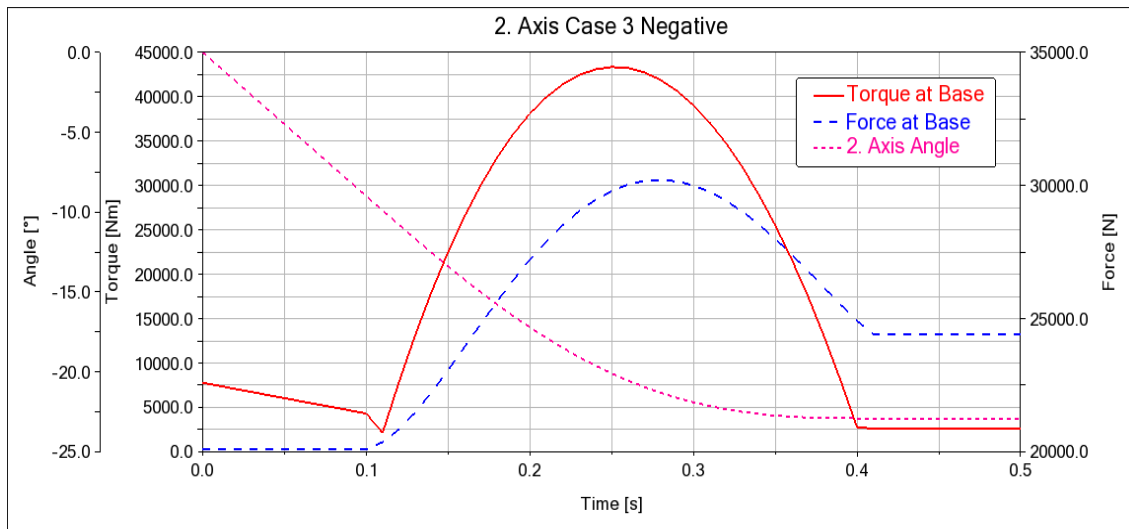
Figure 3.29 - Load variation at base joint during braking of the second axis

As was done for the acceleration, a parametric analysis was performed for each motion varying the design variable attributed to the initial conditions of the motion. The study was focused on the maximum values of torque and force throughout each simulation. In total the same braking motion was analyzed with 25 different starting angles. Table 3.6 presents the highest values obtained for the deceleration type of motion of the different axes.

Table 3.6 - Magnitude torque and force variation at the base joint for each axis braking motion. Rotation orientation CC: Counterclockwise. C: Clockwise

AXIS	ORIENTATION	MAX TORQUE (%)	MAX FORCE (%)
1	CC	34847,4Nm (41,3%)	25695,1N (5,2%)
	C	34485,4Nm (39,9%)	25695,1N (5,2%)
2	CC	**69004,7Nm (180%)**	37410,7N (53,2%)
	C	44944,4Nm (82,3%)	**37669,5N (54,3%)**
3	CC	42648,1Nm (73,0%)	29319,1N (20,1%)
	C	27548,8Nm (11,7%)*	26188,3N (7,2%)*
4	CC	25402,4Nm (3,0%)	24722,1N (1,2%)
	C	25348,7Nm (2,8%)	24721,0N (1,2%)
5	CC	28306,0Nm (14,8%)	25406,3N (4,0%)
	C	25881,9Nm (5,0%)*	24418,4N (2,7%)
6	CC	24656,1Nm (0,008%)*	24419,0N (0,002%)*
	C	24656,1Nm (0,008%)*	24419,0N (0,002%)*

As it can be seen, the second axis motion generated again the highest loads at the base structure. However, it is interesting to note that the movement orientation that generates the highest torque is not the same that requires the highest forces. Both motions are decelerating the robot arm against the gravity, but on different ends of the axis working range. As expected, those are the motions that put higher stresses on the base joint. Anyway, the difference on the maximum magnitude force generated is low between both rotating directions, while the magnitude torque is much higher on the positive motion.

3.4.2.4 Outcome of the separate axes motion analyses

By comparing the results from this table with the previous acceleration results, it is possible to notice that pairs of motion have close maximum load values. The acceleration with clockwise – negative - rotation has similar results to the braking at counterclockwise – positive – for every axis. The same happens on the opposite case. This makes sense, since the reaction forces at the base joint are related to the angular acceleration caused by the axis movements. Even if the movements are different, the accelerations are oriented on the same directions. The objective in this step of the motion study was to find the critical motion type for each axis and the results for this step are shown in Table 3.7.

Table 3.7 - Critical Motion for each axis and respective maximum magnitude torque and force registered

AXIS	CRITICAL MOTION TYPES	MAX TORQUE	MAX FORCE
1	Acce C / Braking CC	34847,4Nm	25695,1N
2	Acce C / Braking CC	69004,7Nm	37669,5N
3	Acce C / Braking CC	42648,1Nm	29319,1N
4	Acce C / Braking CC	25402,4Nm	24722,1N
5	Acce C / Braking CC	28306,0Nm	25406,3N
6	Max Speed CC/C	24655,9Nm	244190,0N

At the end, this study of the general axe's types of motions gave a good idea of which movements lead to the critical stress situation at the base joint. The second axis was found to be the dominant on exerting the base load, while the sixth and fourth axis did not reveal a significant influence on the results. Knowing that the movements which generate high accelerations against the gravity are the critical ones for the structure, on the next step of this study approach the relation between axes' movements was analyzed.

3.4.3 Combined Axes Motion Analyses

In this section are presented the parametric analyses performed to obtain the combined movement that generates the highest load on the base structure. Through the previous step of analyzing the separate influence of the axes, the critical types of movements for each one of them were discovered. In this phase of the motion study, those motions from different axes were combined to reach the highest load possible on the base joint. Naturally, it would be impractical to test every possible movement combination. Each axis has two critical movements (accelerating and braking against gravity or rotating at maximum speed on both directions) which would result in $2^6 = 64$ combinations. Even if the sixth axis were neglected, it would still be necessary to study 32 movement combinations. To reduce the amount of simulations, the following approach was defined:

1. Study the four movement combinations generated by the simultaneous movement of the two most dominant axes – the second and third.
2. Increase sequentially the number of moving axes in respect to their individual influence on the structure load.
3. Parametric analyses and final optimizations with the selected design parameters.

Firstly, the two critical axes were analyzed for its possible critical movement combinations. Because of their strong influence on the base joint load, it was chosen to study all 4 movement interactions to be sure no relevant combination was left out. Thus, all critical movement combinations were covered and the one that generated the highest load was found.

Having determined the critical motion from the two dominant axes, it was then necessary to sequentially introduce the remaining axis motions to the overall system movement and analyze their influence. At each one of these, both movements – acceleration and deceleration - were analyzed always focusing in increasing the previously highest load found. At the end, a robot motion with all axis rotating was identified as the critical type of movement for the fixed joint.

The procedure applied for these previous steps was to compare different movement combinations and then select the one with higher results to proceed to the next phase of the study. In other words, at each introduced axes only a single movement combination was selected to go forward, while the other option was excluded. Due to this "Go/ No Go" comparison, there is the possibility that relevant combinations were not even considered, since they were previously eliminated. Nevertheless, the fact that the most dominant axes were studied at the beginning reduced the probability that non-tested combinations could exert higher loads than the studied ones.

Lastly, a series of design of experiments and optimizations was executed to achieve the movement that generated the highest load possible. After adding all axes motions it was known which was the critical type of movement of the whole system, nevertheless the exact worse movement was not yet found. It was still necessary to work the velocity profile variables that influence the combination of the different axes. By first performing design of experiments with those variables it was possible to approximate those parameters to the critical movement. Then, a final optimization was executed to find the set of design variables that caused the worst possible movement for the supporting structure. Those parameters and the velocity functions of the axes were then considered as the movements requirements that achieved the critical scenario for the base joint of the numerical system.

Before entering the explanation of the work done for each step of these analyses, it is important to refer that from this point on only the reaction magnitude torque at the base joint was studied. This was done to reduce the number of simulations to perform. Besides, the movement that generates the highest moment at the base is certainly not the same that generates the highest reaction forces. Seeing that the torque values registered during the previous simulations were much higher than the forces – in comparison to the respective static values -, it was decided that the critical movement for the supporting joint was the one that exerted the highest magnitude torque.

3.4.3.1 Second and Third Axes Combination

These two axes have each 2 critical motions, resulting in a total of 4 different combinations. These movement combinations were defined by selecting the velocity function correspondent to the intended axis critical rotation. Next Figure 3.30 shows the base load variation through one of these combined movements. To obtain the worst movement possible, the combined motions were tested with different initial displacement conditions – starting angles. The motions' starting conditions have strong influence on the overall movement the system performs, which in turn varies profoundly the load exerted at the base. As a consequence, to each of these initial parameters was attributed a design variable to study their interaction through Design of Experiments analyses.
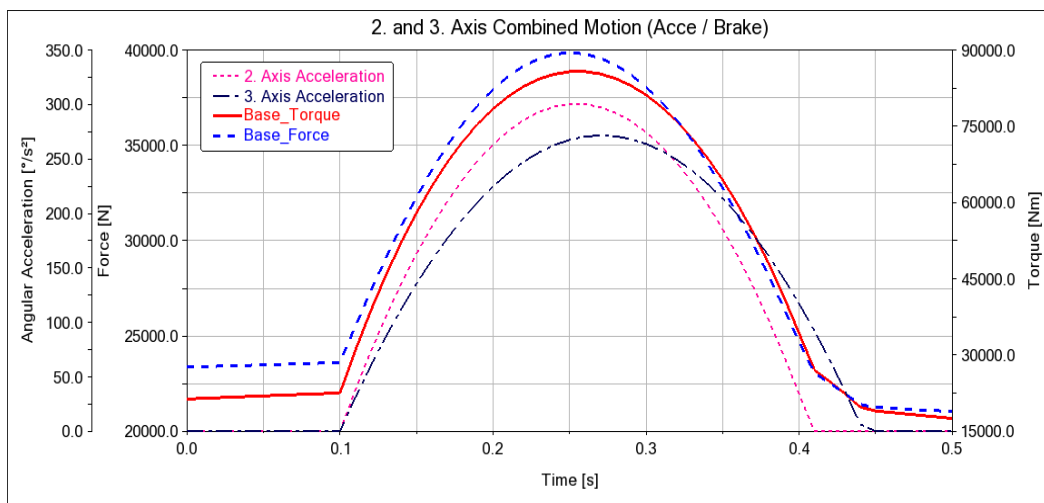
Figure 3.30 - Numerical results obtained from one combined motion of the second (accelerating) with the third (braking) axes.

Another characteristic that affects the combined motion is the relative time offset. It was thought that the time difference between the start of each motion was relevant for the results obtained. Controlling that parameter would allow to approximate the time instants at which both axes had maximum acceleration values, increasing the load exerted. Hence, a time variable was created and added to one of the axis' velocity functions – the third axis - to represent the offset between the start of its motion relative to the other axis – the second. This variable was made constant at zero during the study of the starting angles, being only considered later in a specific Design Study. In total the combinations of the two axes

movements were analyzed under the influence of three parameters: two spatial conditions and one time displacement.

Thus, each of the four movement combinations was submitted to at least three parametric analyses – 2 Design of Experiments and 1 Design Study. The first two were performed to obtain the set of starting angles that resulted in a combined movement close to the worst scenario for that movement combination. The first analysis evaluated the magnitude torque variation with motions starting at different angles around all their practical working ranges. The second restrained the working range to 10% around the simulation with the highest value from the previous analysis. At last, the time offset variable was separately studied, varying its value between -0,05s and +0,05s.

The default level of the first design of experiments was 10, resulting in 100 total simulations with different starting conditions, while the second analysis used a default level of 5, resulting in 25 different simulations. In the time variable design study, a total of 10 simulations were executed within the defined interval range. The set of starting angles and time displacement which generated the combined movement with the heaviest load on the structure was selected as the worst case found for that movement combination. In Table 3.8 are presented the highest values obtained at the end of these analyses for the four combined motions.

Table 3.8 - Maximum Torque for each movement combination. *Limit angle range

MOVEMENT COMBINATION 2. AXIS / 3. AXIS	STARTING ANGLE 2. AXIS / 3. AXIS	TIME OFFSET	MAX TORQUE
Acceleration C / Acceleration C	41,0° / -30°*	-0,039s	89138,5Nm
Braking CC / Braking CC	21,5° / -54°*	0,016s	**89213,7Nm**
Acceleration C / Braking CC	13,9° / -30°*	0,016s	85899,5Nm
Braking CC / Acceleration C	41,0° / -54°*	-0,028s	86337,9Nm

As it can be seen, the braking at both axes is the combined movement that exerts the highest torque at the bottom. However, the acceleration at both also produced close results. For this reason, both combined movements were further submitted to an optimization process to obtain the respective critical configuration of the three parameters. The varying interval chosen for each variable was equal to 30% of the previous interval used in each respective analysis. In this way, the most stressful movement for each of the two motions were found. For the acceleration at both axes, the optimization process resulted in a maximum magnitude torque of 89157,4Nm, while for the braking case it was 89218,0Nm. With results so close to one another – 0.07% difference –, it was decided to proceed the parametric analysis with both movements. Although the acceleration on both axes might exert a lower torque than the braking situation, it could happen that by adding another axis' movement the overall motion of the system generated a higher load than the any other movement. Unfortunately, that also

meant executing the double amount of simulations by carrying both combined movements to the next phase of the study.

3.4.3.2 First Axis Introduction

After selecting the critical movements from the second and third axes combination, the first axis rotation was added to the system. The individual critical motions of this axis were the clockwise acceleration and counterclockwise deceleration. These rotations were added by defining the STEP functions that corresponded to those velocity profiles. As was done for the previous case, a design variable was referenced to the initial displacement condition of this axis and a new time offset parameter was created in relation to the second axis starting motion. From here on, the actuation of the second axis was always considered the time reference for the motion of the other axes.

The time variable for this axis needed more care, due to the large duration of its STEP function transition. This transition developed in 0,724s, while the other two axes took 0,309s and 0,342s. That meant, if the maximum accelerations of the three motions were to be close in time, the first axis' motion should start around 0,2s before the others. That was problematic because the second and third axes motions started at 0,1s of the simulation, meaning it would be impossible to impose an advance of 0,2s on the first motion. Above that, it was decided to study the first axis time variable between -0,7s and 0,4s, so that it covered all possible starting times in relation to the other axes. With a 0,7s advance, the acceleration or deceleration of the first axis was almost complete when the other axes initiated their motions, or with 0,4s delay the other axes had already finished their motion when the first axis was starting.

To be able to study that entire time offset range, it was necessary to delay the starting times of the other velocity functions. Thus, it was chosen to start the acceleration or deceleration of the reference axis at time instant 0,8s and simulate the motion until 1,2s – short after the movements of the second and third axes finished. Unfortunately, that required adjusting the starting angles of the combined braking movement, so that the braking angles were exactly the same as the ones obtained before. Therefore, it was necessary to account for that increased duration at maximum angular velocity and alter the varying range and values of the initial displacement parameters accordingly.

The analysis of the four combined movement types – 2 combined movements of the second and third axis X 2 critical movements of the first axis - were performed in different way than the previous case. For start, a design study with 25 simulations on the first axis starting angle was performed. This allowed the reduction of this parameter interval range for the next analysis. A design of experiments combining the starting angles of the three axes was further conducted with 4 default levels – totaling 64 simulations. The allowable parameter variation interval was equal to 5% of each joint working space. Since the first axis' time offset was not studied until this point, all simulations performed in these 2 analyses had the reference motion starting at 0,1s. In Figure 3.31 is shown the magnitude torque plot from one simulation at the end of this design of experiments analysis. Note how the acceleration of the first and second axes start at the same time instant.
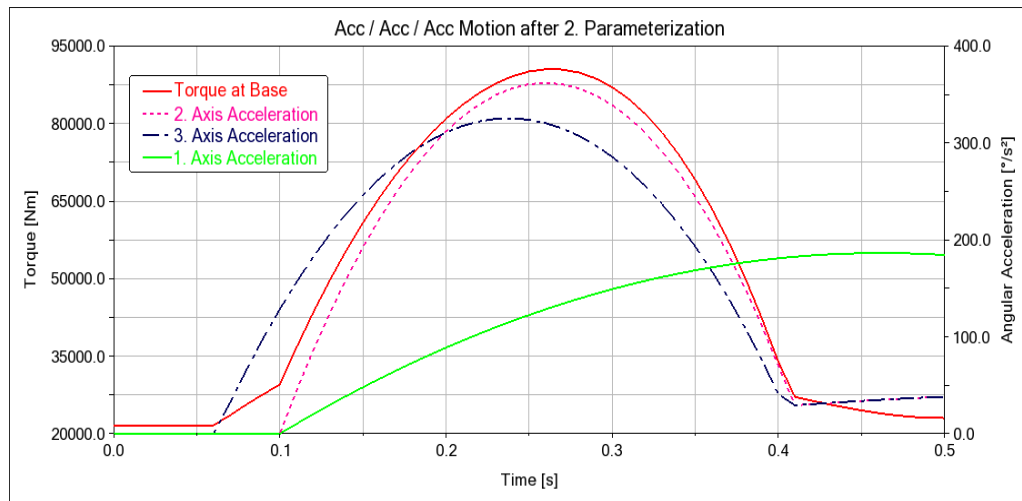
Figure 3.31 - Numerical results obtained from one combined motion of the first, second, and third axes - all accelerating.

Later, the design variables attributed to the initial conditions were made constant with the values that exerted the highest load on the base, and the first axis offset was submitted to a design of studies with 20 simulations. Here all velocity STEP functions were adjusted to start their motions at 0,8s as was already explained. With this analysis, the motion of the first axis was initiated at different points in time. The time offset that caused the highest load was then select as the worst value of that combined movement. Lastly, another design of studies was performed with the starting angle of the first axis varying its workspace range by 10% and wit a total of 20 simulations. This analysis was repeated to again obtain close to critical starting angles for the first axis' motion, because now the time offset values were taken into consideration. In Table 3.9 are exposed the maximum torque results at the end of this parameterization series for the four combined movements.

Table 3.9 - Maximum Torque for the 3 first axes movement combinations. *Max Torque occurs at 1. Axis max speed and not during braking

AXES MOVEMENT (1ST / 2ND / 3RD)	TIME OFFSET	MAX TORQUE	1. AXIS EVENT ANGLE	MAX TORQUE
Acce / Acce / Acce (A/A/A)	-0,525s	99729,9Nm	169,6°	99894,4Nm
Brak / Acce / Acce (B/A/A)	0,110s	100641,0Nm	118,1°	100658,8Nm
Acce / Brak / Brak (A/B/B)	-0,525s	99739,5Nm	146,6°	99791,7Nm
Brak / Brak / Brak (B/B/B)	0,168s*	99734,8Nm	135,8°	99779,8Nm*

From the previous table it can be seen that all movement combinations have close numerical results. The column "event angle" exposes the angle at which the desired motions starts and not the initial angle of the simulation. Basically, this term refers to the starting angles in the case of acceleration motions and the braking angles on the other case. Because the maximum torque on the critical B/B/B movement occurred while the first axis was still at maximum velocity, a quick evaluation of the base load was performed with the first axis rotating at maximum speed on both directions while the other two axes were decelerating. From that study it resulted that the torque values were 100091,4Nm and 99956,5Nm for clock- and counterclockwise, respectively. That meant, the full speed / braking / braking movements had higher stresses on the base than both A/B/B and B/B/B type of movements at the first axis. To clear any doubts, the same was tested for the full speed / acceleration / acceleration cases. The maximum torques registered on those combined movements were 99865,4Nm and 99992,0Nm, both slightly under the values presented on the above table.

This assured that the Braking / Acceleration / Acceleration combination from the first three axes was the one that generates the highest stresses on the base structure. It should be noted that even though the maximum moment occurs during the braking motion of the first axis, that instant was only a few microseconds after the braking starts. Since this difference is so small, in general it can be said that the overall critical motion for the robotic system involves the second and third axis accelerating against gravity, while the first axis is rotating at maximum velocity. Although there is only a slight torque difference between the different movements, this was the only one carried to the next phase of the robot study to reduce the number of simulations in the next steps. Another factor that supported this decision was that fact that the remaining three axes have low influence on the base load.

3.4.3.3 Introduction of the remaining axes

Having discovered the critical movement from the combination of the three axes with highest influence on the fixed joint, it was then necessary to add the remaining axes' motions to the system. This introduction of the last three axes was done sequentially in a very similar way as the parametric study that was performed for the first axis case. Having found the critical motion type for the first three axes - Braking / Acceleration / Acceleration (B/A/A) -, it was necessary to study the two most influential movements of each axis. The axes' velocity profiles were defined according to the respective STEP function starting their motion at the reference instant 0,8s. A design variable was also attributed to the initial displacement position, and a time variable was defined in relation to the second axis starting motion. The time variable was not created for the sixth axis, because its critical motion corresponds to constant maximum velocity, therefore the moment when the axis starts to rotate has no influence.

The study of each combined motion was started by a design study evaluating the maximum torque variation at different starting angles of the newly introduced rotation. The number of simulations performed along the practical axes' strokes were 25 for all axes. After this first analysis, a new design study was executed with a shorter varying interval – 10% variation of the axis' workspace. In this second parametric analysis, the number of simulations ran was 20. The objective here was to approximate the initial displacement parameters to their critical values and reduce as much as possible their varying range. After the second design study, the worst starting angle for the added axis was selected and the influence of the time variable was

studied. Since the first two remaining axes have 0,5s transition duration of their velocity profiles, the time offset variable was allowed to vary between -0,5s and 0,4s. The parametric study of this parameter was performed with 20 simulations. This resulted in an approximate value for the critical time offset. When braking cases were being studied, their initial motion position was adjusted according to the time variable as was done for the first axis braking motion. No further analyses were performed on the starting angles with the new time offsets because it was considered that the magnitude moment would not vary substantially.

In the next Figure 3.32 are shown the accelerations of the five axes throughout a B/A/A/A/A motion. The accelerations never return to zero, although their maximum angular velocities had already been achieved, because these measures are not the relative angular accelerations between adjacent bodies of a joint. For this reason, the accelerations shown are affected by the braking motion of the first axis.
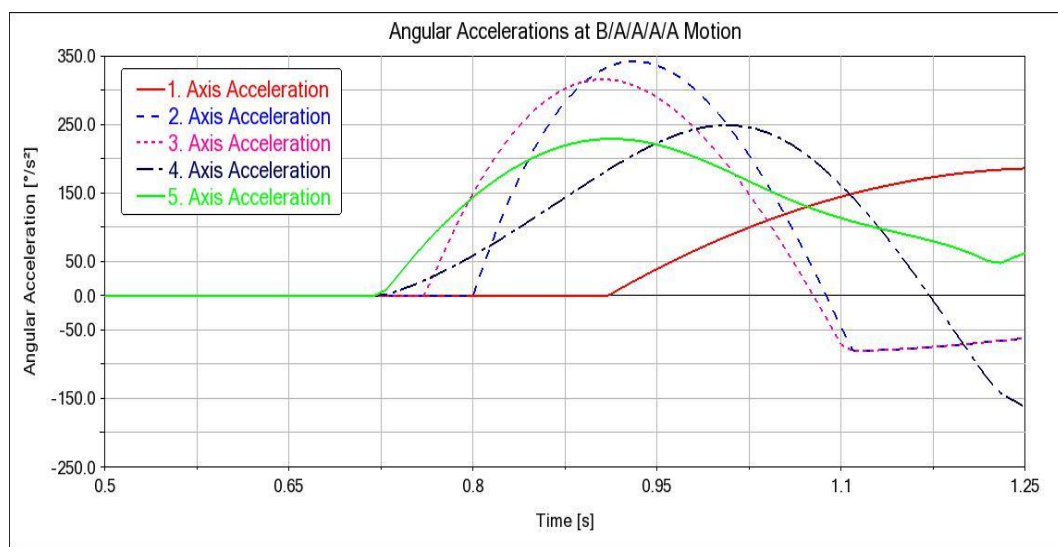
Figure 3.32 - Angular accelerations of the different axes during the combined motion

No design of experiments - combining different starting angles from all moving axes - were performed due to the big number of simulations it would require and low influence on the overall results obtained. This was later addressed in the next step of the parametric study of the robot, so worst combination of all axes starting angles would be eventually covered. To sum up, the following parametric analyses performed for each axis' motion were:

- Design Study (Initial Condition Variable) with 25 simulations within the practical axis' range.
- Design Study (Initial Condition Variable) with 20 simulations around 10% variation of the worst previous case.
- Design Study (Time Variable) with 20 simulations varying between -0,5 and 0,4s.

Performing the above-mentioned analyses approach sequentially for the introduction of the three-remaining axes resulted in the torque values presented in Table 3.10.

Table 3.10 – Numerical results obtained for the combined movement of each added axis. *Maximum Torque achieved with full speed rotation.

ADDED AXIS	MOVEMENT	TIME OFFSET	EVENT ANGLE	MAX TORQUE
5	Acceleration C	-0,074s	-27,6°	**105336,4**Nm
	Braking CC	-0,074s	-58,0°	104222,3Nm
4	Acceleration C	-0,074s	10,3°	**105487,8**Nm
	Braking CC	>0,2s*	-58,8°	104555,7Nm
6	CC Rotation	---	161,2°	105562,3Nm
	C Rotation	---	-56,2°	**105563,0**Nm

The first thing that can be noticed – and was already expected – is that the increase on the maximum load is smaller at each added axis. Adding the fifth axis' motion to the system only increased the previous maximum torque at the base by 4%, and the difference to the other axes was successively smaller. The introduction of the sixth axis movement brought practically no influence on the base torque value – around 0,07%. For this reason, only the first parametric analysis around the axis stroke was performed, since the load variation between distant angles was so small. With the sixth axis added, the critical type of movement for the whole robotic model was obtained.

3.4.3.4 Velocity Parameters Optimization

At this point, the worst movement type for the base structure was known. All axes were rotating at some instant generating very high reaction moments at the bottom of the virtual mechanism. However, the approach taken until here was only intended to obtain a good approximation of the highest load situation. The axes movements were added on top of the previous obtained motions, not fully combining all possible parameters into the overall robot motion. That was the intended purpose for this part of the study. To define all the variables that influence the overall motion of the system and combine them to reach the highest possible magnitude torque scenario.

In this last group of parameterization analyses, a total of 10 parameters were considered to have influence on the base joint load – the six axes' initial positions and four variables carrying the time offsets. The time offsets were applied at every axis, except the second – the reference axis – and the sixth which had constant rotation movement. These ten variables were studied until the motion that causes the highest torque at the base was discovered. The easiest way would be to perform an optimization analysis with all ten variables, but it was impossible to predict how long that analysis would take. Therefore, it was decided to first divide the study in two parts each with 5 parameters to analyze. Thus, it was possible to approximate the axes motions to the overall critical motion with a reduced number of variables evaluated simultaneously. The first part was responsible for obtaining the critical combined movement of the first three axes, and the second part the respective movement of the remaining three revolute joints. After that a final optimization with all parameters was performed to obtain the worst movement possible to the base joint.

The search for the critical combined movement of the three dominant axes was performed through the following analyses:

1. Design Study (3rd axis initial angles) with 10 simulations between -30° and -28°.
2. Design of Experiments (1st and 2nd axes initial angles) with 49 total simulations varying 4% the variables interval from the previous critical values.
3. Design of Experiments (1st and 2nd axis initial angles plus 1st and 3rd axes time offsets) with 81 simulations varying 1,2% the angle stroke interval and 0.1s the times interval.
4. Optimization with all 5 variables.

The initial design study with only the third axis angle was made to confirm that its value on the edge of the practical working stroke was clearly the critical one. This allowed the reduction of the number of variables to 4. The following analysis were intended to successively approximate the solutions to the worst movement combination, until an optimization was performed with all five variables. This resulted in the critical parameter solution for the combined motion of these three axes. Next Table 3.11 presents the results obtained throughout this study approach.

Table 3.11 - Results obtained from the optimization approach of the first three axes.

PARAMETERIZATION	VARIABLES STUDIED	SOLUTION	MAX TORQUE [NM]
1 - DESIGN STUDY	A3	-30°	105563,0
2 – DESIGN OF EXP.	A1/ A2	36,2° / 36,9°	105563,0
3 – DESIGN OF EXP.	A1/ A2/ T1/ T3	36,2°*/ 36,9° / 0,110s/ -0,039s	105560,9
4 – OPTIMIZATION	A1/ A2/ A3/ T1/ T3	36,4°*/ 36,9° / -30° / 0,100s/ -0,034s	105595,7

Knowing the critical movement of the first three axes, the remaining three axes were then treated to obtain their own highest load situation. The sequence of analyses executed were as follows,

1. Design of Experiments (4th and 5th axis initial angles) with 49 simulations varying its range interval by 4%.
2. Design of Experiments (4th and 5th axis angles plus 4th and 5th time variables) with 81 simulations and varying 1,2% for the angle parameters and 0,1s for the time.
3. Design Study (6th axis starting angle) with 25 parameters varying 10% its stroke.
4. Optimization with all 5 variables.

In Table 3.12 are presented the results obtained for each phase of this study with the last three axes.

Table 3.12 - Results obtained from the optimization approach of the last three axes

PARAMETERIZATION	VARIABLES STUDIED	SOLUTION	MAX TORQUE [NM]
1 – DESIGN OF EXP.	A4/ A5	18,7° / -23,7°	105695,4
2 – DESIGN OF EXP.	A4/ A5/ T4/ T5	23° / -20,7° / -0,164s / -0,119s	105876,8
3 – DESIGN STUDY	A6	-42°	105877,0
4 – OPTIMIZATION	A4/ A5/ A6/ T4/ T5	29,4° / -21,4° / -42,6° / -0,186s / -0,112s	105921,4

With this, the separate critical movements for the two groups of axes were finally achieved. It was then only necessary to blend these two movements and obtain the system motion that generated the highest torque at the base. Therefore, a last optimization analysis was performed with eight variables. The initial conditions for the 3rd and 6th axis were left outside this parameterization, due to their already known value and practically insignificant influence, respectively. In next Table 3.13 are presented the parameters solution that compose the overall critical movement to sustain this mathematical model.

Table 3.13 - Robot model critical movement parameters. Sixth axis angle at the instant when the second axis starts its motion

AXIS	MOVEMENT	TIME OFFSET	EVENT ANGLE
1	Braking	0,097s	108,8°
2	Accelerating	Reference Time	-37,33°
3	Accelerating	-0,034s	-30°
4	Accelerating	-0,198s	30,82°
5	Accelerating	-0,112s	-21,51°
6	Negative Rotation	---	170,6°*

This movement resulted in a maximum magnitude torque of 105925,1Nm - the outcome of the optimization analysis. Just to confirm that the event angles were correctly calculated, the velocity functions of all axes were altered according to the reference instant – the beginning of the second axis acceleration – defined at 0,2s. Running a kinematic simulation with the above-described movement parameters, the following magnitude force and torque was obtained - Figure 3.33.
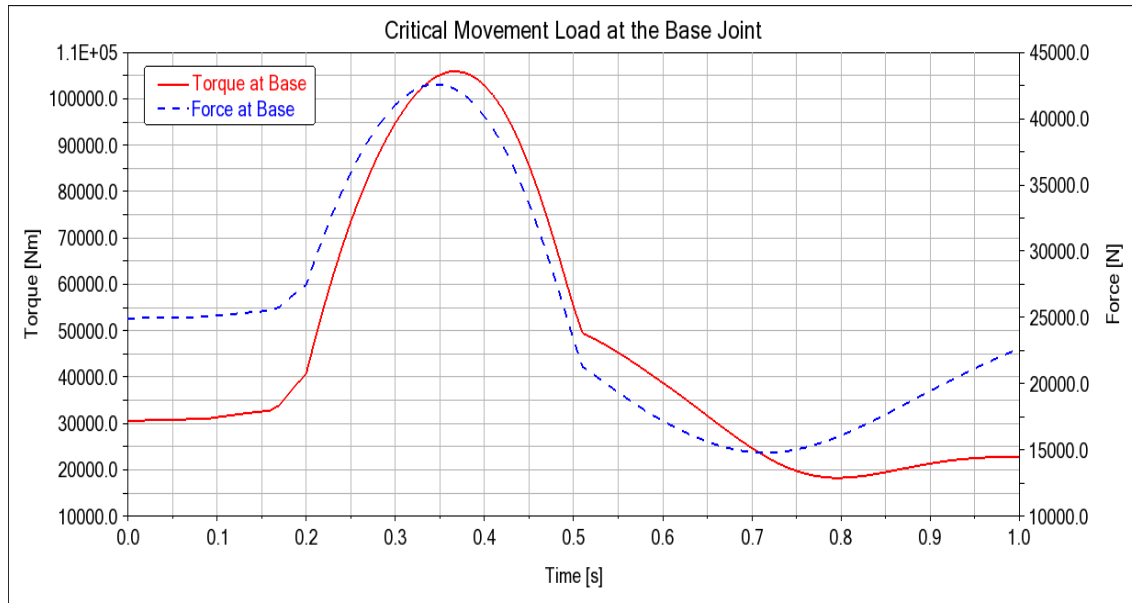
Figure 3.33 - Magnitude torque and force plots throughout the critical motion

This was the motion that generated the highest magnitude torque ever registered from all the performed simulations. To give a better idea of how it looks like, it can be described has starting with the robot fully loaded rotating around its first axis at maximum velocity with the other axes locked in a close to the fully extended arm configuration. At a certain point the first axis starts to brake in emergency, while immediately after the other axes are actuated to push the extended arm upward. It is very hard to conceive a practical function that would require such a motion. Even imagining the robot unloaded fully extended rotating at maximum velocity is already an extreme situation. It is then safe to assume this movement will never be willingly intended. Which in turn means that those load values will hardly ever be reached.

Even if flaws or mistakes were committed in this slow and conservative approach to obtain the highest torque movement, there are hard reasons to believe that the magnitude moments exerted on the supporting structure could be much greater than this.

3.5 Critical Motion Conclusions

Decomposing the maximum magnitude moment in its cartesian directions, the moments along x, y and z were 79'822 Nm, 12'693 Nm, and -68'465 Nm, respectively. For the force components it resulted: 16'218 N, -36'489 N, and 13'419 N, accordingly. However, it is important to mention that these are the values obtained at the exact instant in which the magnitude torque is the maximum. This does not mean that those are the highest possible load values on each direction.

In fact, it might also be important to know the maximum force and torque on each direction. For example, in this motion the maximum moment values along each direction - x, y and z - are 85'186Nm, 22'032Nm, and -74'687Nm, respectively. For the maximum reaction forces result 20'925N, -38'503N, and 13'609N. Although this was the movement found with the highest torque magnitude, certainly other motions can promote higher loads on one specific direction. This raises the question, if higher loads on a certain direction are worse for the structure integrity than loads with smaller values on all directions that together result in higher magnitudes.

In addition, there is a major concern with the results obtained, namely, their reliability. It is of the upmost importance to rephrase that a considerable number of robot characteristics had to be assumed or simplified to build the numerical model. Some variables were even chosen relying only on pure intuition. Thus, the simulated mechanism was certainly not close enough to the physical robot. This means, that the previously obtained results could be completely deviated from the physical problem.

Indeed, a few weeks after this whole motion analysis was finished the robot supplier shared a handbook with technical specifications of the COMAU NJ390-3.0. In it the company proposes different installation solutions for fixing the industrial robot, and also indicates the stresses that a structure supporting the machine should handle for the acceleration and emergency braking scenarios (COMAU S.p.A. 2018). In the following table are compared the loading values given from COMAU with the corresponding ADAMS results.

Table 3.14 - Comparison of the maximum loads obtained from the robot model and COMAU values. Numerical results are the highest registered during all critical motion

MOTION TYPE	VERTICAL FORCE (kN)	TRANSVERSE FORCE (kN)	TORSION MOMENT (kNm)	TILT MOMENT (kNm)
ACCELERATING (COMAU)	25,0	9,0	11,3	39,0
EMERGENCY BRAKING (COMAU)	29,0	17,0	22,6	6,1
NUMERICAL RESULTS (ADAMS)	38,5	23,0	22,0	105,2
RELATIVE DIFFERENCE	32,7%	35,3%	-2,6%	169,7%

The first aspect to mention, is that the results presented in the ADAMS row only refer to the maximum values developed in the obtained critical motion. If the approach taken had been

different - focusing instead on obtaining the 4 different movements that promoted the highest values for these 4 load categories -, the results would certainly be higher than the ones here presented. Although such analyses were not performed, the numerical values for torsion and tilt moments, could not be far from their actual maximum values since the method applied focused on obtaining the movement with the highest magnitude torque. In fact, the maximum tilt moment during the critical motion occurred at the exact instant when the magnitude moment is the highest.

Table 3.14 also shows that the values for the forces and torsion moment are not completely far from the numerical results. The torsion moment values – which depend exclusively on the first axis motion – are very similar, suggesting that the deacceleration utilized in this axis is close to the real emergency braking. However, the tilt moment difference is a big concern.

The given value by the robot supplier is almost 3 times smaller than the one registered on the motion simulations. One reason for this large disparity maybe be related with the fact that the accelerations used to actuate the revolute joints in the model had the same values of the emergency braking situations taken from the SIEMENS report. In addition, a physical emergency brake should be performed in all axes and not only in some, like in the critical movement found in this study. Nevertheless, the combined motions with braking at the first three axes also had very high numerical results for the magnitude moment. This implies that the components' masses of the virtual model were poorly attributed.

The only way to solve this, is to approximate the virtual robot characteristics to the physical machine. Unfortunately, the robot manufacturers rarely provide the dynamic parameters of their products (Wu et al. 2012). Therefore, it is up to the client user to identify those motion characteristics. Luckily, this field of studies has gained increasing attention and there are now many identification methods available (Jin and Gans 2015). They usually rely on creating a kinematic model of the robot, then control the movement of the physical robot through a prescribed trajectory while sensors take data measurements. This data must then be analyzed and through the identification method chosen the parameters of the robot can be estimated based upon the kinematic model.

The physical robot only arrived at the institute at a late stage of this project, making it impossible to realize these parameter identification procedures. It is here suggested to the investigators of the WBK researchers to invest in these identification methods to improve the robot virtual model, increasing the reliability of the subsequent simulations performed with the new robot characteristics. From the experience gained of this work, the author of this text points the following as being the most important characteristics to identify in order to properly approximate the virtual model to its physical counterpart: component's masses, velocity profile (or maximum accelerations) for braking and acceleration motions, and spring stiffness for the study of the second and third axes joints. If those parameters can be properly approximated, then the robot virtual model will become a reliable tool to help the investigators by rapidly presenting solutions for different answers and situations.

4   Dimensioning Process

Having numerically found the critical motion and associated loads that the COMAU NJ290-3.0 industrial robot can exert on a system supporting it, it was possible to start the dimensioning process of the modular structure. It was not necessary to idealize the functionalities needed for this construction, because its design concept had been previously developed by another student (Alznauer 2021). The work realized by this student was focused on conceiving the needs that an industrial robot has in order to perform the objectives set for the Wertstromkinematik (WSK) project. In his work the key aspects this modular structure should fulfill are mentioned, and solutions are suggested for some of those features. In spite of that, the solutions proposed are centered on achieving the concepts formulated by evaluating the expenses of such a solution with its advantages. A lot of room was left to allow changes. Consequently, this previous work was used for gathering information about the overall tasks this structure should perform and served as a starting point for the dimensioning process.

Before going forward, it is imperative to mention that the work from now on described was solely focused on answering the structural needs of the base support, while trying not to compromise its other functionalities.

The modular structure proposed by the previous student can be divided in two main groups of components: the functionality components and the structural components. On the functionality side, the control and supply units for the proper functioning of the structure are comprised, including the interface elements that allow the connection of the robot information and power cables with the supply grid. On the structural aspect, the parts composing the support frame are accounted, including a horizontal plate and also the clamping systems. For this dimensioning work only the structural components were considered. Figure 4.1 shows a virtual assembly of this modular structure.
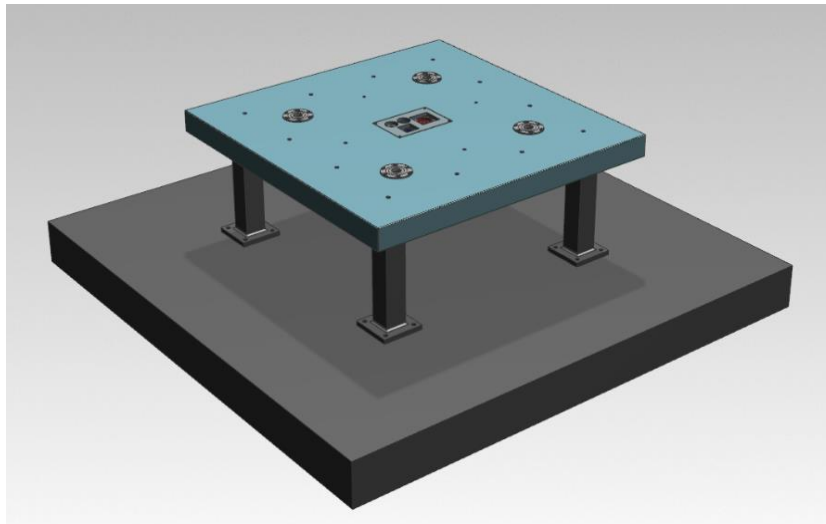
Figure 4.1 - Design concept proposed for the modular structure by (Alznauer 2021)

The support frame is composed by four feet fixed to ground, four legs that elevate the structure to allow the distribution of the power grid from underneath, and four bars creating a square metallic frame that connects the four legs. Attached to this square frame is a horizontal plate that supports all the functionality components referred above. This plate will act as the

"fake ground" that covers all the area assigned for the manufacturing processes with the WSK units. The clamping modules responsible for connecting the robot in a way that achieves the "Plug-and-Produce" concept are also fixed to this plate.

From a perspective of load transmission, the industrial robot will be connected to the clamping modules passing onto them the stresses generated during its operation. These in turn, will transmit the load to the horizontal plate that consequently is fixed to the ground through the supporting frame. The objective of this dimensioning work is to make sure the structure is capable of sustaining the exerted load under the performance criteria set by the project functions.

4.1   Dimensioning Approach

The most important structural function this modular construction has to assure is a low deformation during robot operation in order to introduce as less deviations as possible on the machine tool center point (TCP). The precision of the industrial robot should be the least affected by displacements on its base structure. Besides this major characteristic, there are other vital aspects that such a support system should uphold. It must not under any circumstance reach mechanical failure. The vibrations transmitted from the operating process or from other nearby machines should also be accounted and dampened not to influence the robot performance. Finally, in addition to support the industrial machine, the structure must be prepared to sustain the weight of other components that might be positioned next to the robot to assist the manufacturing tasks. Naturally, all of this should be achieved with the least expenses. The material and manufacturing costs of this structure should be kept as low as possible. Although all of these questions have to be addressed to properly assure the structure functionality, the only aspects evaluated in this dimensioning process were the displacements at the regions where the robot will be attached, and the stresses developing on the base construction.

To do so, a methodic approach with increasing complexity and detail was performed to analyze the stresses and displacements occurring on the structural components of the modular base. This structural analysis was executed recurring to ABAQUS® - a CAE program based on finite element method. An initial, simple model of the structure based on the above shown Figure 4.1 was drawn on a CAD program and then imported to Abaqus to simulate its response under the load exerted from the robot. This structure model was then successively updated to include more components, better representing the future, physical construction, and the load transmission between the different parts.

At this point, it is important to mention that the load used in the structural analysis was the numerically calculated load in ADAMS and not the values provided by COMAU in their technical specifications. The main reason was to maintain the workflow planned at the beginning of this thesis. This would allow a future student or investigator to quickly replicate and improve the executed dimensioning steps when more realistic robot parameters - and as a consequence, more realistic load results - are obtained. In addition, using the numerical results would allow to evaluate the structure behavior for the whole critical movement, instead of loading the structure with a single value for each cartesian direction. This would help to perceive the influence of other possibly important loading scenarios besides the exact instant with the highest sum of moments. Therefore, it was decided to import the numerical results at

all time steps of the critical movement into the FEA program. However, there is the downside of prolonging the simulation times in order to solve the numerical problem at each one of the time steps.

Before entering the description of the dimensioning process, the design objective has first to be properly defined. As already mentioned, the major goal was to have the smallest displacement possible. This is a clear objective, but it would be helpful to have a defined value to aim at. For example, a maximum displacement that the structure must not surpass. Due to the early stage of the WSK project, there was no such data for the maximum allowable displacement nor any other related measures. Hence, this work was focused on the reduction of this variable as much as possible, instead of aiming at a certain value. This means, the successive design iterations were made to constantly decrease the structure displacements, without considering how those values would actually influence the TCP positioning.

However, for the allowable stress values, to make sure no region of the support will enter the plastic deformation regime, a safety factor was applied to the yield stress of the chosen material. From the literature previously exposed, a proper safety factor for a situation like this would vary between 1 and 3 (Chang 2015). The materials used are known and reliable – this will be addressed later -, but the loading conditions are not entirely certain. The only forces applied come from the robot and the structural components' weight, not considering other external elements that might be deployed on top of the structure or may be attached to the lower part of the horizontal plate, for example. However, since the load utilized on the structural analyses are already higher than ones indicated by the robot supplier, a safety factor of 1,7 was selected. It is here suggested to reevaluate this safety value when the robot mathematical model is updated with closer parameter characterization.

The dimensioning process applied was divided in four main steps. Each of these aimed to answer specific questions about the structure and on each one of them, the complexity and reliability of the model increased.

- ➔ In the first step, a very simple geometry was modeled and subjected to the robot load. The goal was to have a solid starting point from which to develop the remainder of the structure with more detail. At the same time, this simple model was also used to test different capabilities of the CAE program and decide which were the best parameters to employ in this type of problem.
- ➔ In the next step, the dimensions of the simple geometry were altered to test different structural responses. This step was intended to perceive the influence of certain characteristic lengths on the stresses and displacements registered during the simulation. In the end, the position and height of the legs, and the thickness of the horizontal plate were defined.
- ➔ In the third step new elements were added to the model. The clamping modules attached at the horizontal plate, the clamping pins, and a new part responsible for connecting the robot to the clamping modules. This step was centered around the clamping modules configuration to make sure they would not reach their maximum load capacity. The number, position and their installation type were defined in this step.
- ➔ In the last step, different solutions were tested to try achieving better results regarding the stresses and displacements generated on the structure. These proposed solutions were compared, and conclusions from their application were drawn considering the associated advantages and drawbacks. In the end, a structure with defined dimensions was selected along with relevant notes and suggested tasks to perform future phases of the WSK project.

In the following sections of this text the above exposed approach for the dimensioning of the modular construction is described. The objective of the next sections is not to fully detail the work that was performed, but more inform and explain about the decisions took on the numerical program parameters and especially expose the thinking process done when a certain design decision or assumption was made.

4.2   Simple Model Development

As previously referred, it is a good approach for any structural analysis to start with a simple model and then increase successively its complexity and reliability. That should be done until the structural engineer agrees that the virtual model conceived is a good enough representation of the physical case and the results are acceptable to be extrapolated to the physical world. Thus, it was decided to start by modeling a very simple geometry that would resemble the overall structure size.

For that reason, a single part based upon the dimensions defined by the previous student's work was modeled on a CAD program. This part resembled a table composed by a square $2x2m^2$ plate with 0,1m thickness on top of four legs with 0,5m height and $0,2x0,2m^2$ cross section area – Figure 4.2. This part file was then imported to Abaqus to prepare the simulation conditions.
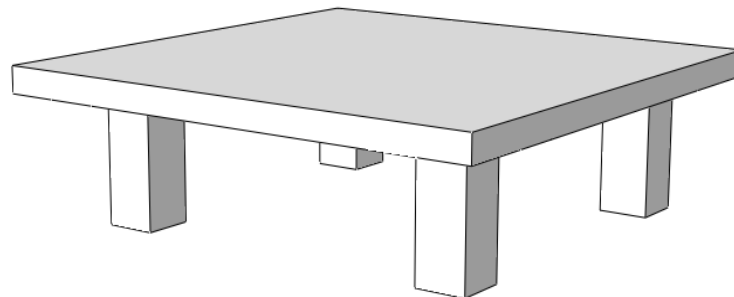
Figure 4.2 - Simple initial model

To start, it was necessary to attribute this geometry the necessary material properties to solve the problem. The purpose of this whole dimensioning process was to evaluate the stresses and displacements originated on the structure when only submitted to the robot load. Thereby, it was necessary to characterize the material stiffness and Poisson's ratio in order to relate the forces exerted with the nodes' displacements and internal stresses. The only other property that had to be defined was the material's density in order to apply the gravity force due to the component's own weight. No other material properties were necessary for this simulation. It was supposed to occur within the elastic regime at a constant temperature and environment conditions, therefore not requiring yield stress, expansion coefficient, electrical conductivity or other properties.

The material chosen for this structure was a typical low carbon steel. This choice was mostly based on its accessible price. This material does not require any other notable functions besides withstanding the loads transmitted from the production system. The weight of the structure is

irrelevant since it is fixed to the fabric ground floor. Atmospheric conditions should not be a concern due to the closed environment. Even if the yield stress was too low, it would only be a matter of increasing the size of the components on the critical regions. This holds true, as long as the added weight would not make it worthier to use another material. Nevertheless, it was considered that the best material for this task was simply the cheapest option available.

For simplicity's sake, it was assumed that the mechanical properties of the material were isotropic, thereby making it only necessary to define one stiffness value. In the next Table 4.1 are presented the values attributed to the simple structure model. The consistent set of units utilized was the kg/m/s, which gives the stresses results in Pascal and the displacements in meters.

Table 4.1 - Material properties attributed to the part

STIFFNESS (Pa)	POISSON'S RATIO	DENSITY (kg/m³)
210E+9	0,3	7800

Having the component's material properly defined, it was time to apply the loads to the part. For the boundary conditions, the bottom surface of the four feet - that are supposed to be fixed to the ground – were pinned to have their degrees of freedom totally constrained. In terms of the components' own weight, the gravity force was added applying to all regions of the model. The program would calculate the weight of the component based on the density value and the volume given by the part geometry. Finally, the robot load was introduced. However, this task was not straight forward, it required some modeling in Abaqus and further considerations.

The first matter was related with the load application. It was not possible to directly apply the load to the center of the horizontal plate, due to the components' geometry type. Instead, a fictional point had to be created to have the load exerted on it so that the load could later be distributed to the structure. These points are called Reference Points (RP) and the first question to answer was where it should be located. In ADAMS a fixed joint was employed to act as the support for the robot movements. This joint was located on a single point at the robot model origin and carried all the load exerted. Thus, the Reference Point in Abaqus was chosen to be on the corresponding location of the fixed joint at the robot model in ADAMS. This means, the RP was defined at the center of the upper surface of the horizontal plate.

Then, it was necessary to understand how this point distributed the load to the structure. That was made through a coupling constraint in Abaqus. In this case the created point, which was initially free to move under the load exerted, now had its degrees of freedom coupled to the degrees of freedom of all the nodes of the upper surface of the plate. With this the load exerted on the point could be transmitted to that surface. Yet, this connection was distributing the robot forces uniformly throughout the surface. This means the load was being equally divided for all the nodes, instead of concentrating it more on the center of the plate, where the robot is supposed to be attached. It was decided to leave this distribution uniform, because the model would later be improved to better represent this aspect.

The look of the CAE program viewport with the three different loads exerted on the part is depicted in the following Figure 4.3.
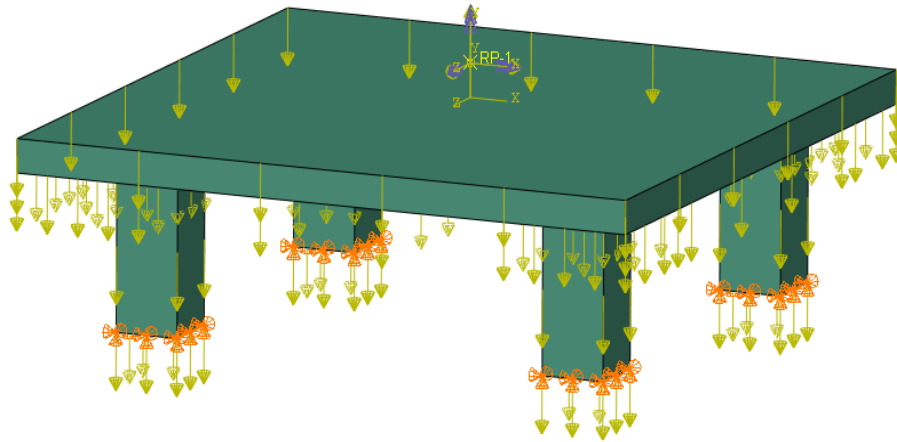
Figure 4.3 - Load applied at the structure model

Onto the next task of the model preparation for the structural analysis, it was necessary to select the intended type of simulation and the desired output variables.

As already mentioned, the purpose of this work is to only evaluate the structure capability to sustain the robot loads. There is no intention to study any other aspects besides the structural analysis of the base. For such cases, Abaqus has three different simulation options: Static General analysis, Dynamic Implicit analysis, or Dynamic Explicit analysis. Static analyses are intended for cases in which the inertia of the components is neglectable and time-dependent material effects (fatigue, creep, and so on) are not desired. Implicit Dynamic analyses are a good option for problems with low frequency response, vibrations, and oscillations. On the other hand, Explicit Dynamic is used for situations with impact, crash, drop, and other extremely discontinuous events (Dassault Systèmes 2020).

For this problem with the robot load the Static General analysis was chosen. The base construction is supposed to be static, have the least displacements as possible. Even if the load applied was not time constant, it is not abrupt to influence the inertia of the structure. There is no risk of evaluating this model recurring to static analysis because the frequency of the load is too low to cause large strain rates. Nevertheless, just to assure this question, an implicit dynamic analysis was later performed to prove that the kinetic energy of the system was practically neglectable for this problem.

Another important aspect for this simulation is to leave the Non-Linear geometric (NLgeom) option OFF. In situations where large strains are expected, non-linear geometric effects become important, and this option should be turned on to help the program solver. Otherwise, when it is sure no large strains will occur, then it is best to leave this option off, since it can largely increase the computational costs.

Regarding the output variables, the displacements and internal stresses occurring at the structure were undoubtedly selected. For the displacements Abaqus provides results of this measure in each of the global coordinate system directions and also the equivalent magnitude. Regarding the internal stresses, the results can present the different elements' stresses along the global directions and there are also many criterions available. For this simulation, the

stresses on the structure were evaluated by the von Mises Equivalent Stress. For the resolution of the outputs, it was chosen to have the results shown for all time steps of the simulation in order to observe the structure response for all the critical movement.

At last, the model had to be discretized in a finite number of elements. For this simple geometry it was possible to use only hexahedral shape elements as there were no complex features or sharp edges. That was a good option because this element shape gives good results for three-dimensional analysis without requiring large computational resources. For the type of element, it was decided to simulate the construction with different options and compare their performance. The selected elements were the C3D8 (first-order elements), C3D8R (first-order with reduced integration), and C3D20 (second-order elements). The first-order reduced integration elements were the default option at Abaqus, but even though they produce faster simulations, the full integration elements are more appropriate for low bending situations and detecting local stress concentrations. The quadratic element was also tested to check if the first-order element was not presenting shear locking phenomenon, deforming less than it should.

4.2.1   Mesh Element Type Comparison

For the comparison of the different element types, multiple simulations with increasing mesh density were performed for each element in order to achieve convergence on the numerical results. The objective was to sequentially refine the mesh until a variation of under 2% on the maximum displacements between iterations would be achieved. Although the displacements results converged rapidly, it was soon noticed the existence of a singularity at one leg's corner in contact with the bottom surface of the horizontal plate. This was proved when the progressively denser mesh on the leg's region generated successively higher stresses - Figure 4.4.
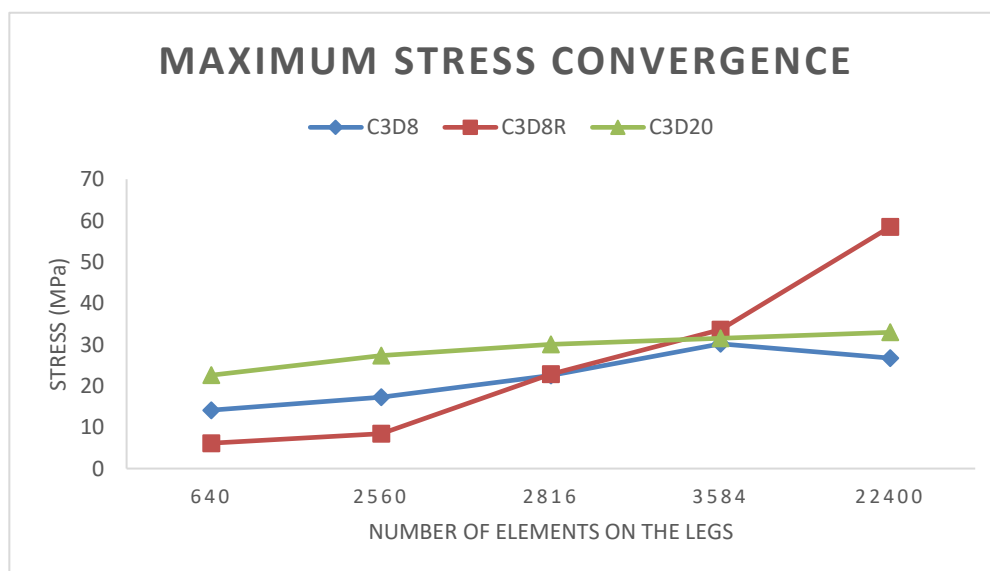
Figure 4.4 - Maximum Stress Convergence with different finite element type

---

As it can be observed, for all elements the stresses tend to be increasing with a finer mesh. Even the quadratic element which is the best option for capturing stress concentration points revealed this singularity behavior. The decrease on stresses between the last two iterations of the C3D8 element happened, because the finer mesh at the legs also affected the elements' size and number on the horizontal plate. It was noticed that if the size of the elements on the plate was close to the size of the elements on the legs, then the maximum stress value would slightly decrease. Otherwise, it would keep rising. To prove this circumstance, the model with C3D8 had its elements' size on all the component reduced to half. Then with successive simulations only refining the mesh on the legs, it was verified that the stress value raised again – even more rapidly than before with a coarser mesh on the plate. This confirmed there was a singularity.

For the max displacement registered on the structure, the convergence occurred easily with a couple of iterations. The point where that displacement occurred was in the middle of one edge of the horizontal plate. The convergence process is presented in Figure 4.5.
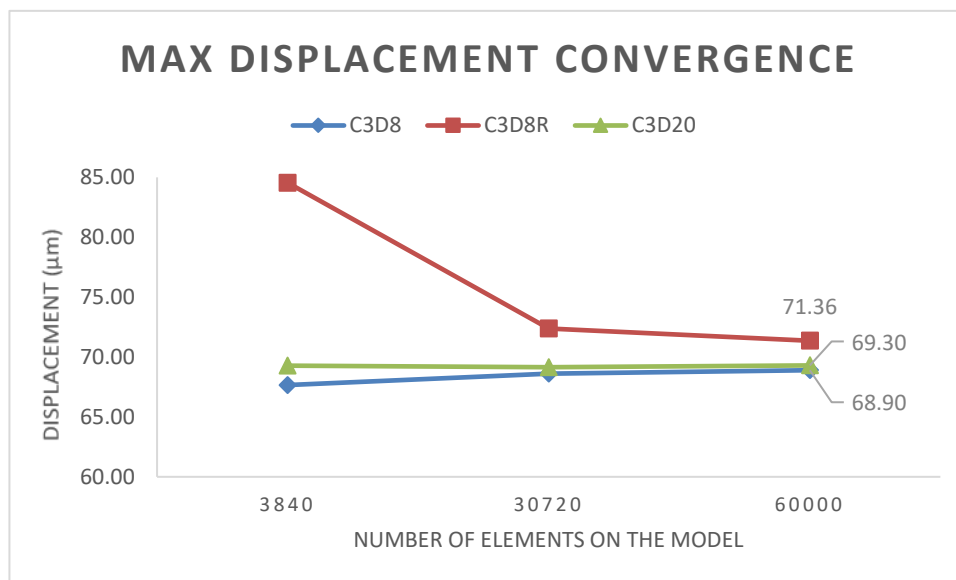
Figure 4.5 - Maximum Displacement convergence for different finite element types

The first thing to note is that both full integration elements had no significant variation with finer mesh. Their initial values were already close to the final ones obtained. On the other hand, the reduced integration element needed a much denser mesh to converge the maximum displacement result. Then, it can be seen that the final results for the three elements are relatively close. This suggests that it would be acceptable to choose any of the elements to use in the next steps of the work. However, the quadratic element requires a great amount of computer power. Its simulations were 4 times longer than the C3D8. Also, the reduced integration element needed far more elements to converge to a solution and this could lead to longer simulations on more complex models. Consequently, the first-order full integration element was selected. It had already close displacement values since the first iteration and the fact that the final results are similar to the C3D20 proves it was not being affected by shear locking effects.

This completed the objectives for the first step of the dimensioning process. A simple model submitted to the robot operating loads was successfully simulated and the simulation parameters were defined for the next stages of the work.

4.3   Simple Model Dimensions

The second step was intended to approximate the dimensions of the simple model to a more feasible solution. From the numerical results of the previous step – specially the low stresses -, it was considered that the structure was over-dimensioned. While it is true that the weight of the components is not a concern, larger dimensions entail higher material costs due to the added mass. As a consequence, it was decided to reduce some dimensions of the system, while at the same time, trying not to raise the numerical results dramatically. Thus, this second step was divided in two parts. First, different models were created varying only one dimension to understand its influence on the structural response of the structure. Then, models with different dimension configurations were experimented based on the previous knowledge gained in order to select one of those option for the next phases of this work.

The studied dimensions were the horizontal plate thickness, the legs area, the position of the legs, and the legs height. These dimensions were studied separately in relation to the model in the first step. For the horizontal plate, the original model had a thickness of 100mm and thus one model with 75mm and another with 50mm were simulated. Regarding the area of the legs, for its simplicity was chosen to only consider square cross-sections. The first step model had legs with 200x200mm² area, then other two models with 150x150mm² and 100x100mm² were created. In respect of the legs' position, this characteristic had a constraint, which obligated the structure to have at minimum of 1m space between them to allow the underneath cables and power distribution to pass. The first step model had the legs 1,2m apart, then a configuration with 1,1m and another with 1m were studied. Lastly, the legs' height. This dimension also had a constraint due to the same exact reasons. In this case, the horizontal plate should be at a minimum of 400m height off the ground. In the original model the legs had 500mm height, thus heights of 450mm and 400mm were created. In Figure 4.6 are shown the numerical results for each one of these different geometry variations. Note that, although there are only 3 models on the horizontal axis, in reality 8 different configurations were analyzed.

As expected, the reduction in the horizontal plate thickness and the leg's area raised the displacement results. However, the rapid increase from 75mm to 50mm shows how important this parameter is. Knowing that this dimension also greatly influences the mass of the structure, a deep evaluation on the expenses in comparison with the allowable displacement should later be performed. For the legs' height, unsurprisingly, the best option is the smallest - 400mm. Concerning the positioning of the legs, the results are interesting because there is a slight displacement increase between the 1,1m and 1m distances. This happened because of the uniformly distributed load on the upper surface, causing the outer edges of the plate to have larger strains. Due to this situation a new model with 1,05m distance between the structure legs was simulated. Its maximum displacement was 46,62μm, the lowest result of the 4 models. Therefore, a leg distance of 1,05m was selected for the next phases of the work.
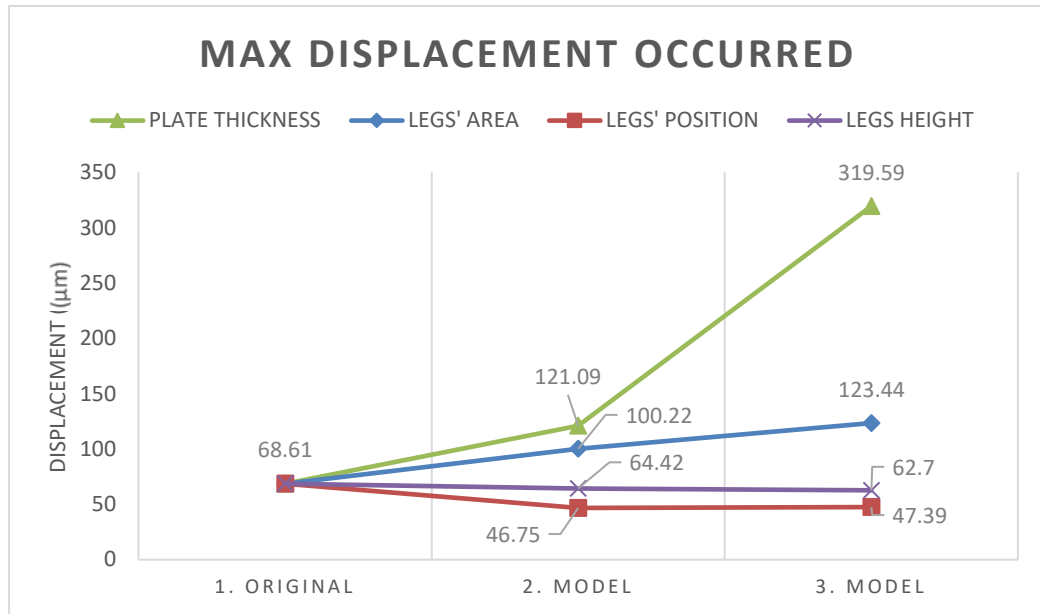
Figure 4.6 - Maximum displacement occurring at different model variations

With this, it was only necessary to define the plate thickness and the area of the legs. To do so, three structures with the following characteristics were modeled:

➢ 1. Model: Plate thickness = 75mm, Leg Area = 150x150mm²
➢ 2. Model: Plate thickness = 62,5mm, Leg Area = 150x150mm²
➢ 3. Model: Plate thickness = 50mm, Leg Area = 150x150mm²
➢ 4. Model: Plate thickness = 75mm, Leg Area = 125x125mm²
➢ 5. Model: Plate thickness = 62,5mm, Leg Area = 125x125mm²
➢ 6. Model: Plate thickness = 75mm, Leg Area = 100x100mm²

Since the numerical results did not increase too much from the first step model to the 75mm thickness plate model or to the 150x150mm² area model, there was no need to try configurations with bigger dimensions than those. The other configurations were created to have more structure samples. One interesting fact that occurred in the models with legs' area of 125mm or 100mm square side, was a shift from the highest displacement point. On those configurations it was at one of the horizontal plate corners, instead of occurring in the usual location in the middle of an edge. This happened because the plate area outside the legs increased, by reducing its cross-section. In Table 4.2 are presented the simulation results of these models and their mass reduction in comparison to the original model.

The table shows once again the high influence of the plate thickness on the maximum displacements. The third model has less than half of the mass of the original construction, but the strains are much higher than in any another configuration. The table also depicts that the first model is by far the one with the best displacement increase per mass reduced ratio. However, this is also the most conservative solution. Despite not being presented in the table, the maximum internal stresses were not high enough to reach problematic values in any of the proposed models. Even the nodes in the neighbor area of the singularity point presented relatively low stress values.

Table 4.2 - Numerical results obtained for the 6 models

NUMERICAL RESULTS	STEP 1	1	2	3	4	5	6
MAX DISPLACEMENT (µm)	68,61	108,1	160,1	277,6	142,3	215,2	190,1
STRUCTURE MASS (kg)	3744	2620,8	2230,8	1840,8	2535	2145	2464,8
DISPLACEMENT INCREASE	---	39,46	91,49	209,0	73,7	146,6	121,5
MASS REDUCTION	---	30,0%	40,4%	50,8%	32,3%	42,7%	34,2%
SENSITIVITY (µm/kg)	---	0,0351	0,0605	0,1098	0,0609	0,0916	0,0950

At this point, it is important to rewind and think about the purpose of this dimensioning step. The intention here was to approximate the model from the first step to a more practical solution. The dimensions here chosen for the next steps of the work, could be later altered when a much more reliable structure model is conceived. In fact, this was exactly done. In the last step of the dimensioning process, a similar step as this one here presented was again executed.

Knowing that these dimensions' changes could later be reverted and being conscious that the displacements obtained in this step were unreliable, due to the uniform load distribution on top of the structure, it was decided to opt for the optimist solution. The structure with 50mm plate thickness and 150x150mm² leg cross-section area. This was the lowest mass configuration, and so the next steps of the dimensioning work were performed to try improving its load response.

4.4 Structural Model Upgrade

The purpose of this phase of the dimensioning work was to approximate the simple geometry model to a virtual construction closer to the future physical structure. That was achieved by introducing new elements that could better represent the load transmission between the different components of the modular support. Those newly added components were intended to replicate the clamping modules' load distribution. To do so, three different components were created. A part representing the clamping module, another part reproducing the clamping pin assembly and a new horizontal plate part.

The clamping modules chosen for the WSK project are supplied by SCHUNK, a German company leader in clamping technology and gripping systems. These components are usually employed to rapidly secure pallets for high-precision manufacturing processes. They possess a cylindrical shape with a central hole for the clamping pin - Figure 4.7. The clamping pins are attached to a pallet by a screw connection. These pins are introduced in the clamping module hole and then locked through an internal mechanism that is actuated by compressed air. Once the manufacturing operation is complete, the clamping module is again pneumatically actuated to open and free the pin. This is a fast and precise coupling procedure which reduces machine set up times and secures the pallet positioning accuracy.

Figure 4.7 - Example of a SCHUNK clamping module and clamping pin (SCHUNK GmbH & Co. 2021)

In this work, the clamping modules will be mounted on the upper surface of the horizontal plate for fixing the robot during its operation. However, the clamping pins cannot be directly attached to the robot. The COMAU machine is laid on top of a support component contacting with this surface by four feet. These feet also possess holes to additionally attach the robot by screw connections to the underneath support. Unfortunately, these holes cannot be used for the clamping pins for three major reasons. Firstly, the diameter of the robot feet holes is larger than the screws used to mount the clamping pins on the pallets. Secondly, the holes of the robot feet are too close together, which does not allow the use of all holes for the clamping pins. Thirdly, if the pins were directly mounted on the robot feet it would restrain the possible orientations to place the industrial machine.

Since one of the main objectives of the WSK project is to offer flexibility in production plants, it was here decided that the robot should have the possibility to be coupled on four different orientations at the same modular structure. To fulfill this requirement the positioning of the clamping modules must be bisymmetrical in relation to the center point of the structure plate. The best way to achieve such a connection between the production unit and the base support is to add a new plate that acts as an interface between the robot and the clamping modules. This plate would be mounted to the robot by the screw connections at the industrial machine feet and on the other surface it would have the clamping pins attached by different diameter screws. Additionally, with this new component there is more freedom to select the number and position of the clamping modules to achieve a better solution. Not to mistake this plate with the structure plate, this new part is from here on referred as "robot plate".

The work done in this step was to make sure the added components were properly modeled to transmit the machine loads in a close behavior to a future physical construction. Hence, this third step was carried out in the following task order.

1. Elaborate the robot plate.
2. Formulate different clamping module configuration options.
3. Study the clamping pins assembly.
4. Introduce the new elements in Abaqus and test their connection properties.
5. Improve the model fidelity at the robot feet interaction.
6. Test the proposed clamping module configurations.

7. Select the best solution.

In the following sections of this paper the work done in each of these tasks is presented.

4.4.1 Robot Plate Design

The robot plate will be responsible for connecting the robot to the modular structure. The load exerted from the machine operation will be transmitted to the plate passing it then onto the clamping modules. As a consequence, this component should be strong enough not to fail at any of these connection points. Since there was information available on that regard, the initial dimensions for this robot plate were based on an existent solution proposed by the robot manufacture.
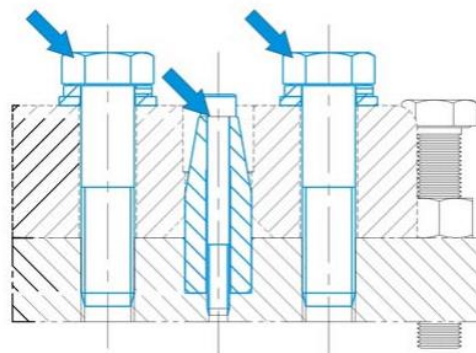
Figure 4.8 - COMAU NJ390-3.0 fixture elements (COMAU S.p.A. 2018)

In the COMAU technical specifications handbook are suggested different solutions to install the machine to the ground. One of those is based on fixing all the feet of the robot to a single steel plate and then secure this plate to the ground. This plate has an area of 1,2x1m^2 and 40mm thickness. It is connected to the robot by six partially threaded hex head screw 24x100 (8.8) and two couples of hollow centering pins crossed by socket hex head screws M10 (8.8) - Figure 4.8. This plate is laid on the ground, but between both surfaces should be employed a self-leveling mortar layer to flat and smooth the fabric floor. The connection of the plate to the ground is then accomplished by 16 chemical sleeve anchors with M24x170 screws around the edges of the plate. In Figure 4.9 is presented a sketch of the plate with all its holes and the robot feet area.

This installation solution proposed by the robot manufacturer is different than the one on this work mostly because the robot plate will not be entirely laid on another surface. Instead, it will be connected to the clamping modules that elevate it a few millimeters above the structure's upper surface. This situation will be explained in detail in the next section. Basically, for this project the robot plate will only be supported on the clamping modules. Outside those regions the plate will be simply suspended, susceptible to bending. This means, the internal stresses on this plate will certainly be higher than the ones on the COMAU solution. Nevertheless, this was a good starting point for the robot plate. By using a steel part with equal dimensions, the connection to the robot feet by the screws are assured, since it was exactly the same as the robot manufacturer suggests. If the internal stresses on the FEM numerical

results are too high, then it would be necessary to reinforce this plate. In that case, the obvious choice would be to increase its thickness. For those reasons, it was decided to start with a robot plate with the same dimensions of the plate used by COMAU in their installation solution.
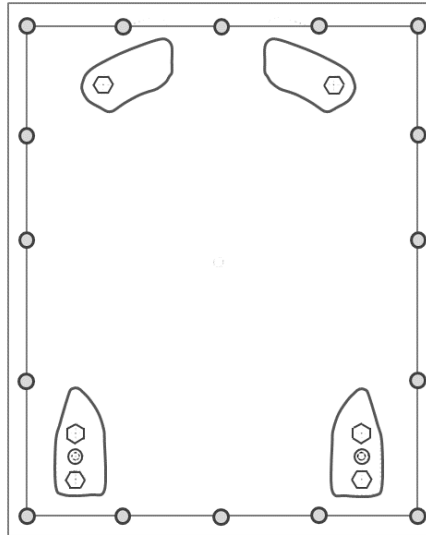
Figure 4.9 - Sketch of the installation plate (COMAU S.p.A. 2018)

4.4.2   Clamping Configurations

As was mentioned above, the clamping modules are responsible for holding the robot plate - and consequently the machine unit - in place during its operation. Thus, it is important to assure these components can safely withstand the loads generated. From the multibody analysis in ADAMS, the load exerted on a supporting structure at the instant with maximum magnitude moments is presented in Figure 4.10.
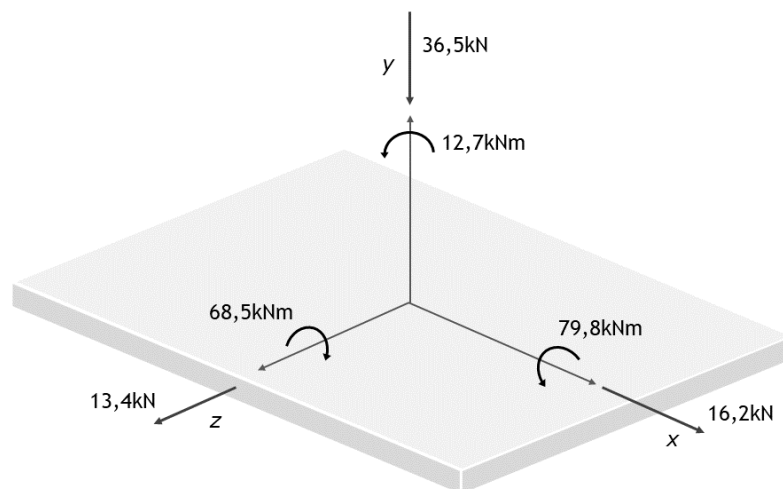
Figure 4.10 - Critical load taken from the motion analysis numerical results

However, it is important to recall that these are not the highest values along each of the degrees of freedom of the base joint evaluated in the motion analyses. As was previously exposed, for the critical motion obtained there are other time steps when the loads are higher at a certain direction. For each of the six DOF those results were:

- Vertical Force = -38,5kN
- Lateral Force X = 20,9kN
- Lateral Force Z = 13,6kN

- Torsion Moment = 22,0kNm
- Tilt Moment X = 85,2kNm
- Tilt Moment Z = -74,7kNm

As the approach taken in the motion analysis was solely focused on the maximum magnitude torque, the previous loads presented could become even higher if separated studies were made to obtain the movements that generated their maximum values. However, those studies were not performed. Thus, it was considered that the maximum force and moment values along each direction could not be much higher than the ones obtained in during the critical motion. In other words, the motion obtained with the maximum magnitude torques was assumed to possess the highest load scenarios along each degree of freedom of the base joint.

In order to sustain the forces and moments presented, it was necessary to develop a clamping configuration that could handle those loads. To do so, a few questions had to be answered. Which type of clamping modules should be utilized? How many are needed? And where should they be positioned? Although these are different questions, they are interrelated. Therefore, it was decided to formulate different feasible clamping configurations varying in model, number, and positioning and later test the structure behavior with those proposed solutions.

To reduce the number of formulations, were only considered the two types of clamping modules with the highest force and torque resistance. From SCHUNK catalogues the NSE-plus-176 and the NSE3-136 clamping modules with turbo function were taken (SCHUNK GmbH & Co.). In Table 4.3 are presented the maximum load values one of these components can withstand.

Table 4.3 - Maximum supported load for both clamping modules (SCHUNK GmbH & Co.)

LOAD TYPE	NSE3 138	NSE PLUS 176
VERTICAL PULL FORCE (kN)	28	40
VERTICAL PUSH FORCE (kN)	40	35
LATERAL FORCE (kN)	2,8	4
TORSION MOMENT (Nm)	190	350
TILT MOMENT (Nm)	500	350

As it can be seen the lateral forces and tilt moments are only given for one direction. Therefore, the maximum equivalent lateral force and tilt moment during the critical motion were taken:

- Maximum Equivalent Lateral Force = 23,1kN
- Maximum Equivalent Tilt Moment = 105,2kNm

From the values shown in the table it is clear that a large number of clamping modules would be necessary. To have more information on this regard, the SCHUNK technical support was contacted to share the maximum load values of clamping systems with a higher number of modules. In return, three different clamping configurations along with their maximum allowable forces were provided - Table 4.4.

Table 4.4 - Maximum supported load by different clamping configurations

LOAD TYPE	4X3 270X270MM PITCH (NSE plus 176)	4X3 300X300MM PITCH (NSE plus 176)	5X4 200X200MM PITCH (NSE3 138)
LATERAL FORCE	48kN	48kN	56kN
TORSION MOMENT	16,5kNm	18,5kNm	18kNm
TILT MOMENT X	89kNm	98kNm	95kNm
TILT MOMENT Z	69kNm	76kNm	77,7kNm

None of these configurations could be directly employed for the structure. Although they sustain the loading at the time instant correspondent to the maximum torque magnitude, they fail to withstand the maximum torsion moment of 22,0kNm. These clamping configurations can easily sustain the vertical and lateral forces, and tilt moments, but not the torsion. This implies that the torsion generated by the robot model might be the actual critical load for the clamping system. Therefore, it would be a good option to perform another motion analysis to obtain the maximum torsion the production unit can generate at its base support.

In addition to not sustaining that load, the clamping modules did not respect other design constraints of the structure. Such constrains are:

- Be bisymmetrical to allow the positioning of the robot on 4 different perpendicular orientations.
- Leave the center of the plate unoccupied to let the supply and information cables to the robot go through.
- No be directly positioned under the robot holes to allow space for longer screws and nuts under the robot plate.

Although none of the clamping systems shared by SCHUNK could be employed, these were a valuable piece of information. Knowing the maximum loads supported by those configurations, it was possible to formulate new clamping configurations that respected the design constraints and then compare them with the SCHUNK solutions. This comparison was based on empirical equations and safety factors.

4.4.2.1 Clamping Equations
In respect to the vertical force, the maximum allowable value for a group of clamping modules will be equal to their individual maximum axial force multiplied by the n number of clamping points.

$$F_{plate,vertical}^{max} \leq F_{module,vertical} \times n$$

The same succeeds for the lateral force components. In this case, the equivalent lateral force should be smaller than the maximum lateral force of each module multiplied by its number.

$$F_{plate,lateral}^{max} \leq F_{module,lateral} \times n$$

For the calculation of the maximum allowable torsion moment in a group of clamping modules, the following assumption was done. A pallet supported by a n number of clamping modules, will reach its torsion failure when all the points are subjected to their maximum lateral force on the perpendicular direction of the torsion applied point. This is shown schematically by Figure 4.11.
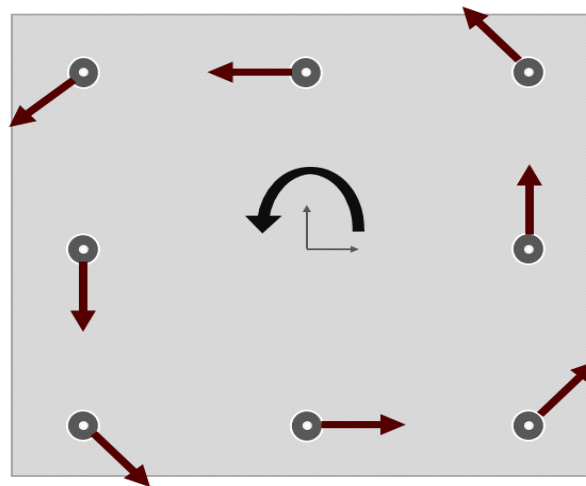
Figure 4.11 - Maximum Torsion Moment calculation scheme

With such an assumption the equation for the maximum allowable torsion exerted on one specific point for a pallet would be:

$$M_{plate,torsion}^{max} \leq \sum_{1}^{n} d * F_{module,lateral}$$

where d is the distance from the load point to the clamping module position.

For the tilting moments, a similar elaboration was done. The clamping system would reach its maximum tilt moment value when the clamping modules exceeded their maximum allowable vertical forces. Next Figure 4.12 exemplifies this clearly.
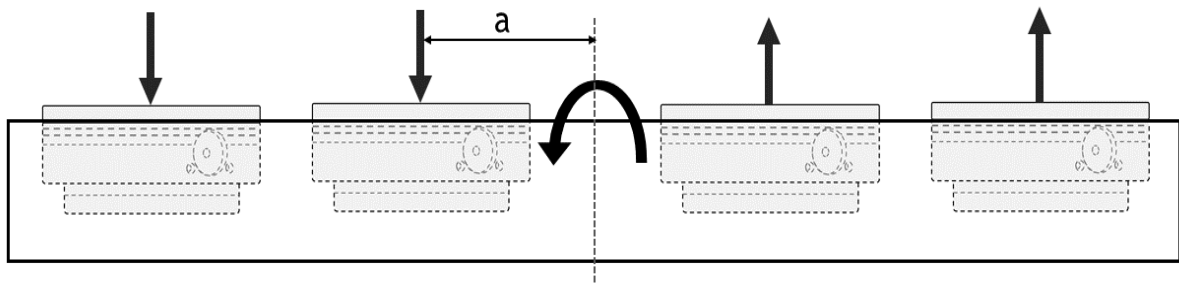
Figure 4.12 - Maximum Tilt Moment calculation scheme

Thus, the equation for the allowable tilt moment becomes:

$$M_{plate,tilt}^{max} \leq \sum_{1}^{n} a * F_{module,vertical}$$

where a is the normal distance between the tilt moment axis and the clamping point.

Indeed, these last two equations do not reflect the load response of the clamping modules. In the tilting moment, the components will not be only submitted to axial forces, there will always be a component of tilting on the own module. To assess if these equations can be reliable to predict the maximum allowable loads for a new clamping configuration, these equations were applied to the examples given by SCHUNK.

Table 4.5 - Comparison of the formulated equations results with the first configuration maximum loads

NSE PLUS 176 - 270X270 PITCH – 4X3 CONFIGURATION			
LOAD	SCHUNK	Equations	Ratio
TORSION MOMENT (kNm)	16,5	16,9	0,974
TILT MOMENT X (kNm)	69,0	75,6	0,913
TILT MOMENT Z (kNm)	89,0	113,4	0,785

Table 4.6 - Comparison of the formulated equations results with the second configuration maximum loads

NSE PLUS 176 - 300X300 PITCH – 4X3 CONFIGURATION			
LOAD	SCHUNK	Equations	Ratio
TORSION MOMENT (kNm)	18,5	18,8	0,983
TILT MOMENT X (kNm)	76,0	84,0	0,905
TILT MOMENT Z (kNm)	98,0	126,0	0,778

Table 4.7 - Comparison of the formulated equations results with the third configuration maximum loads

NSE3 138 - 200X200 PITCH – 5X4 CONFIGURATION			
LOAD	SCHUNK	Equations	Ratio
TORSION MOMENT (kNm)	18,0	19,0	0,947
TILT MOMENT X (kNm)	77,7	112,0	0,694
TILT MOMENT Z (kNm)	95,0	134,4	0,707

From the above tables it can be seen that the torsion moments' results from the equations are only slightly higher, but the tilt moment especially in Z have a considerable difference. Interestingly the tilt moments have different ratios depending on the direction. This suggests that the tilt equation is not entirely reliable since the relation between the real values and the empirical ones is dependent on the configuration utilized. This is demonstrated by the low ratio of tilt moments on X in the third configuration, while the first two cases have high values.

4.4.2.2 Proposed Configurations

However, there was no other way to validate any prior configurations. The objective in this step was to formulate different clamping possibilities to later evaluate their behavior on the structural analyses. Thus, new configurations that respected the design constraints were drawn and the empirical equation above shown were applied to these cases. For the values obtained from the torsion and tilt equations a safety factor of 1,2 and 1,75 was enforced, respectively. This allowed the formulation of the following options:

- NSE plus 176: 12-Points Square 960mm: 4 Clamping Modules each side
- NSE plus 176: 2 Modules at corners + 4 Modules on the symmetry axes
- NSE plus 176: 3 Modules at the corners – 2 Outside, 1 Inside
- NSE plus 176: 3 Modules at the corners – 3 Outside
- NSE3 138: 4 Modules at the corners + 4 Modules on the symmetry axes
- NSE3 138: 4 Modules at the corners

The objective with these configurations was to gather as much as possible the clamping modules around the region where the robot feet are connected. Even if there were large strains on the edges or center of the robot plate, the important values are the displacements occurring on the robot. As a consequence, many of the configurations presented have the clamping points around the corners of the robot place, which is where the robot feet are placed.

Unfortunately, it was not possible to formulate any configurations of NSE plus 176 with 8 points. The only way to employ such configurations would require much bigger dimensions for the robot plate to use modules further away. This would certainly increase the plate strains near the robot feet regions. The least expensive configuration is the NES3 138 with only 16 points. The configuration with 20 NSE3 138 is slightly above the configurations' cost with 12 NSE plus 176, but it is worth to evaluate that option too. Might happen that a higher number of clamping points, although smaller in diameter, is favorable for lower displacements. With that

being said, all these 6 configurations were then introduced in Abaqus, and their respective structures responses were analyzed.

4.4.2.3 Clamping Modules Installation Type

Nonetheless, there is one last question that needs to be answered regarding the clamping modules. The type of installation on the structure plate. This installation can be full or partial - Figure 4.13. The full installation leaves 5 mm of space between the two connected materials, while the partial leaves 39mm. This shows what was previously mentioned, that the robot plate will have not contact with the structure plate.
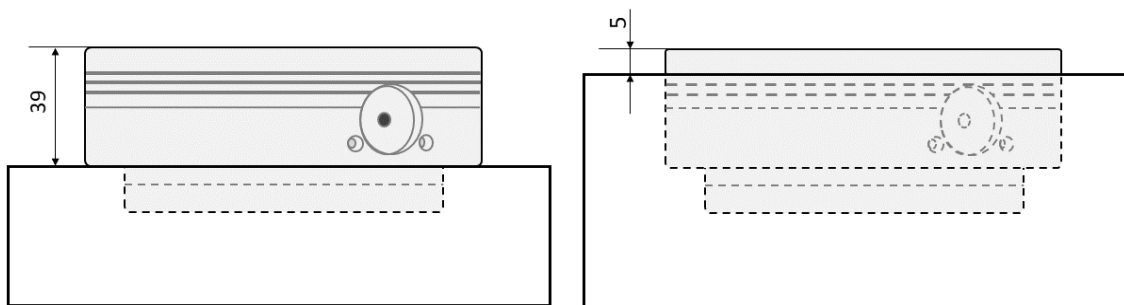
Figure 4.13 - Schemes of the two installation type options with Partial on the left, Full on the right

In both installation types the supported forces have the same value, because they depend only on the screws attaching the clamping point to the structure. In a full installation would be hard to use the lateral air channels to command the clamping mechanism. It would require machining the plate in the horizontal direction, which is too expensive. For the partial installation this actuation could be possible since it only requires through holes along the thickness. Other advantage of this installation type is the possibility to use the larger space between both plates. This space could be used for longer screws and nuts to attach the robot, for example. The only inconvenient in this solution, is the chance for some manufacturing waste or other objects to enter this space. Due to the larger flexibility that the partial installation offers without any loss of performance, this installation type was chosen for the structure.

4.4.3 Clamping Pin Attachment

The clamping pins are the metallic revolution parts that are locked inside the clamping modules hole. These small components have a through hole in its axis where screws are introduced to connect the pin to the desired pallet. These screws are hexagon socket head cap type of steel grade 12.9 - DIN EN ISO 4762 - 12.9 – and can have M10, M12 or M16 diameters depending on the holding forces required. The clamping pins can be attached to the workpiece in two different ways if the M12 screw is utilized as shown in Figure 4.14. For the M10 the solution on the right needs to be employed and for the M16 screws the option on the left. In its assembly manual SCHUNK defines minimum thicknesses for the attached plate depending on the screw utilized, but those values are inferior than the 40mm thought for the robot plate.
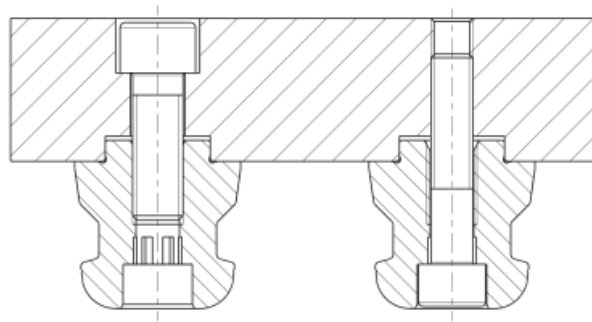
Figure 4.14 - Clamping pins attachment option to the pallet (SCHUNK GmbH & Co. 2018)

SCHUNK offers a wide variety of clamping pin solutions with different functions. Inside their standard clamping pins class there are the centering pins (SPA), the positioning pins (SPB) and the holding pins (SPC). The centering pins have the highest position accuracy and act as the pin that set the position of the pallet on that point. The other pins allow an easier coupling for pallets without precise positioning tolerances (above 0,01mm). The SPB allows slight displacements on one direction and the holding pins SPC have a centering clearance of 0,1mm. These latter pins should be used for areas where the alignment of the workpiece is not intended. An example for the use of these pins is shown in Figure 4.15. One SPA is used to define the position of the pallet, another SPB to restrain the displacements in on direction, and the other SPC pins with no positioning function, just intended to hold the pallet in place. Since the robot plate is also one unique component, a similar solution should be utilized for this work.
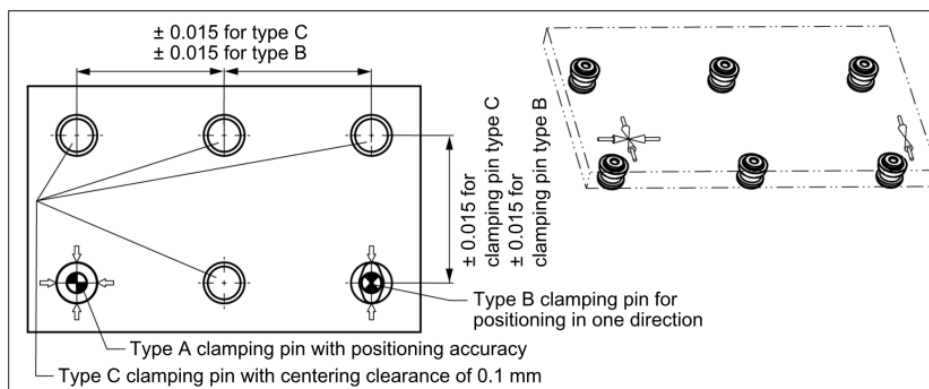
Figure 4.15 - Arrangement of the different types of clamping pins (SCHUNK GmbH & Co. 2018)

Besides these 3 pins, there are also the accuracy pins (SPG) which are suggested to substitute all other pins in situations where several clamping positions are necessary. However, these do not support M16 screws and so their maximum holding forces are lower (SCHUNK GmbH & Co. 2018).

For the proper positioning and holding of the robot plate, it was necessary to decide which type of clamping pins will be used, where should they be used, and also which screws should attach the pins to the robot plate. The selection of the screws was done based on the maximum internal stresses occurring during the numerical simulation and the suggestion of SCHUNK

engineers to use M16 screws. The type and location of the clamping pins was done after the clamping configuration was selected. The objective was to utilize a centering pin SPA near one of the robot's foot, then another SPB close to another opposing foot, and fill the remaining clamping positions with SPC pins.

4.4.4   Updated Abaqus Model

At this point, there was enough knowledge on how the clamping procedure of the industrial robot to the modular structure should be executed. Configurations with different clamping module positions were defined, the clamping pins' functions and connections to the robot plate were studied, and the starting dimensions for that same plate were set. It was now possible to update the simple structure module with far more detail on the robot load transmission. The new components could be introduced in the FEM computer program and the analyses of the different clamping positions could be performed. But before running into that, it was necessary to validate all these new connections that are established between the different elements of the model.

To make sure the interactions of all the parts of the system were behaving in a close manner to the physical world, it was decided to create a first trial model to study those relationships. This model would serve to test different contacts and interaction properties available in Abaqus for the purpose of selecting the most appropriate case for each connection. It was decided to start analyzing a robot plate coupled to the structure by only eight clamping positions. This lower number of connections was chosen, to reduce the amount of work in changing the parameters or type of each connection. This would also help to identify more rapidly any simulation problems or errors. In the following paragraphs are explained how the physical connections between the bodies might occur, and it is presented how those relations were replicated in Abaqus.

4.4.4.1   New Components of the Model

For start, the robot plate was modeled with the same dimensions of the COMAU installation. A plate area of 1,2x1m² with 40mm thickness and all the eight holes used to attach the robot feet – form here on called as "robot holes". Additionally, other eight through holes were modeled for the connection with the screws of the clamping pins – also called as "pin holes". The material used by the robot manufacturer for their installation plate is also a steel. Therefore, the same material properties used for the base structure were attributed to the robot plate. For the discretization of the component, the element type selected was the C3D8. The geometry and load submitted to this plate are similar to the simple model cases in the first and second steps. Thus, it was expected that the structural response of this new plate would be identical. The C3D8 element was already proven to be the best option for this situation, and so it was the again selected for the robot plate.

The clamping modules utilized for this contact analysis were the larger ones - NSE plus 176. The dimensions of this component were taken from technical drawings in the SCHUNK catalogue and used to model a revolution part in Abaqus (SCHUNK GmbH & Co.). It is here important to refer that this component was considered as a rigid body. After consulting SCHUNK Services on this matter, they confirmed that the deformation on the clamping modules - due to the load on them exerted - could be neglectable. Therefore, there was no reason to include these bodies

in the simulation has deformable. As a consequence, they would have no internal stresses, transmitting all the load to the adjacent elements. The rigid bodies do not possess material properties as they solely act as a geometric entities. Nevertheless, a point mass with the same weight of the clamping module was attributed to each part. The finite element type used for this component was the R3D4. It is a rigid quadrilateral element with 4 nodes and was the only discrete element available for this component - Figure 4.16.
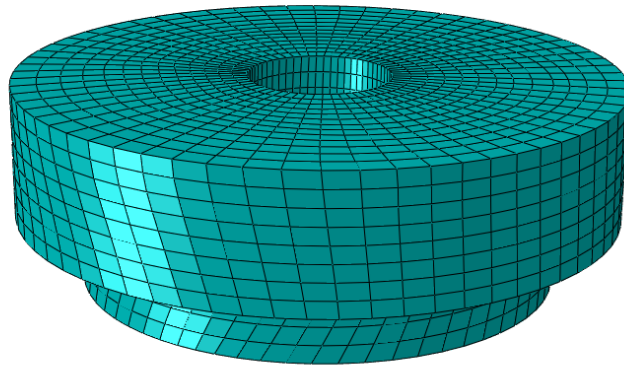
Figure 4.16 - Clamping module part after the discretization process

The clamping pins and their screws were generated as an entire single part. This was done to spare more connections between elements and reduce the model complexity, although compromising the approximation to the physical world. It was considered that modeling these two components as one, would induce no large deviations on the simulation results. This part was modeled as an 1D wire with the length equal to the sum of the plate thickness and the clamping pin length. To attribute the different diameters – corresponding to the screw and the pin - two different sections were created in Abaqus. One with a 16mm diameter circular profile and another with 40mm of diameter. As just implied, the screw size chosen was the M16, as it was already expected the occurrence of large stresses at these components. The shape of this entire part can be seen in Figure 4.17.
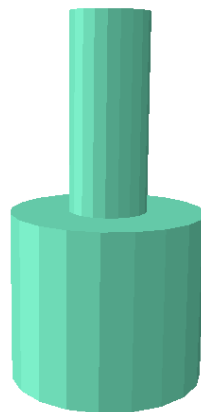
Figure 4.17 - Modeled part in Abaqus to represent the clamping pin - screw assembly

Regarding the materials, the clamping pins are made of a hardened stainless steel, while the 12.9 grade screws are quenched and tempered alloy steels. These are broad definitions making it difficult to find proper elastic modulus. Even if the yield and tensile strength are given for the screw, those values are not relevant for this simulation inside the elastic regime. Due to the lack of better options, the same plain steel properties defined for the base structure were attributed to this component. The type of element chosen for this wire part was the B31. This element follows the more realistic Timoshenko beam theory and is also the recommend option for situations that involve contacts (Dassault Systèmes 2020).

Lastly, it was necessary to adjust the base structure component to accommodate the clamping modules. The base upper surface was edited to create the eight depressions where the modules would be inserted. Having chosen the partial installation type, these cavities had a diameter of 138mm and 20,8mm of depth. These are not through holes and that is problematic for the use of hexahedral shape elements on these regions. Instead, tetrahedral elements had to be employed to properly represent these features. However, these elements are not a good option to model the entire base structure, due to their low computational efficiency outside the clamping region. On the other hand, a discretization that uses both element types - tetrahedral around the clamping holes and hexahedral on the reminder areas – has incompatibility problems on the interface of both elements. Fortunately, Abaqus automatically solves this situation by creating an internal tie constraint that prevents the relative movement of the nodes on both surfaces.
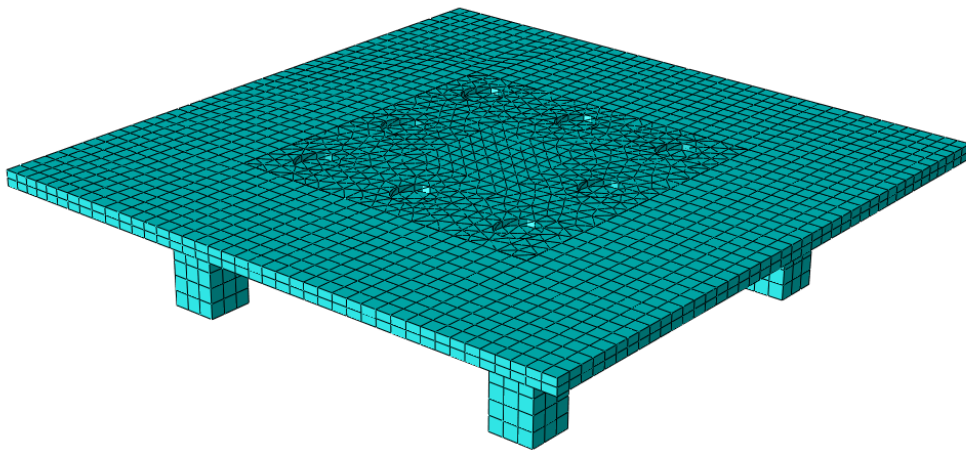
Figure 4.18 - Base structure part after discretization

Having properly modeled all the components, it was then possible to start defining their relationships. It is relevant to mention that the coordinates of the reference point where the robot load is applied were changed to coincide with the center of the upper surface of the robot plate. In the following paragraphs are discussed the physical connections between the different parts and how these were modeled in Abaqus to portrait the same behavior in the computer program.

4.4.4.2 Relationships between components

Starting with the installation of the clamping modules on the base structure, this fixture is performed by 6 M8 screws distributed around the outer section of the clamping part - Figure 4.19. The screws secure this component's position fixing the transition surface of the clamping module - between the two regions of different diameter – to the surface of the workpiece. These two surfaces are supposed to have no relative movement to one another. Thus, it was chosen to model this connection in Abaqus employing a Tie Constraint. The clamping transition surface was selected as the master surface, while the upper surface of the structure worked as the slave.
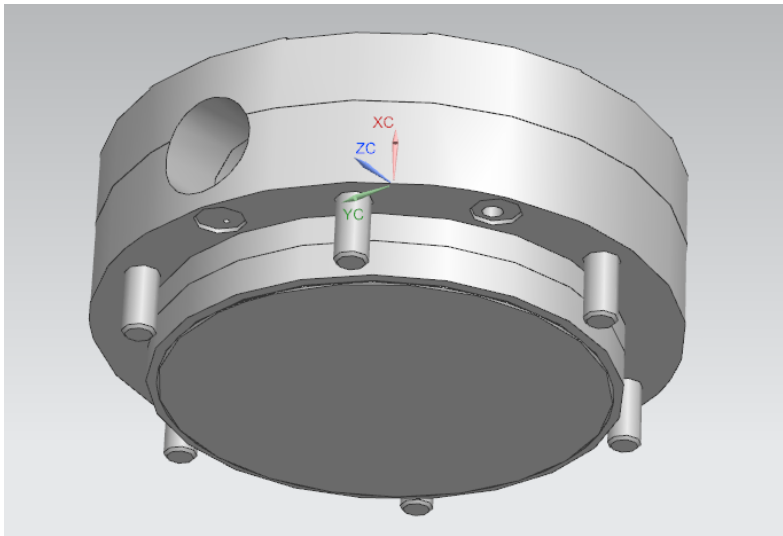
Figure 4.19 - Underneath view of the clamping module with its six M8 screws

On the other end of the clamping modules are placed the desired pallets. In this case, the robot plate is laid on top of these components and then fixed. The upper surface of the clamping parts will sustain the plate when it is pressed by the robot load. To model this connection, a Hard contact with frictionless characteristics was attributed. The frictionless option was used because of the low expected relative movement between the surfaces. The clamping modules upper surface was defined as the master surface since it belongs to rigid bodies. The lower surface of the robot plate was selected as the slave. The contacts were defined as small sliding – due to the low relative motion – and the Surface-2-Surface tracking method was employed because it better replicates a physical contact.

Regarding the pin clamping procedure, this attachment occurs through a locking mechanism that slides internally in the clamping module body and clamps the pin in its lower diameter section. Basically, the larger diameter section at the bottom of the pin has its movement restrained by two metallic components – as depicted in Figure 4.20. This is a much more complex connection because it relies on the contact of a radially sliding component that impedes the movement of another component possessing an inner cavity intended for that function. Since in the program none of the modeled elements had this level of detail, it was thought to replicate this connection in the following way.
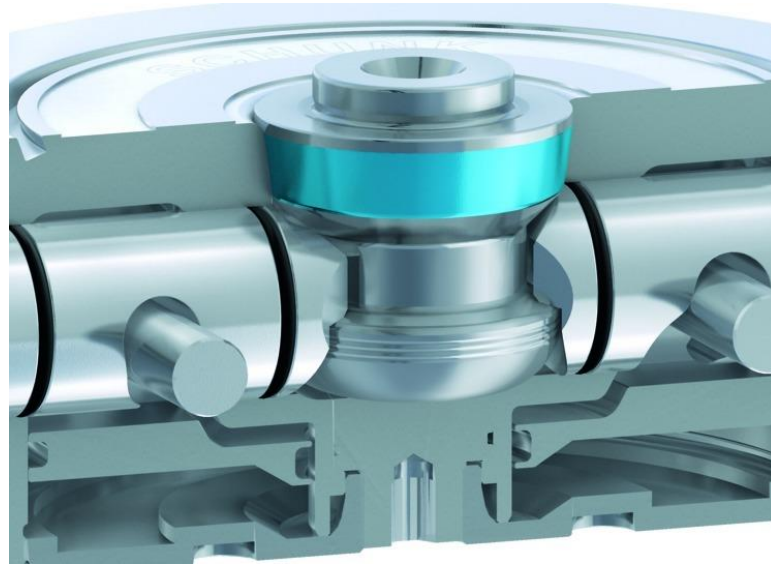
Figure 4.20 - Cut view of the clamping module exterior body (SCHUNK GmbH & Co. 2021)

In the clamping operation the bottom of the pin is completely locked, but the section above the sliding mechanism is free to deform. Focusing on that aspect, the pin-screw body was sectioned at the location where the locking mechanism closes – at the bottom of the smaller diameter length - and the region under that point (approximately 13mm length - Figure 4.21) was constrained to the rigid part portraying the clamping module. The constraint type used was the Coupling Constraint, which prevents the motion of the lower section of the wire body to the center of mass of the rigid body. As a consequence, the bottom portion of the pin-screw part was constrained to always have the same motion of the rigid body, which recreates the actual physical connection.
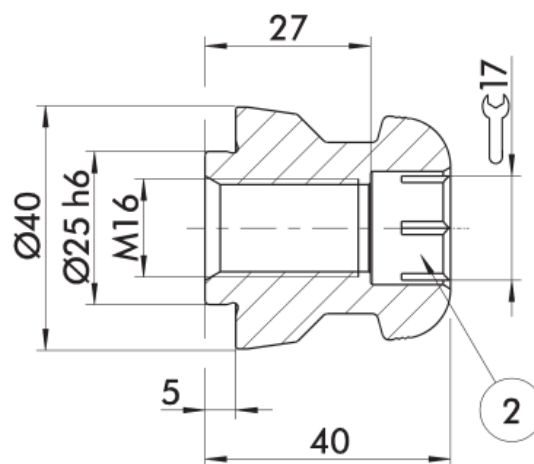
Figure 4.21 - Technical drawing of the clamping pins (SCHUNK GmbH & Co.)

On the other end of the 1D body was necessary to define the connection of the pin-screws to the holes of the robot plate. Recalling the left side of Figure 4.14 for the M16 screw case, it can be seen that the screw thread only fastens the clamping pin inner hole and not the walls

of the pallet hole. In other words, the pallet only contacts with the screw at the screw head. When the screw is being rotated, it is pressing the upper surface of the pallet down, while the clamping pin – which acts like a nut - is tightened to press the lower surface up. This connection resulting in the pallet compression is what holds the three elements all together. Such a relationship is hard to model with the virtual components created. Since the pin-screw part was modeled as an 1D body it is not possible to create the contact interactions between the screw head or the pin and the plate surfaces.

To better represent this connection, the pin-screw part was sectioned at the plate thickness length and the robot plate surfaces were partitioned to represent the screw head and the clamping pin contact areas. An M16 screw possesses a screw head with 24mm diameter and a SCHUNK pin contacts a pallet through a circular area with 40mm diameter. Thus, these circumferences were created on the respective surface of the robot plate around the pin holes. Having created these partitions and sectioned the 1D pin-screw component, allowed to choose the upper and the newly created point of the wire body to couple them to the respective circular area - Figure 4.22. This coupling was made through MPC constraints. With this, the two points of the pin-screw body were locked to the robot plate surfaces.
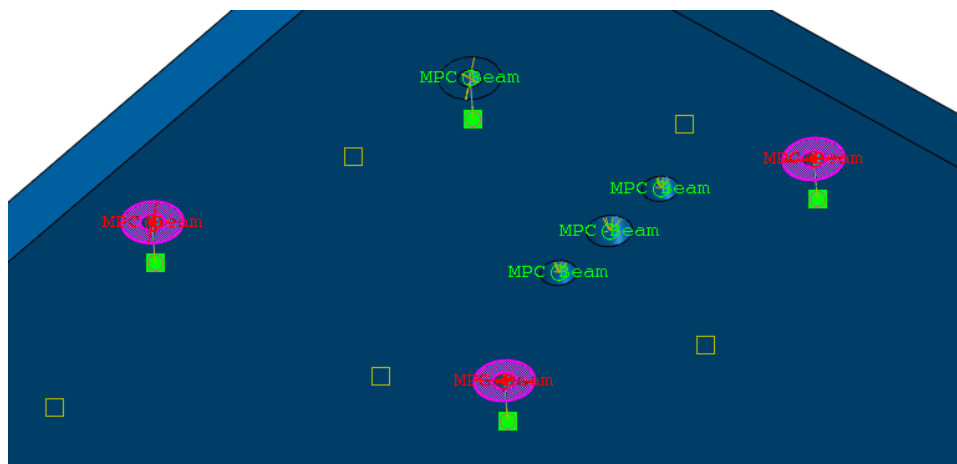
Figure 4.22 - Visualization of the MPC Constraints between the pin-screw bodies and the robot plate

It is true that all of these connections between the clamping module and the screw holding the clamping pin to the pallet, could be further improved to better characterize the physical interactions between these different elements. The pins and screws could be modeled separately and as 3D bodies instead of 1D. The clamping pin could possess the cavity where the sliding mechanism of the clamping module enters. This own mechanism could be modeled and have its actuated position fixed. Then, all the proper contacts could be created and applied between the bodies. This would make the virtual model as close as possible. However, the probability of aborting the simulation or occurring other problems would be extremely high with so many contacts and relations. In FEM analyses, contacts induce a lot of complexity, and so simplifications should always be used when possible. The best options found for the clamping procedure connections were the ones exposed, therefore these were employed for all remaining steps of this dimensioning work.

At last, it was necessary to select which regions would be connected to the load reference point. Until here, this RP had been coupled to the entire upper surface of the structure plate. But, in reality the robot is only supported by the 4 feet and attached by 8 holes. This means, the robot load would only be transmitted from these regions. To better represent this, the area of the robot feet was drawn on the upper surface of the robot plate, and the reference point was coupled to these regions. In this way, the load of the robot would only be applied at the interface regions where the robot is supported, instead of dividing it equally through the entire surface.

With this, all the relationships between the different components of the model were properly defined. After the simulation, their motion behavior was studied and considered to be close to an expected physical situation. No part would penetrate the geometry of another, neither the stresses along the holes of the robot plate were unreasonable, nor the deformation of the structure base around the clamping module seemed unrealistic. Those small details convinced the use of the connections above exposed. Keep in mind that there are - and were tested – many other possibilities to couple the same two elements. The described connections were the ones that seemed more appropriate and were consequently selected for the next steps of this work. The assembly of this updated model is shown in Figure 4.23.
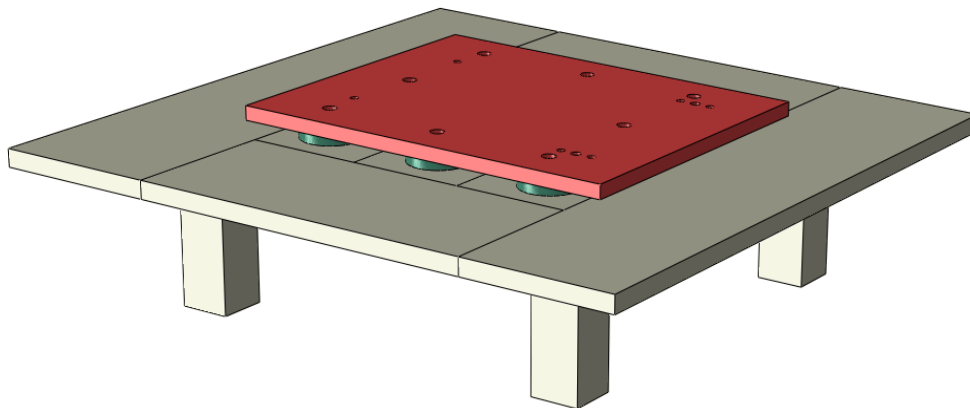
Figure 4.23 - Updated version of the structural model

4.4.5   Robot Feet Behavior

Although the introduction of new components increased the reliability of the FEM model, the manner of how the load was being distributed did not reflect a proper load transmission. Even if the load was only applied at the equivalent robot feet area, there would be certain situations in which this distribution method would deviate profoundly the robot plate structural response from the expected physical behavior.

When the immobile robot is placed on a surface, all the underneath structure will be pressed down due to the gravity. The four feet of the production unit distribute the load according to the position of the overall mass center of the machine. When the robot is being actuated, the load transmitted by one of the feet will change throughout the movement. For example, if the robot arm is fully extended at the front, the front feet will press more heavily

the plate, while the feet on the back could even be lifted. To prevent this, the robot is attached by screws to the plate, not allowing this upward movement of the feet. When such situations happen, the screws will generate local stresses on the holes which are being pulled up.

The type of coupling used to distribute the robot load does not reflect such event. Because the reference point is connected to an area equivalent to the robot feet, an upward movement will carry all that region, rather than concentrating it at the holes that attach the robot. This means, this load distribution would hide stress concentration points. Since this is an important aspect to properly ensure the structural integrity of the robot plate, the model was improved to capture this physical situation.

After trying different options, the best solution found was to import the CAD file of the COMAU machine Base part and connect it to the upper plate. To do so, the new imported part was placed in its corresponding position and the eight screw connections were made with rigid beam type MPC constraints. This screw connection was not modeled with deformable bodies – like the screws of the clamping pins – not to increase the model complexity. Besides, there was no intention to study the structural response of these screws since the robot plate dimensions are the same as the installation solution proposed by the robot manufacturer. Therefore, there should be no reason to doubt the screws functionality, providing that the ones used are at least the same as indicated on the installation guide.

In the last task the load reference point was connected to surfaces on the robot plate equivalent to the machine support area. To properly obtain the desired physical behavior, this load had to be applied on the robot part. It was decided to distribute the load only on the bottom surfaces of the feet – which contact with the plate – because selecting more regions on the machine would make these more susceptible to deform. This in turn, would make the robot part also hold some of the load, alleviating the stresses on the supporting platform. As the load results taken from the motion analysis are entirely sustained by the single base joint, the robot parts should not be affected by it. Thus, the best option was to exclusively select the bottom of the robot feet surfaces. Still on the loading aspect, it is important to mention that this added part was not considered for the gravity force on the model. Otherwise, it would erroneously increase the force on that direction, when it was already included in the load applied at the reference point.
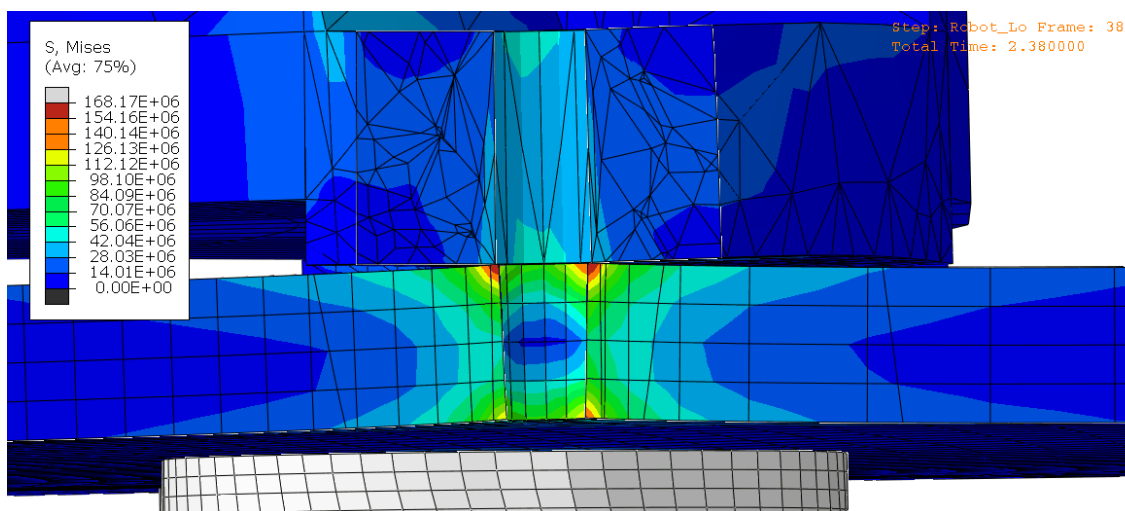
Figure 4.24 - Visualization of stresses results on the robot connection of the updated model

After simulating this model with the imported robot part and the constraints created to imitate the screw connection at the robot plate, the results show the behavior that was intended to achieve. In Figure 4.24 it can be seen that the robot foot is being elevated and pulling only the robot hole concentrating the stresses at its ends.

4.4.6 Clamping Positions Analyses

After all previous tasks, the load transmission from the robot feet to the structure base occurring in this model seemed reasonably close to a future physical construction. No other options were found to enhance further this model without increasing considerably the model complexity. Taking that into consideration, it was decided to start testing the above-proposed clamping configurations. The objective was to compare the displacements occurring on the robot plate near the feet and make sure there were no regions developed too high stresses. Additionally, the internal forces at the pin-screw part were also evaluated to make sure the maximum holding forces were not being exceeded.

To compare the different clamping configurations, separate models were created. All of these new models were copied from the one until here developed, being then modified according to the clamping positions. The structure plate was edited shifting the modules' cavities to the new locations, as well as the clamping holes on the robot plate. For some models the area of this plate had to be increase, otherwise the pin-screw holes would be too close to the edges. For the last two configurations with the NSE3 138, the dimensions of the rigid body that replicated the clamping modules were altered to describe the geometry of this smaller version. For the same reason, the mass of the inertia points at each rigid body were also adjusted to their lower values. Then, the assemblies were again constructed to move all components to their new locations and the interactions between all parts of the system were again established. All the other aspects of the model remained the same as the previous version. In Figure 4.25 are shown the underneath views of the robot plates with the different clamping configurations.
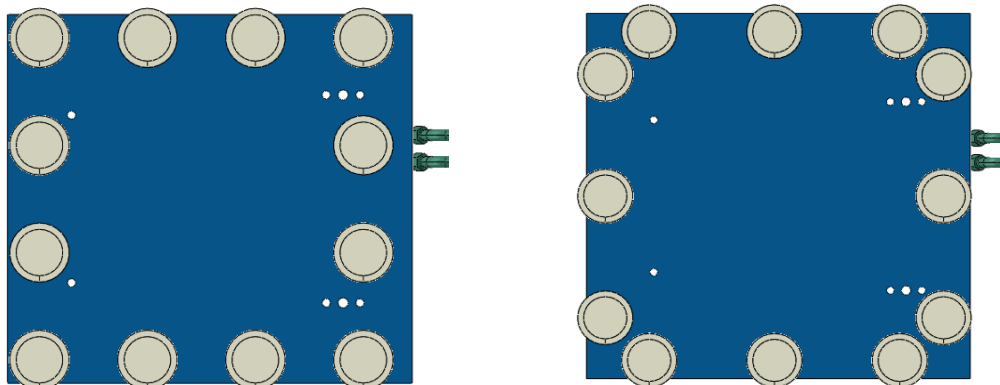
Configuration 1 – 12 Points distributed along a square with 960mm on the sides

Configuration 2 – 2 Modules concentrated at the robot plate corner plus 1 Module at the center of each edge
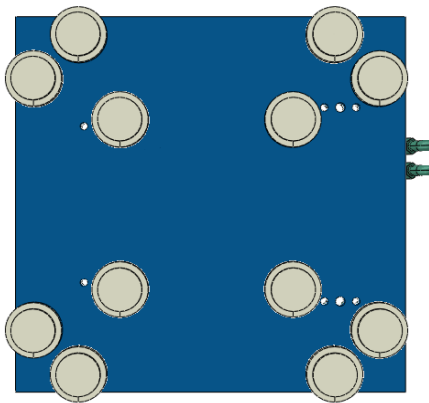
Configuration 3 – 3 Modules at each corner with 1 of them side the robot feet region
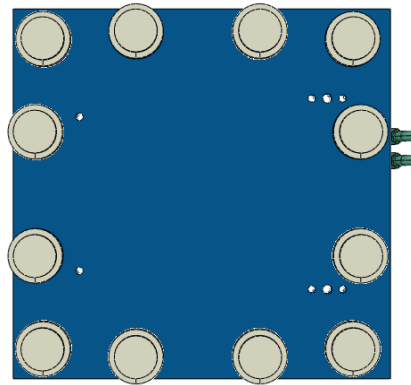
Configuration 4 – 3 Modules at each corner all on the outside
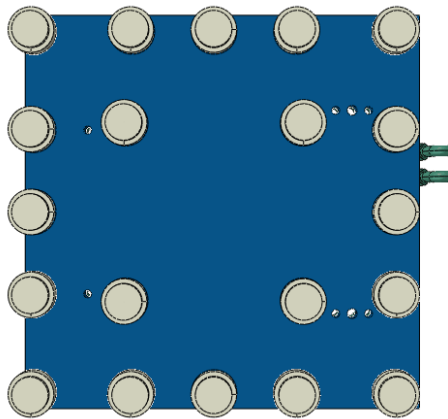
Configuration 5 – 4 Modules (NSE3 138) at each corner plus one at the middle of each edge
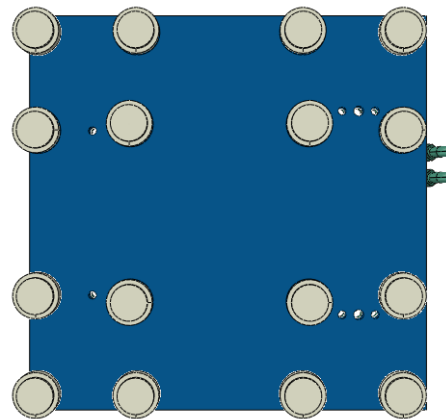
Configuration 6 – 4 Modules (NSE3 138) at each corner

Figure 4.25 - Clamping configurations elaborated

With all systems properly defined, their structural responses under the robot load were simulated. The maximum stress locations were all arising at holes in the robot plate. In some cases, those points appeared on top of a hole attaching the robot, in others, they appeared at the bottom of the pin holes. As expected, these regions promoted stress concentrations in the FEA program which were later confirmed to also have singularity points. It was also noticed that the largest strains were developing on less relevant regions of the model. A usual location was at one of the corners of the robot plate. The deformation at this point did not evidence how exactly the robot was being affected and also made it hard to compare different configurations. Therefore, it was decided to study the maximum resulting deformations on the region around the machine's feet. The results from the different clamping systems simulations are presented in the next Table 4.8.

During this step of generating and simulating different clamping configurations, it became evident that the best solutions would involve gathering the highest number of clamping positions around the robot feet. At the same time, it was clear that at least one clamping point was necessary inside the robot feet area. This would reduce the upper plate capacity to bend under the load. If no module was used in this region, all that interior area would be hanging

only supported by outer clamping points. By adding supports in those regions, the hanging distance was heavily reduced, leading to lower deformations. Doing so, also reduced the stresses on the outer clamping pins, homogenizing the load distribution.

Table 4.8 - Numerical results obtained for each type of clamping configuration

NUMERICAL RESULTS	1	2	3	4	5	6
MAX OVERALL DISPLACEMENT (µm)	283,0	277,3	237,8	280,1	233,0	222,1
MAX ROBOT FEET DISPLACEMENT (µm)	258,2	245,5	210,1	254,7	219,1	204,7

At this point, it is important to refer that the results shown in the table were not obtained immediately. The initially formulated configurations had different distances between the clamping points, and their structural results were worse than the ones shown. Those initial positions had been selected only to fulfill the design requirements and withstand the maximum loads. While editing the new configurations, it was noted that the position of the clamping modules could be reasonably modified to achieve better solutions. One of the main aspects realized was that the configurations with a clamping point inside the machine feet would perform better if the area of the robot plate was increased. This added space would provide more freedom to select the position of the outer modules and consequently try different locations to obtain better structural responses. For example, the initial fifth model formed a square of 960mm with five modules on each side plus another four making a square with 540mm. Increasing the robot plate area from 1,2x1m² to 1,2x1,2m² and pushing the clamping points on the outer square to form a 1050mm side square - while maintaining the inner 540mm square - reduced the displacements by 22%.

For this reason, different positions of the clamping modules were tested for the same configurations. These trials were merely based on intuition and the locations of the points were never drastically modified, but it was enough to improve the initial results. At the end, it seemed that the best configurations should distribute the clamping modules evenly around the robot feet, while trying to keep them as close as possible to the robot holes. The results shown in the table above are the best obtained after experimenting with different module positions for the same type of configuration. Even the stress results are in general similar for both models – only showing high stresses at singularity points at the holes.

Regarding the displacements the two best options found were the third configuration - 3 NSE plus 176 around each robot foot with one inside – and the sixth configuration – 4 NSE3 138 around each robot foot. This last configuration is 14,6% less expensive and shows slightly smaller strains at the robot plate. Regarding von Mises equivalent stresses, both models exhibited in general similar results. The exact position of the clamping points of this system are presented in Figure 4.26
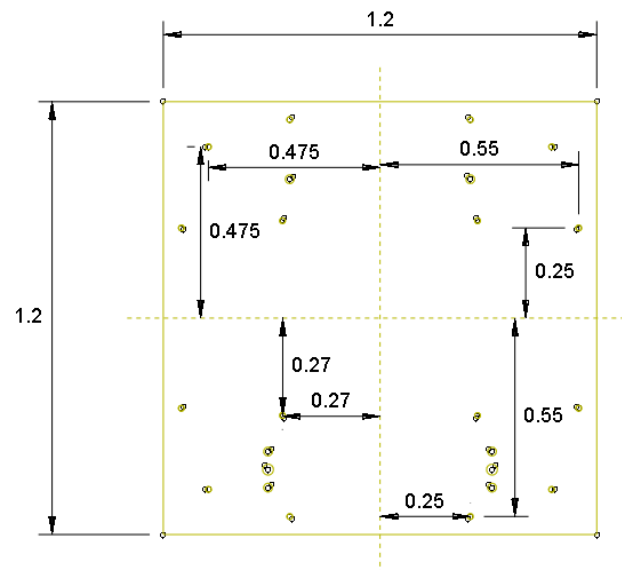
Figure 4.26 - Sketch of the robot plate with the clamping positions of the selected cofiguration

Having chosen the clamping positions to use in the next steps of this work, it remained to confirm that the M16 screws could sustain the load transmission to the clamping modules. From the SCHUNK Catalogue these screws can hold the clamping pins until a maximum pulling force of 75kN. This means, the pin-screw parts in the model should not have internal axial forces above that value. In order to analyze these internal forces, it was necessary to add a new output for the simulation. The numerical results that show the internal forces occurring in a beam section are the NFORCSO – nodal forces in beam section orientation. With this output it is possible to take the shear or bending diagrams for beam parts, for example.

From the simulation with the 16 NSE3-138 clamping modules the highest axial force values obtained for all pin-screw parts in the model were 42,7kN under tension and 62,0kN under compression - Figure 4.27. This tension value appears on the interface between the robot plate bottom surface and the clamping pin larger diameter, when the plate is pulling the clamping module upward. On the other hand, the maximum compression occurs at the middle of the clamping pin length, when the plate is pressing the clamping module against the structure. However, this compression force value is higher than the allowable axial forces for the clamping modules (28kN). This suggests that the component would fail due to the high compression stresses from supporting the robot plate.

This event seamed unreasonable, even if the plate was only being supported by 16 modules. The high compression forces were certainly related with the type of connections selected between the parts in the model. To confirm this, it was decided to analyze the internal loads appearing at the pin-screw parts in FEM models that portrayed the clamping configuration examples shared by SCHUNK. Knowing the maximum loads supported by each solution, would be possible to check the maximum internal forces at the respective pin-screw bodies. Even if the results obtained were high, it would only mean that the modeled pin-pallet connection was not behaving properly or was poorly distributing the loads.
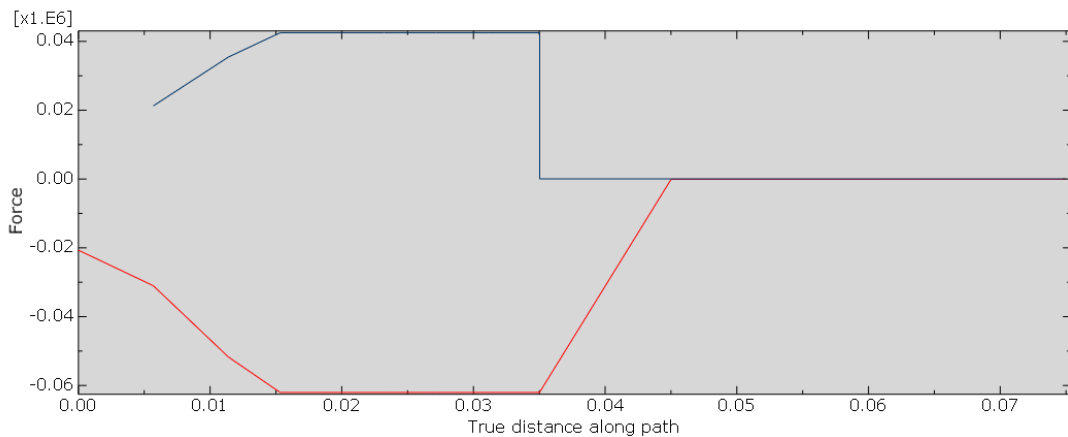
Figure 4.27 - Pin-Screw internal axial forces plot exported from Abaqus

Therefore, three models were created with the robot plate supported by the clamping configuration examples given by SCHUNK. The load applied to the reference point was changed to the maximum respective values of each solution. After the simulations, the axial internal forces were taken for the pin-screw parts. The results for the three models were: 91,9kN, 110,6kN and 111,9kN for the maximum tension forces and -151,2kN, -145,4kN and -154,9kN for the compression forces. Comparing these results with the ones obtained in the 16 modules configuration, it is safe to assume the M16 screws can withstand the pulling forces from the robot plate. The results in the SCHUNK models were much higher and these represent proved solutions in practical applications, therefore there is no reason to doubt the clamping modules, or the screws in the proposed configuration will fail under the robot operating load.

The selection of the M16 screws for attaching the clamping pins concluded this third step of the dimensioning work. The objective was achieved: an improved model where the load transmission from the robot to the structure was closer to a future construction and the selection of the clamping configuration. This model was then carried for the next stages of the work. To ease the computational requirements of the solution, the robot Base component was sectioned – Figure 4.28. The maximum displacement on the robot feet region of this model was 205,9µm at the left rear foot of production machine.
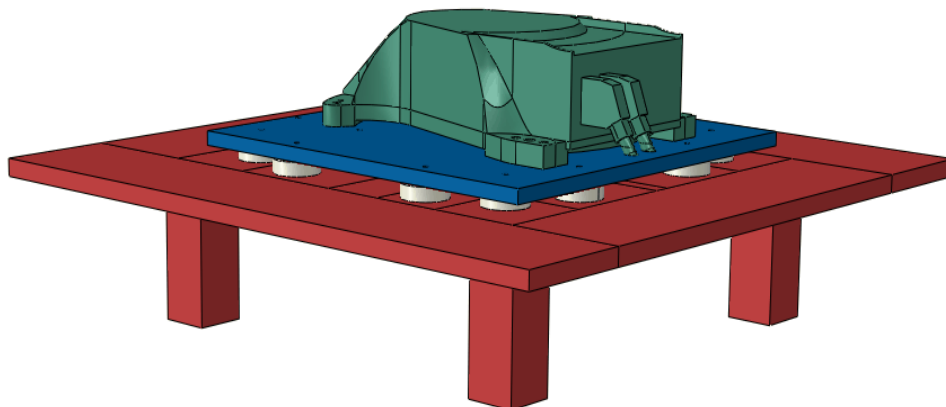
Figure 4.28 - Updated structural model with the robot base part

4.5   Experimenting Different Solutions

This step was intended to experiment different possibilities to reduce the maximum displacements at the robot plate. The objective was to work around the components dimensions of the previously selected model in order to find better solutions. Obviously, increasing the thickness of both – structure and robot – plates would provide better results. But this was the last option explored, since it would add much more material on the plates, and thus, raise the materials cost. In addition to changing the components' sizes, it was also tried to introduce new elements to act as reinforcements of the robot plate.

Starting with the size of the structure plate, it was realized that the central hole through where the cable connections are brought from underneath the structure had not yet been created. This hole dimensions – $0,205x0,305m^2$ - were taken from the work previously done at the institute and applied to the structure plate. Note that this feature is not symmetric, so it will have to be later analyzed if this raises problems at the robot connection, when it is attached in perpendicular directions. After simulating the new model with the supply interface hole, the results revealed no significative difference. There were no stress concentrations on this new hole border, and the maximum displacement at the robot plate only increased 2,7%.

Still on the structure plate regard, it had been previously noted that the chosen area of $2x2m^2$ was not a favorable option. That became even more evident when the physical COMAU machines were delievered at the institute facilities. The robot arm when fully extended can almost reach a distance of 3m. Considering that the robots will be placed at the center of the modular construction, there are two construction possibilities for the fake fabric ground. The modular structure has an area of $1,5x1,5m^2$ and two adjacent production machines must have at least one unoccupied station between them, or the plate area covers $3x3m^2$ and adjacent robots can be placed on adjacent working stations.

The WSK projects requires the possibility to execute manufacturing tasks by co-working of machine units. Thus, there should be a common space shared by the working areas of both robots. Until this point, there was no calculation on preferable or limit distances between two production systems, and so it was assumed that a distance of 3m was a good option. This meant, the $2x2m^2$ area could not be kept. It was too small for adjacent robots to be placed side-to-side, but also too large to use intermediate unoccupied stations. As so, the two options exeposed above were developed and submited to the robot loads in the FEA program.

The maximum displacement results revealed interesting aspects. The larger plate area added more weight outside the structure legs, thus generating higher displacements on the outer edges of the structure. What is interesting is that the center of the plate – where the robot is fixed – had lower strains, because the plate was bending on the opposite direction. By increasing the structure plate area, the bending at the center – due to the robot load – was counteracted by the bending of the plate, due to the added weight outside the supporting legs. For this reason, the displacement results for this model were 8,5% smaller than the modular structure with $1,5x1,5m^2$ plate area. In Figure 4.29 is shown a cut view section at the mid plane of the model. The deformation was scaled by 1000 to better percieve this phenomenon.
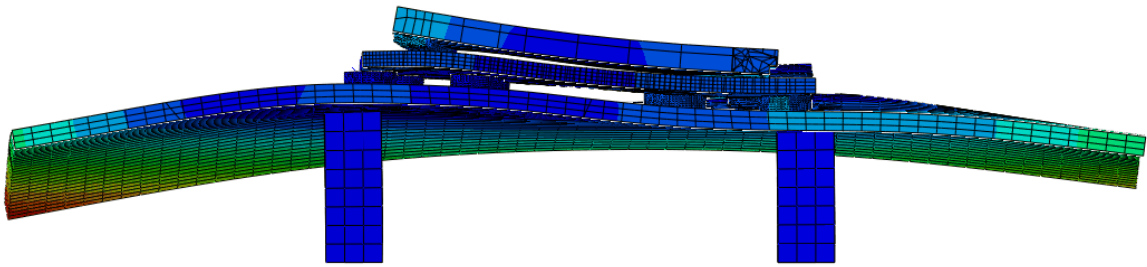
Figure 4.29 - Cut view section from the structural model mid plane

Although this seems an interesting possibility, it is necessary to account the load this structure might have and that was not here taken into consideration. The only load applied in this model was from the robot critical motion. The structure plate is supposed to work like the false ground of a production fabric, and thus more elements will be laid on top of it. This analysis was not considering that extra weight at the edges of the structure. This means that the position of the legs would have to be adjusted, possibly increasing its number. However, that would certainly reduce the counter-bending effect at the center of the plate. On the other hand, the smaller plate area has higher strains and the number of modular stations necessary to cover the same fabric area is much higher. One single 3x3m² plate covers the same area has 9 modular stations with 1,5x1,5m². This has the added cost to buy and install clamping modules that are not being used. Even if the maximum displacements are increased - by adding more legs on the structure -, the plate area with 3x3m² was selected due to its lower components' costs.

4.5.1   Robot Plate Area

With the base structure dimensions settled, it was time to explore the size of the robot plate. At this point, the area of this plate was 1,2x1,2m² with its center slightly displaced from the robot reference point. Although, the clamping positions above tested were bisymmetrical, the center of the installation plate from COMAU handbook was 25mm closer to the rear of the robot. This meant, the clamping modules on the front of the robot were closer to the robot plate edges than the ones on the back. In order to homogenize these distances and make the clamping holes' locations bisymmetrical at the robot plate, the center of this component was pushed to the robot reference point. After running a simulation with this plate centered position, the displacement results decreased 7,4%. For the sake of completeness, another simulation was performed with the robot plate now shifted 25mm to the front of the robot. The maximum displacement numerical result for this model was 1,4% higher. This might suggest that there is a better solution than a centered plate, if a deeper analysis is run. However, since it is easier to manufacture the clamping pin holes at the same distance from the center and the strains do not decrease substantially by shifting the center of the plate, it was decided to have the robot plate centered with the robot first axis.

Then, it remained to see how varying the area of the robot with the clamping positions fixed would influence the structural results. As a consequence, it was decided to increase the area to 1,3x1,3m² and then to 1,4x1,4m². The results of these two models showed a very small decrease on the maximum displacement values. The largest robot plate had a decrease of 0,4%. At last, it was tried to reduce the plate area as close as possible. The size of the plate was reduced until only 30mm separated the edge and closest the clamping pin holes. This resulted in a 1,16x1,16m² area. From the simulation of this model an increase of 2,1% at the maximum displacement was taken. Although the best solution was the largest robot plate, the reduction of the structure strains was very subtle. In addition, this solution would require more metallic material, which in turn implied higher costs. Therefore, the plate with 1,2x1,2m² area was chosen.

Until now, only square areas had been tested, so it was decided to experiment rectangular shapes. Two new models were elaborated with larger distances on one direction. One with 1,3x1,2m² and another with 1,2x1,3m². Both of these constructions had slightly worse numerical results than the square robot plate. The model with more mass along the frontal plain had better results than the large plate on the robot transverse direction. This established that a square area was the best option for the robot plate shape.

4.5.2   Robot Plate Reinforcements

Before moving to the study of the plates' thicknesses influence on the structural results, a different solution to try decreasing the displacements at the robot feet was experimented. This approach involved attaching new metallic components to the bottom of the robot plate in hope to increase the plates' bending resistance. The higher strains occurring at the structure are gathering around the robot feet, which press the structure down in some regions and pulls it up on others.

One could think of adding more elements that connect both plates, acting like additional supports directly transmitting the forces from the upper to the lower plate. However, this solution requires extremely tight tolerances for all components. Otherwise, the robot plate might be unproperly positioned when it contacts one of these elements before the clamping modules. This solution would require all components in between the two plates to contact the robot plate simultaneously when it is being attached. Such an option would raise drastically the manufacturing costs of the structure, due to the required high precision.

Instead, a better solution would be to attach smaller elements – by welding or bolted connections – to the bottom surface of the robot plate. These elements would be hanging only supported by its connection to the plate. The objective was to experiment different component sizes and shapes in hope its additional weight and manufacturing costs would compensate the reduction in deformation occurring at the structure. The upper surface of the robot plate was not even considered because it would be hard to couple more elements to that part. The machine already occupies a great portion of that area, while the space between the robot and structure plates is free to be exploited. The only constrains on the lower side was making sure these additional bodies keep a reasonable distance to the clamping modules and do not cross under the robot feet holes.
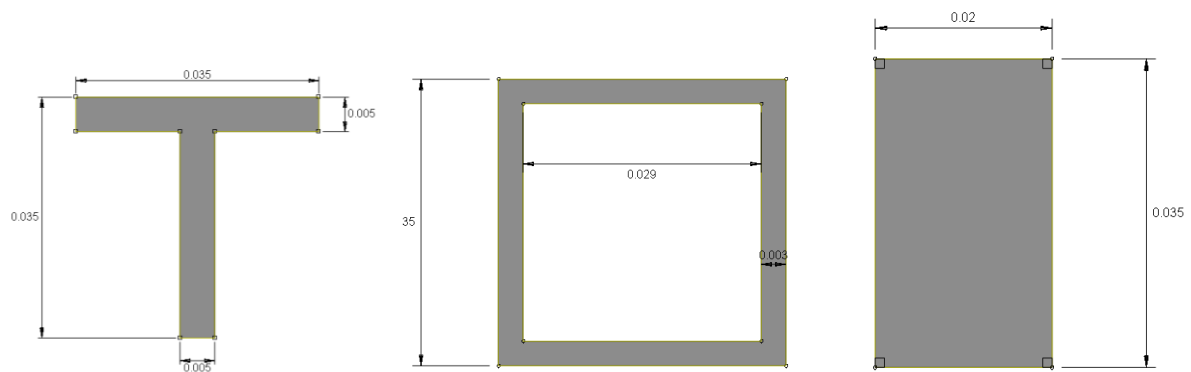
Figure 4.30 - Profile sections of the three types of reinforcements studied

At the beginning, it was thought of using beams or bars to reinforce the robot plate. These structural components include the best options in respect to bending resistance, and thus seemed a good starting point. However, the most promising option - I beam profile - could not be used because its minimum size according to international norms did not fit in the 39mm height of space available. Instead, it was necessary to search for other options that could be employed in this small space. From that search three types of elements were selected: T-profile beam (EN10055), hollow square section tubes (EN10219), and wide flat bars (EN10058) - Figure 4.30. For each of these components, the largest profile within the space available was chosen. In fact, there were more possibilities that could have been tested – like L or U profiles -, but it was decided that the 3 selected elements were already enough to test the effectiveness of this type of reinforcement.

The material properties attributed to these new parts were the same as the other steel components in the system. The type of finite element used to analyze these components was a continuum shell element, because it is more computational efficient and specifically appropriate for situations involving slender structures dominated by bending behavior (The Efficient Engineer Channel 2021). After modeled, these elements were placed on regions with the largest strains in the robot plate. The objective was to attach these components as close as possible to the robot feet. Having selected the positions for the beams, they were connected to the robot plate by Tie Constraints. Lastly, the gravity force had to be edited to include the weight of these new parts.

Starting with the T-beam, the largest profile for the available space was the T 35x35x5. Due to its non-symmetric bending resistance, this profile was attached to the robot plate surface in two different ways. It was connected by its flange - leaving the T upright - and by its web - inverting the T - leaving its flange suspended. This was done to test, if the fact of having more mass away from the plate, would bring more benefits against bending. For the model were introduced 7 beams with different lengths – 3 on the transverse direction between the robot feet, and other 4 parallel to the robot frontal plane - Figure 4.31.
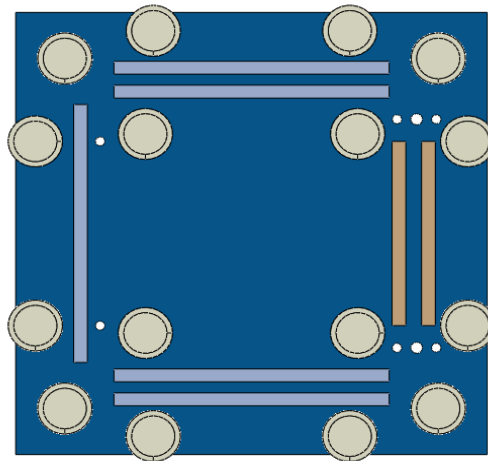
Figure 4.31 - Bottom view of the robot plate reinforced by 7 T-beams

The numerical results of these two models showed no practical variation on the maximum displacements at the robot plate. The best solution of the two had the T upright and its maximum displacement reduction was merely 0,41%. The other option had actually the same max displacement value as the model without reinforcements. This suggests that a model with a larger contact area between the two surfaces is a better option. However, this has to be better assessed because the Tie Constraint fuses completely the two surfaces – no matter their size. In practice, such an extensive surface connection is not so easily achieved. Regardless of those details, it seemed that adding T-beams would bring no structural advantages for the model, so there was no reason to explore them more.

The next experiment was the hollow square tube. Although there were also rectangular tubes, its smallest profile size would not fit the 39mm space without being attached by the largest dimension, occupying a larger area with smaller height than the square tube. The largest profile available was the 35x35 with 3mm thickness. The same number and length of tubes was utilized in this model as the previous case. It was not possible to approximate more the components, because it was always thought of having some space for a possible welding process. The simulation of this model revealed close results to the T-beams. The maximum displacement reduction at the robot plate was 0,37%, slightly less than the T-beam upright option. It was becoming evident that these slender reinforcements would cause no practical influence on the plate strains.

Indeed, the reinforcement with rectangular flat bars revealed closer results. The cross-section area selected was the 35x20mm², allowing the bar to be connected by the 20mm lateral surface and be left hanging with 35mm height. In order to occupy has much space as possible, the flat bars were approximated, leaving a small space for some welding process for example. A total number of 11 bars with different lengths were attached to the lower surface of the robot plate. The maximum displacement was slightly improved in this model with a reduction of 0,86%. However, this was not enough to make this a worth solution. The increased cost in buying and coupling these components to the robot plate would certainly be too high for the advantageous they provide.
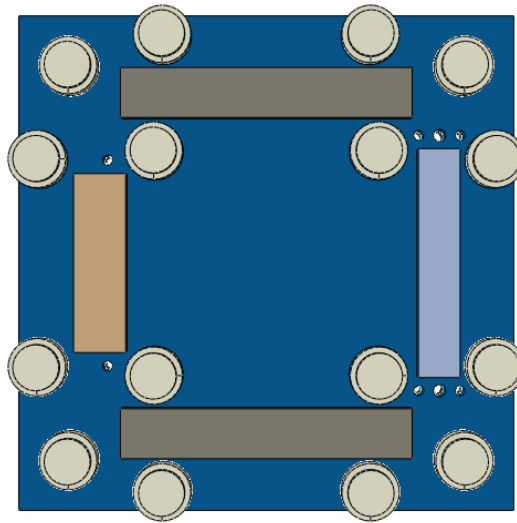
Figure 4.32 - Bottom view of the robot plate reinforced by 4 plates

As individual bars or beams were proving to be an inefficient option, it was thought of using additional metallic plates. This idea came up by coupling the flat bars all together, which would result in an equivalent new plate. Therefore, 4 new plates with 35mm height, different lengths and widths were modeled. These were attached to similar positions to the ones used in the other reinforcement models - Figure 4.32. However, the discretization element had to altered. In this case, the components were not slender anymore. Their overall shapes were like plate not beams or tubes. For this reason, the C3D8 element was also used for these parts. The results obtained from the simulation of this model revealed a decrease in maximum displacement of 2,76%.

Despite producing better structural results than the previous experiments, these plate reinforcements might not yet a be favorable option. Although the stress reduction is considerable, in respect to the displacement reduction its influence is tenuous. Additionally, the superficial connections used in Abaqus can hardly be achieved in a physical solution. Welding or bolt connections do not produce such a behavior between parts. This means, the usage of these plates should be better evaluated - with more appropriate connections to a real application – if its usage is intended. It might happen that using those proper connections in Abaqus will reduce even more the ability of the reinforcement plates to improve the structure bending resistance. In the end, this is another solution that might not be worth in comparison with the added costs it entails.

4.5.3   Plates Thicknesses

At last, the influence of the plate thicknesses on the structure response to the load was evaluated. It was already expected that thicker plates would develop less strains and internal stresses on the structure, thus the purpose of this study was to evaluate the tendency of the displacement reduction by increasing the plate thickness. To do so, the rate change of the maximum displacement value due to the plate's mass variation in respect to the model until now used was compared for different plate thicknesses. With this variation analysis it would be

possible to perceive how strongly the displacements changed throughout a short discrete interval of thicknesses.

This study evaluated the influence of each plate thickness separately. For the robot plate the values analyzed were 35mm, 50mm and 60mm. It was intended to experiment with 30mm, but that value did not fulfill the M16 screw minimum dimensions for the attachment of the clamping pin. Regarding the structure plate, model variations with 40mm, 60mm and 75mm were simulated. For these new models, the position of the reference point where the robot loads are applied had to be altered according to the structure dimensions. All other aspects of the numerical models were maintained. In Table 4.9 and Table 4.10 are shown the results obtained from the simulation of all systems only varying the thickness value of the studied plate.

Table 4.9 - Numerical results obtained for structural models with varying the robot plate thickness

NUMERICAL RESULTS	35	40	50	60
MAX DISPLACEMENT (µm)	209,8	186,7	155,8	135,9
DISPLACEMENT VARIATION (µm)	23,1	---	-30,9	-50,8
MASS VARIATION (kg)	-56,2	---	112,3	224,6
SENSITIVITY (µm/kg)	-0,412	---	-0,275	-0,226

Table 4.10 - Numerical results obtained for structural models with varying the structure plate thickness

NUMERICAL RESULTS	40	50	60	75
MAX DISPLACEMENT (µm)	230,0	186,7	159,8	150,0
DISPLACEMENT VARIATION (%)	23,2	---	-14,4	-19,6
MASS VARIATION (kg)	-702	---	702	1755
SENSITIVITY (µm/kg)	-0,062	---	-0,038	-0,021

From the table results it can be taken that the displacements vary less with the increase in the plates' thicknesses. In addition, it can be seen that the robot plate has a much stronger influence on the strains occurring in this component. At the same time, although not exposed in the tables, the stresses at the upper plate practically depended only on that plate thickness. This proves that an improved structure behavior concerns more the robot plate than the other structure components. For this reason, it is not worth to increase the size of the structure plate, when the other smaller plate has much more influence on the response to the robot load. The large structure plate will play a more fundamental role on assuring the construction integrity when other loads – besides the robot – are applied at the structure.

Although there is no defined value for the maximum allowable internal stresses or displacements occurring in the structure components, it was decided that a robot plate with 50mm thickness was a reasonable option for this construction. Being the most relevant component for the robot load response, it might be a good option to take a conservative decision and increase its thickness. With those dimensions, the robot plate would weigh around 560kg, which represents 20.7% of the industrial machine plus robot plate assembly.

At last, it was decided to reduce the size of the discretization elements on all parts of the selected model to make sure the results obtained were close to converging – under 2% variation. However, when simulating this virtual construction with a finer mesh the displacement values varied substantially. After further simulations with consecutive denser mesh, the maximum displacement results on the robot plate converged to a 170,8ym – an increase of 9,6% from the value presented in Table 4.9. However, the strains on the structure plate changed more considerably. This variation was mainly due to the previously coarse discretization of the structure plate. Since it was a large volume body and the focus was on the robot plate displacements, the elements' size was kept high for this component. Otherwise, a small increase in the mesh density would raise the computational costs drastically. Therefore, it is safe to assume that the variation on the maximum displacements results with a finer mesh, were mainly caused by a better discretized of the structure plate.

Regardless of that cause for the displacement values variation, this mesh refinement showed that the results in Table 4.9 were not inside the convergence interval. However, the purpose of that table was to compare the structural results between models with different plate thickness. The discretization parameters used were the same for all models – specially the number of elements along the thickness. In addition, the trend of displacement reduction with increased thickness is plausible. Considering that the variation on the displacements' results came from a denser mesh on the structure plate and not from the robot plate, then the comparisons between models with different robot plate thicknesses can be maintained even if the results were not converged.

4.6   Proposed Solution

Having chosen the robot plate thickness, this dimensioning work was concluded. All components connecting the robotic system to the base structure had been defined. The installation type of the clamping modules was selected based on the possibility to explore the space between the two plates. The size, number and position of these clamping components was chosen after a thorough comparison of different possibilities. The screws used to attach the clamping pins to the robot plate have also been selected, after evaluating the axial internal forces on this aggregated assembly. Finally, the dimensions of the robot plate were defined after having studied the influence of its area and thickness on the structural results. These components ensure the transmission of the robot load to the base structure without the risk of deforming plastically or failure of any bolted connection.

The von Mises equivalent stresses outside the singularity points are not high enough to reach yield stress values of a typical low carbon steel – even accounting for a safety factor of 1,7. Therefore, it can be assured that the deformable bodies in the model will not fail under the robot load. The axial forces measured on the pin-screw assemblies were much lower than the values developing at the examples given by SCHUNK, thus ensuring the proper attachment of

these two elements. The results of the moments equations for the clamping position chosen were higher than the maximum load values – even considering the safety factors applied. This suggests that the clamping modules utilized can sustain the forces transmitted.

However, it is important to refer that the torsion moments equation results for the different clamping configurations were the closest to the maximum load values. In addition, the maximum torsion torque during the robot model critical motion was in fact lower than the physical value provided by COMAU, contrary to the numerical tilt torques which were multiple times higher. This suggests that the structure might be over-dimensioned for the real critical tilt moment, but not far from failing at the physical, critical torsion moment. At the same time, adding more clamping points only slightly increases the torsion resistance in comparison with the tilt. This load component is the actual critical aspect of the structure integrity. It is here suggested to search for the maximum torsion value on a new motion analyses approach and better evaluate the torsion equation elaborated for the clamping configurations. Asking SCHUNK Services for clamping systems that sustain larger torsion torques is also recommended.

The clamping modules will certainly occupy a large portion of the costs associated with the modular structure, and thus the number of these components should be the smallest possible. Although the maximum value considered for the torsion torque was smaller than the load provided by the robot manufacturer and the equations utilized were not completely reliable, the clamping configuration proposed had a slightly higher value for the allowable torsion torques. Even accounting with a safety factor of 1,2 on top of the equations results. Therefore, it is at least safe to say that the here proposed solution will not fail under regular operations. The robot can be safely connected by the robot plate to the clamping modules and perform its motion without approximating failure on the components underneath. Nevertheless, further and more reliable evaluations of this aspect should be in the future performed.
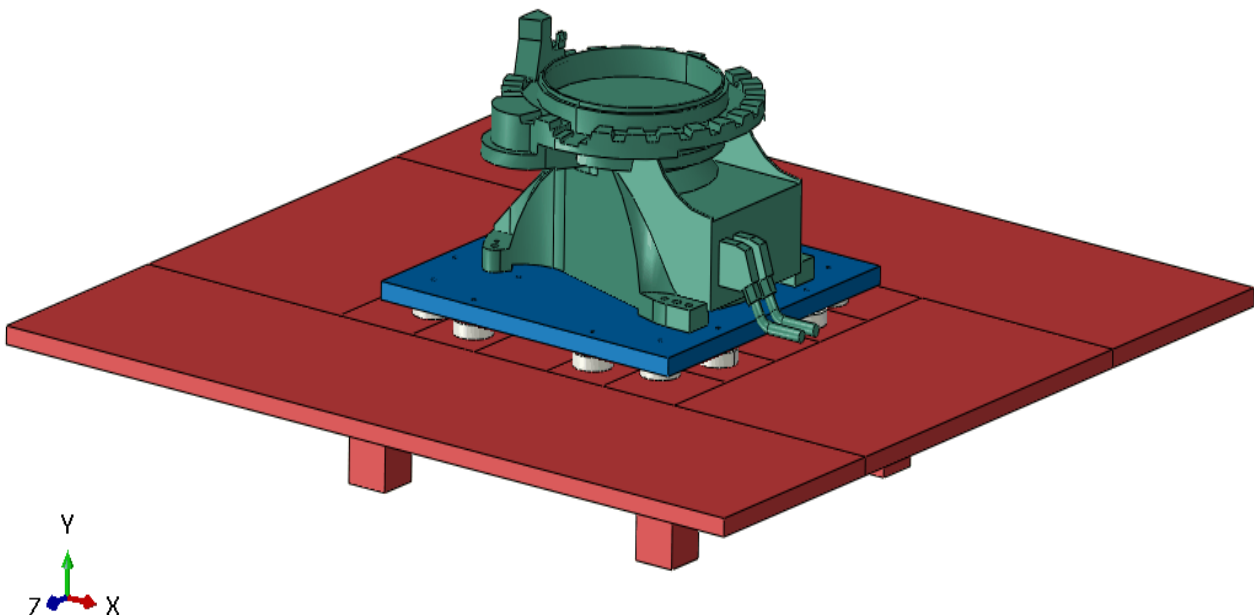
Figure 4.33 - Final structure model with the robot Base part

In respect to the displacements, it would be interesting to understand how much these values influence the positioning of the robot end-effector. This could be achieved by analyzing the deviation of the first rotation axis of the robot due to the strains occurring on the structure. Nevertheless, a maximum value around 170μm for the critical – extremely impractical – movement suggests that under regular operating loads the structure influence on the robot TCP positioning is very reduced.

The last part of the modular structure that needs to be defined is the structure horizontal plate, the supporting frame with the legs and feet, and all these elements' connections. This assembly of components will be responsible for many other functions besides withstanding the production system operation. Thus, those additional functionalities and loads will have to be accounted in order to properly develop this construction. In addition, as the last step demonstrated, the geometry and dimensions of the base structure do not heavily influence the structural response of the remaining components. This means, there is room to explore different solutions to answer the other structure functionalities, without risking the robot load supporting characteristics.

5   Summary

5.1   Summary

The objective of this work was to dimension a structure capable of handling the robot operation and at the same time of respecting the design criteria from the WSK project. To achieve this, was first necessary to identify the load that such a robot would exert on a construction supporting it. It was decided to search for the critical load, taking the worst-case scenario as the reference load applied. A methodic approach was designed and employed to obtain the critical movement of a kinematic model representing an industrial robot. This model was constructed based on multiple assumptions to try approximating its characteristics to the real machine. A multibody simulation program was utilized to experiment different movements, successively changing the axes rotations in order to obtain the critical motion for the entire robotic system.

With the critical motion from the kinematic model obtained, the associated load was introduced in a finite element analysis program to simulate the structural response of a construction model. An initial model with simple geometry was conceived based upon work previously done at the WBK research institute. This model resembled the overall dimensions of a possible final structure. During the dimensioning process, the virtual structure was successively updated to better portray the physical problem by adding new elements. The added elements were introduced to represent the load transmission through the components that achieve the "Plug and Produce" design concept. In the end, different dimensions for the construction components and other options were explored aiming to improve the structural results of the model. In the end, a final solution capable of fulfilling the design requirements and sustaining the robot load was proposed.

5.2   Outlook

This work was divided in two main phases: motion analyses of a robotic model and structural analyses of a corresponding modular support. The objective of each of these phases was achieved – obtain the robot model critical motion and dimension the structure to withstand the associated load -, but there are still aspects that remain to be answered.

The first big concern is the allowable torsion by the clamping systems. Although the approach taken in this work – to search the movement that promotes the highest magnitude torque - was a good initial assumption, it was later observed that it should have also considered other scenarios. The closest region of the structure model to reach failure is the clamping system due to the torsion moments. Its maximum allowable loads are the closest to the physical values presented by the robot manufacturer. As was previously suggested, this aspect of the structure model should be further evaluated, maybe consider utilizing more clamping modules even if it increases the construction costs.

Besides that, there are still other structural questions which were not evaluated, such as vibration dampening or loads from other components. The whole base structure – the supporting frame and the horizontal plate - also needs to be properly developed. And of course, the evaluation of cost/benefits needs to be performed in order to select preferable construction

options. Some examples are the plates' thicknesses, the different areas of the horizontal plate, and so on.

On the other phase of this work, the industrial robot model was evaluated with unreliable numerical model characteristics. Some of the load results obtained from the motion analyses revealed to be completely deviated from the physical values. If it is intended to use a multibody simulation program to aid future tasks of the WSK project, a better characterization of the robot characteristics needs to be made. A good option is to submit the physical machines to parameter identification procedures.

Nevertheless, the here proposed solution can be already tested as a prototype for the WSK project. Indeed, the final choice of all the parts and their dimensions will depend upon the prices of such components, but the dimensions proposed will safely handle the robot loads for a first experiment. There will always be a compromise between the allowable structure response characteristics and the price willing to pay. This decision will have to be later addressed by the institute researchers, and it might happen that it is necessary to change everything here proposed. The hope of this works author is that this report here exposed, and the conclusions taken from the multiple simulations performed can be helpful for those future decisions.

List of Figures

List of Tables

Publication bibliography

Alznauer, Sven (2021): Konzeptionierung und Entwicklung einer modular erweiterbaren Infrastruktur als Basis für roboterbasierte Produktionssysteme. Bachelor Thesis. Karlsruher Institut für Technologie (KIT), Karlsruhe. Institut für Produktionstechnik.

Bathe, Klaus-Jürgen (2006): Finite element procedures. Boston, Mass.: Bathe.

Blundell, Michael; Harty, Damian (2015): The multibody systems approach to vehicle dynamics. 2nd edition. Amsterdam: Butterworth-Heinemann.

Bundesministerium für Bildung und Forschung - BMBF (2021): Industrie 4.0. Available online at https://www.bmbf.de/bmbf/de/forschung/digitale-wirtschaft-und-gesellschaft/industrie-4-0/industrie-4-0.html, updated on 8/31/2021, checked on 8/31/2021.

Chang, Kuang-Hua (2015): e-design. Computer-aided engineering design / Kuang-Hua Chang. Amsterdam: Academic Press.

Comau (2021): NJ-290-3.0 - Comau. Available online at https://www.comau.com/en/competencies/robotics-automation/robot-team/nj-290-3-0/, updated on 7/13/2021, checked on 4/26/2021.

COMAU S.p.A. (2018): Technical Specifications NJ 290-3.0. Description, available versions and technical features of the Robot Robot workspaces and overall dimensions Features of the Robot wrist Robot integration principles and description of the available options.

Dassault Systèmes (2020): Abaqus/CAE User's Guide.

Deloitte Insights (2021): The smart factory. Available online at https://www2.deloitte.com/us/en/insights/focus/industry-4-0/smart-factory-connected-manufacturing.html, updated on 8/31/2021, checked on 8/31/2021.

Flores, Paulo (2015): Concepts and Formulations for Spatial Multibody Dynamics. Cham: Springer International Publishing.

Fu, Feng (2018): Design and Analysis of Complex Structures. In : Design and Analysis of Tall and Complex Structures: Elsevier, pp. 177–211.

González-Velázquez, Jorge Luis (2021): Chapter 1 - General concepts of mechanical behavior and fracture. In Jorge Luis González-Velázquez (Ed.): A Practical Approach to Fracture Mechanics: Elsevier, pp. 1–34. Available online at https://www.sciencedirect.com/science/article/pii/B9780128230206000013.

Haug, Edward J. (1984): Computer Aided Analysis and Optimization of Mechanical System Dynamics. Berlin, Heidelberg: Springer Berlin Heidelberg.

Jadav, Chetan; Gautam, Jignesh (2014): Multibody Dynamic Analysis of The Suspension System Using Adams 2 (03).

Jin, Jingfu; Gans, Nicholas (2015): Parameter identification for industrial robots with a fast and robust trajectory design approach. In *Robotics and Computer-Integrated Manufacturing* 31, pp. 21–29. DOI: 10.1016/j.rcim.2014.06.004.

Ling, Frederick F.; García de Jalón, Javier; Bayo, Eduardo (1994): Kinematic and Dynamic Simulation of Multibody Systems. New York, NY: Springer New York.

LookKIT 2020/1: Industrielle Transformation (2021): Wertstomkinematik. Variantenvielfalt durch flexibles Produktionssystem. KIT - Strategische Entwicklung und Kommunikation.

Lynch, Kevin M.; Park, Frank C. (2017): Modern robotics. Mechanics, planning, and control. Cambridge UK: Cambridge University Press.

MSC Software Corporation (2002): MSC ADAMS Product Catalog. Driving Innovation with Functional Virtual Prototyping.

MSC Software Corporation (2021): ADAMS Help 2021, checked on 4/25/2021.

Mühlbeier, E.; Gönnheimer, P.; Hausmann, L.; Fleischer, J. (2021): Value Stream Kinematics. In Bernd-Arno Behrens, Alexander Brosius, Wolfgang Hintze, Steffen Ihlenfeldt, Jens Peter Wulfsberg (Eds.): Production at the leading edge of technology. Berlin, Heidelberg, 2021. Berlin, Heidelberg: Springer Berlin Heidelberg, pp. 409–418.

Nikravesh, Parviz E. (1988): Computer-aided analysis of mechanical systems. Englewood Cliffs, NJ: Prentice-Hall.

Paul, Burton (1984): Computer Oriented Analytical Dynamics of Machinery. In Edward J. Haug (Ed.): Computer Aided Analysis and Optimization of Mechanical System Dynamics. Berlin, Heidelberg: Springer Berlin Heidelberg, pp. 41–87.

Pipinato, A. (2016): Bridge structural theory and modeling. In : Innovative Bridge Design Handbook: Elsevier, pp. 91–126.

Resman, Matevž; Turk, Maja; Herakovič, Niko (2021): Methodology for planning smart factory. In *Procedia CIRP* 97, pp. 401–406. DOI: 10.1016/j.procir.2020.05.258.

Rieg, Frank; Hackenschmidt, Reinhard; Alber-Laukant, Bettina (2019): Finite Elemente Analyse für Ingenieure. Grundlagen und praktische Anwendungen mit Z88Aurora. 6., vollständig überarbeitete Auflage. München: Hanser.

Schiehlen, Werner (2006): Computational dynamics: theory and applications of multibody systems. In *European Journal of Mechanics - A/Solids* 25 (4), pp. 566–594. DOI: 10.1016/j.euromechsol.2006.03.004.

SCHUNK GmbH & Co.: VERO-S NSE plus Brochure. Available online at https://schunk.com/us_en/homepage/vero-s-nse3/.

SCHUNK GmbH & Co. (2018): VERO-S quick-change pallet system: Assembly and Operating Manual. Available online at schunk.com.

SCHUNK GmbH & Co. (2021): Werkstückspannung – SCHUNK. Available online at https://schunk.com/shop/de/de/Spanntechnik/Bearbeitungszentrum/Nullpunktspannsysteme /Nullpunktspannsystem-fuer-allgemeine-Fraesanwendungen-und-Schwerzerspanung/, updated on 9/2/2021, checked on 9/2/2021.

Schwab, Klaus (2016): The fourth industrial revolution. Geneva, Switzerland: World Economic Forum.

Shabana, Ahmed A. (2013): Dynamics of multibody systems. 4th edition. Cambridge: Cambridge University Press.

Streamliner, F. DataE.M. (2021): What is shear locking | FEM Data Streamliner. Available online at https://femds.com/FEM_Guidelines/Prevent_Shear_Locking, updated on 9/7/2021, checked on 7/25/2021.

Szabo, B. A.; Babuška, Ivo (2011): Introduction to finite element analysis. Formulation, verification, and validation / Barna Szabo, Ivo Babuska. Oxford: Wiley-Blackwell.

The Efficient Engineer Channel (2021): Understanding the Finite Element Method. The finite element method is a powerful numerical technique that is used in all major engineering industries - in this video we'll explore how it works. youtube.com. Available online at https://www.youtube.com/watch?v=GHjopp47vvQ&t=369s, checked on 7/20/2021.

Udeyo, Felix (2021): Introduction to Structural Analysis, 9/1/2021.

wbk Institut (2021): wertstromkinematik.de. Available online at http://wertstromkinematik.de/, updated on 8/31/2021, checked on 3/5/2021.

Welch, Phoebe (2019): An Overview of How to Use ADAMS/Solver. Chapter 1 - ADAMS/Solver and MSS.

Werkle, Horst (2021): Finite Elements in Structural Analysis. Cham: Springer International Publishing.

Wojtyra, Marek (2009): Joint reactions in rigid body mechanisms with dependent constraints. In *Mechanism and Machine Theory* 44 (12), pp. 2265–2278. DOI: 10.1016/j.mechmachtheory.2009.07.008.

Wu, Wenxiang; Zhu, Shiqiang; Wang, Xuanyin; Liu, Huashan (2012): Closed-Loop Dynamic Parameter Identification of Robot Manipulators Using Modified Fourier Series. In *International Journal of Advanced Robotic Systems* 9 (1), p. 29. DOI: 10.5772/45818.